

Advanced Modelling Methodology for Bearing Chamber In Hot Environment

Deliverable: D3.1 Literature review on multiphase flow characteristics and heat transfer phenomena in the bearing chamber

Authors: Taras Mykhailenko, Oleksii Lysytsia, Andrej Brunak, Illia Petukhov (KhAI)

Contributors: Sergiy Yepifanov, Mykhaylo Ugryumov, Denys Nemchenko (KhAI)

Date of issue of this document: 14/07/2018

Start date of project: 01/05/2018

Duration: 36 Months



This project has received funding from the Clean Sky 2 Joint Undertaking under the European Union's Horizon 2020 research and innovation programme under grant agreement No 785493

Dissemination Level		
PU	Public	X
RE	Restricted to a group specified by the partners of the project	
CO	Confidential, only for partners	

Contents

Contents.....	2
Introduction	4
1. Experimental investigations on multiphase flow characteristics and heat transfer phenomena in the bearing chamber	8
1.1 Complex investigations of multiphase flow characteristics and heat transfer phenomena.....	8
1.2 Investigation of oil film behaviour.	14
1.3 Investigation of oil droplet flow behaviour.....	29
1.4 Investigation of air flow behaviour.	35
1.5 Investigation of heat transfer.	40
1.6 Experimental optimization of sump design.	51
1.7 Experimental investigation of leakages through the labyrinth seals.....	56
1.8. A review of wet gas flow rate measurements by means of singlephase meters	59
2. Mathematical models of the multiphase flow in the bearing chamber.....	62
2.1 A simplified models of the oil film on the housing of a bearing chamber.....	62
2.2 Mathematical model of thin film flow with droplet impingement	69
2.3 A coupled 1D film hydrodynamics and core gas flow model for air-oil flows in aero-engine bearing chambers	78
3. CFD modelling of multiphase flow in the bearing chamber.....	83
3.1 CFD modeling of Fluid and Gas Dynamics problems	84
3.2 CFD modelling of oil film behaviour.....	105
3.3 CFD modeling of Heat Transfer problems.....	126
Summary.....	132
References.....	134

Document History

Version and date	Changes
1.0 – 17/05/2018	Report structure: prepared by Taras Mykhailenko (KhAI)
1.1 – 13/06/2018	First draft: inputs provided by Oleksii Lysytsia, Andrej Brunak, Illia Petukhov, Sergiy Yepifanov, Mykhaylo Ugryumov, Denys Nemchenko (KhAI)
2.0 – 27/06/2018	Revised version: prepared by Taras Mykhailenko (KhAI)
2.1 – 05/07/2018	Revised version: reviewed by Mykola Lubiv (STCU)
3.0 – 14/07/2018	Final version: finalized by Taras Mykhailenko (KhAI)

Introduction

The lubrication system plays a key role in a reliable operation of gas turbine engines and their lifetime. The modern lubrication systems are in charge of lubrication and cooling of friction faces. They also prevent the faces from corrosion and peeling. The oil takes away the debris appeared due to the friction. The lubrication system reduces the noise in the friction zones and gearings as well. The oil from the lubrication system also keeps the pressure in the bearing cavities, drive cavities and gearbox cavity at the appropriate level. Providing all these essential things, the lubrication system shall be operationally efficient and accessible for maintenance.

The oil feed fault may damage the bearings and gearings and, as a result, initiate overheating of the engine or even bearing failure, which usually means engine destruction. The bearing chamber also belongs to the targets of the lubrication system.

The bearings transfer the forces from the rotating elements to the casing. Hence, they take considerable static and dynamic forces from the engine rotors. The bearings shall ensure the rigidity of the power frame and centring within the entire range of expected forces. The example of the bearing chamber locations in the gas turbine engine is shown in Figure 1 [1].

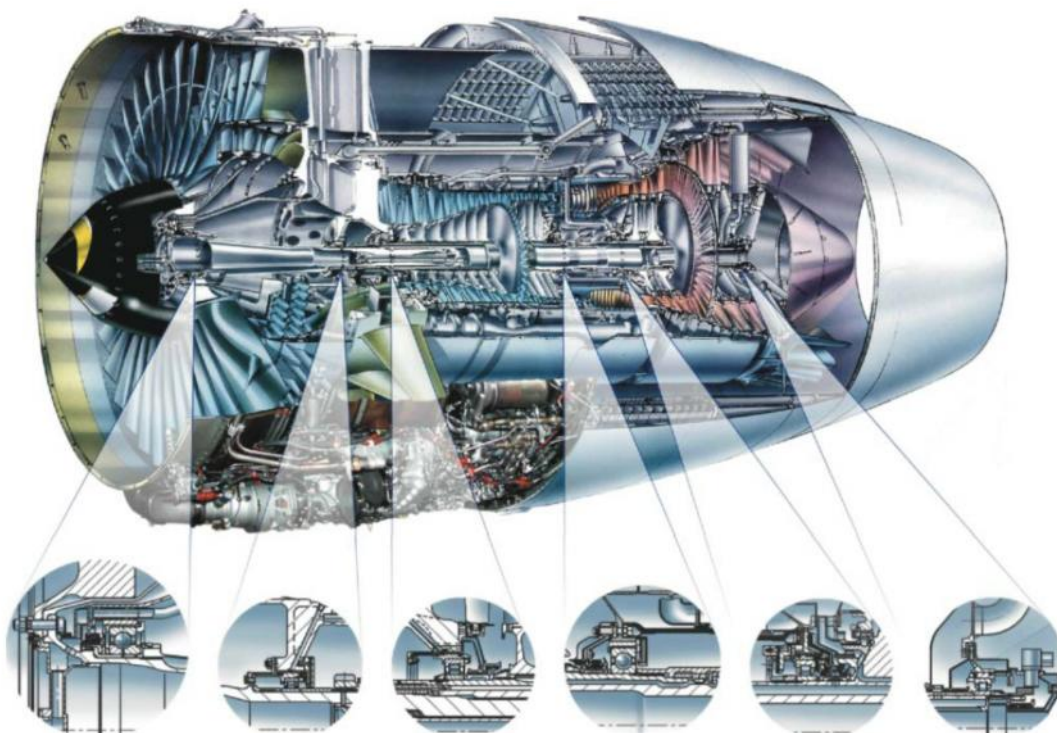


Figure 1. Bearing chamber locations

Regardless of the bearing chamber design, the pre-chamber is pressurized with air from the compressor. The pressure drop between the bearing chamber and pre-chamber prevents the oil leakage from the bearing chamber. Hence, the hot air enters the bearing cavity and blends with the oil forming the air/oil mixture. The air leakage over the labyrinth seal depends on their type, condition and pressure drop.

To determine the required oil flow to the bearing chamber, one must know the heat flux to the bearing cavity from the external environment. In general case, the heat flux consists of the components presented in Figure 2 [2].

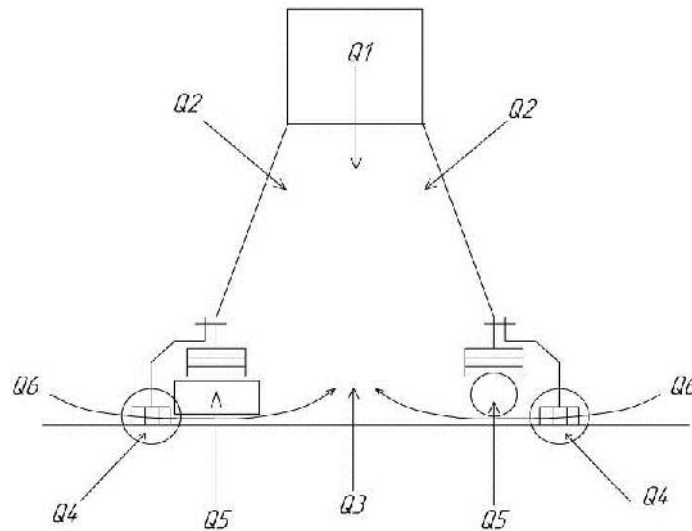


Figure 2. Components of the heat flux into the bearing chamber

The heat flux includes the heat load from the gas path (Q_1), through the bearing chamber wall (Q_2), from the shaft (Q_3), from the seals (Q_4), from the bearings, gears, spline joints, etc. (Q_5), from air enters over the labyrinth seal (Q_6).

The heat from the gas path to the bearing cavity transfers due to the thermal conductivity and convection. The components, which are in contact with the gas path, serve as transmitters. Similar process can be observed in the heat flux from the shaft.

The heat transfer is provided by the convection, heat conductivity and radiation. The convective heat exchange is dominant in case of heat transfer from flow to the bearing chamber wall and from the bearing chamber wall to the contacting flow. The impact of radiation is considerable for the turbine bearings.

Generally, heat flux through the bearing chamber wall is described by the heat transfer equation [3]:

$$Q_2 = U(t_{\text{air}} - t_{\text{mix}})A,$$

where U – overall heat transfer coefficient, $W/(m^2 \cdot K)$; A – heat transfer area, m^2 ; t_{air} – air temperature from external side of bearing chamber, K ; t_{mix} – temperature of air/oil mixture inside bearing chamber, K .

To calculate the heat transfer from the gas path to the bearing chamber, heat transfer through the chamber walls and heat transfer from the shaft, one must preliminary determine the temperature of support elements and heat transfer coefficients.

Hence, to get the heat transfer coefficients in the pre-chamber, one must know the temperatures and pressures at the points, where air is taken and where it is exhausted. Next, using the known geometrical parameters of the channels and the determined gas dynamic parameters, one can determine the flow parameters in the entire system. Besides, air heating because of non-uniform temperature state of the system shall be taken into account.

Heat transfer coefficients of the bearing chamber elements depend on many factors, like flow structure, rotational speed of the shaft, amount of injected oil and airflow rate over the labyrinth seal, geometrical parameters of the cavity, etc. One of possible flow structures in the bearing chamber is shown in Figure 3 [4].

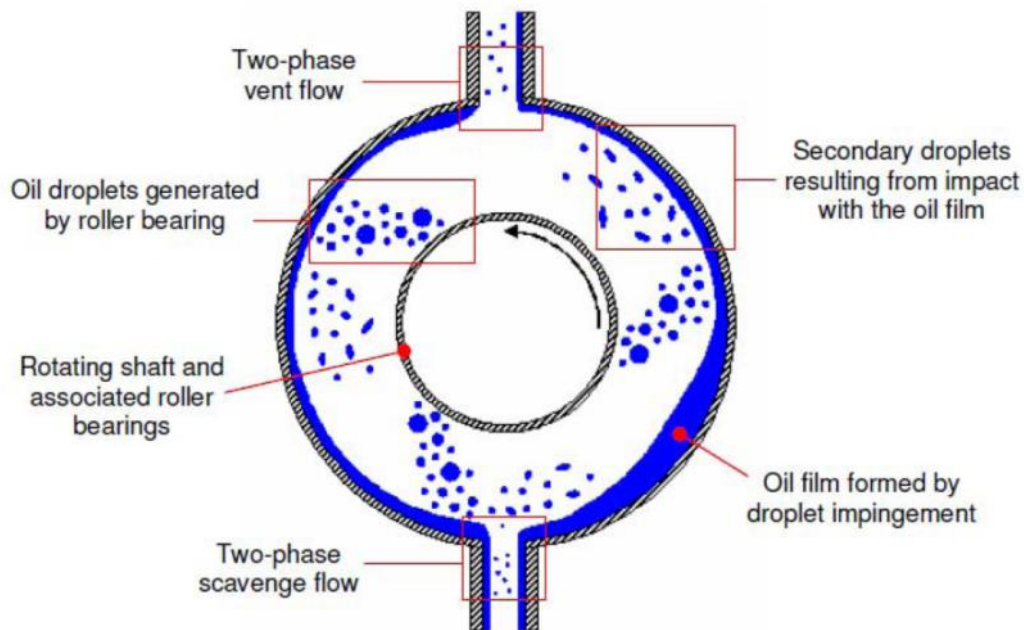


Figure 3. Multiphase flow structure in the bearing chamber

The problem of heat exchange simulation is caused by the multiphase fluid in the bearing chamber. The fluid is a mixture of the injected oil and air from the labyrinth seals. Getting through the nozzle on the surface of the bearing, oil spreads over it, forming the oil film. Some droplets of oil are separated from the oil film and carried to the inner surface of the chamber by the centrifugal forces and interaction with the airflow. During this process, the droplets interact with the airflow, exchanging momentum and energy with the latest. Getting to the wall of the bearing chamber, oil droplets form a moving film on the interphase surface. The film is moving because of aerodynamic forces, gravity and viscosity. The formed film is influenced by the droplets, which fall on it from the bearing, as well as by the air flow, which can generate and carry out the droplets from the surface of the film. Because of this complex interaction, the oil film has a variable thickness along the circumference of the bearing chamber. This fact affects the process of heat exchange between the chamber walls and the air / oil mixture.

It is very difficult to cover thermal and hydraulic processes in the bearing chamber in the mathematical models. The behaviour of the multiphase fluid (droplet-film-air) is influenced by oil and air flow rates, rotation speed and direction, bearing chamber design, pressure in the bearing chamber, changes in the thermodynamic properties of the phases due to heat transfer, roughness of the chamber walls and many other factors.

Investigations of multiphase flow characteristics and bearing chamber heat transfer phenomena are extremely important works for aviation industry because their results will ensure development of efficient engine components. This report presents a literature review on investigations of multiphase flow characteristics and heat transfer phenomena in the bearing chamber. For the purpose of this report preparation, the research articles published

in thematic journals and conference proceedings together with the publicly available results of research projects funded by the European Commission's Framework Programmes (ELUBSYS "Engine Lubrication System Technologies"; E-BREAK "Engine Breakthrough Components and Subsystems"; ATOS "Advanced Transmission and Oil System concepts", INNOVATE "The systematic Integration of Novel Aerospace Technologies"), UK Technology Strategy Board SILOET and SILOET 2 Programmes, UK Research and Innovation SAMULET Program, National cooperative research projects of the German Federal Ministry of Economics and Technology and Rolls-Royce Deutschland (LuFo-20T0605 Luftfahrtforschungsprogram 2007-2010), European Community's Industrial and Materials Technologies research programme "Brite-Euram" (project BRE2-CT94-0538), were reviewed and analysed.

1. Experimental investigations on multiphase flow characteristics and heat transfer phenomena in the bearing chamber

This part of literature review deals with experimental research of multiphase flow characteristics and heat transfer phenomena in the bearing chamber. This review gives the design and operability of test rigs of different experimental groups. On the basis of different author's articles analyses conclusions about observed test rigs possibilities, differences, advantages and disadvantages were made.

1.1 Complex investigations of multiphase flow characteristics and heat transfer phenomena

This section presents the researches dealt with the complex investigations of multiphase flow characteristics and heat transfer phenomena in the bearing chamber.

The article [5] deals with the research of processes occurred in the aircraft engine bearing chambers: heat transfer and thickness of oil in the chamber. The test rig of [5] is presented in Fig 1.1.

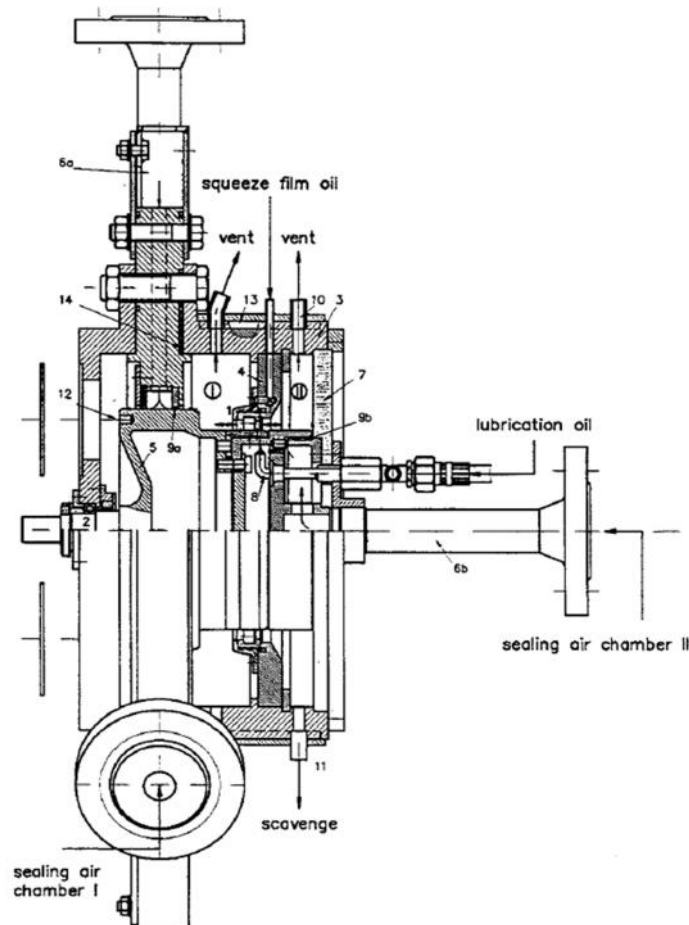


Figure 1.1. Test rig:

1 – roller bearing; 2 – axial fixed ball bearing; 3 – housing; 4 – roller bearing support unit (flange); 5 – rotor; 6a – sealing air supply chamber I; 6b – sealing air supply chamber II; 7 – transparent cover; 8 – under race lubrication; 9 – labyrinth seal; 10 – vent; 11 – scavenge; 12 – balancing hole; 13 – cooling duct; 14 – insulation.

Features of test rig:

- 2 oil cavities (I and II) with aspect ratio $b/h = 1.0$ and 0.5 ;
- roller bearing chamber is researched;
- method of lubrication – under race;
- transparent disc covering chamber is used to provide the experiment of oil film thickness measuring. It is made from high temperature thermoplastic material;
- three fin labyrinth seals are used to prevent leakages;
- maximal rotation speed – 16000 rpm;
- cooling fluid – water;
- the housing is mounted with an insulation layer consisting of ceramic paper;
- sealing air is supplied by compressor with $\kappa=4$;
- 18 Ni-Cr-Ni thermocouples are used to measure the temperature inside the chambers.

The paper presented the heat transfer analyses in the bearing chamber. To obtain the heated state in the bearing chambers the finite element method is used (200 elements and 500 nodes for housing, 32 elements and 85 nodes for bearings).

The relative error of the local heat transfer coefficient $\frac{h_g}{h_c}$ is a function of the wall thickness l , the thermal conductivity λ , the heat transfer coefficients at both sides of the wall (h_g, h_c) and the temperature difference $\Delta T = T_g - T_c$ (where “g” – gas, “c” – coolant).

To realize a high temperature difference, cooling ducts are provided with water as a cooling fluid. Wall thickness l and thermal conductivity λ can be adjusted in order to minimize the relative error by use of next equation:

$$\left(\frac{\lambda}{l}\right)_{opt} = \frac{r_g}{\sqrt{1 + \frac{r_g}{r_c}}}$$

At a rough guess of heat transfer coefficients, the appropriate wall thickness is fixed by the thermal conductivity of used material.

Local heat transfer is derived from the heat flux Q :

$$d\dot{Q} = -\lambda \cdot dA \cdot \nabla T_{(wall)}$$

where A – surface area.

The local heat flux $d\dot{Q}$ is determined from an assumed two-dimensional temperature distribution in the housing. Temperature distributions are calculated from the wall temperatures using a finite element code. Wall temperatures T_w at each boundary node of the finite element mesh have to be interpolated from the measured values by spline functions. For a high temperature utilization the dependence of the thermal conductivity from the temperature has to be taken into account. Iterative correction method, considering a linear relation:

$$\lambda(T) = \lambda_{0^{\circ}C} + s\Delta T$$

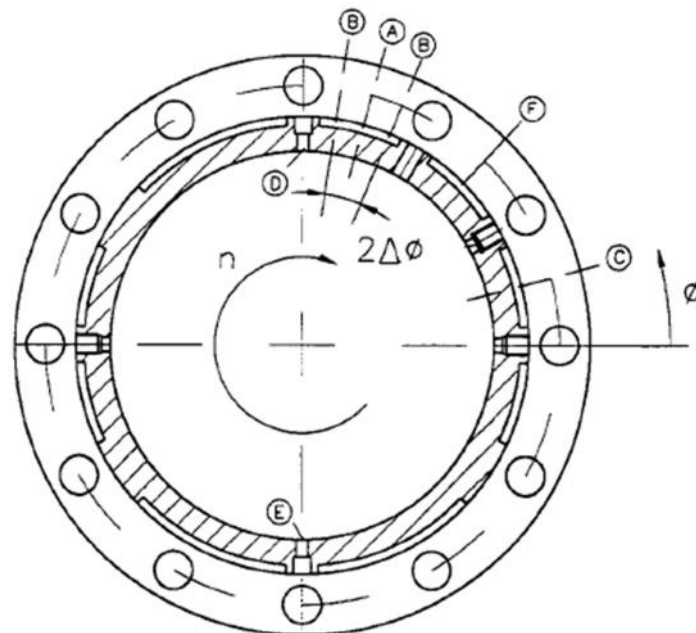
where $\lambda_{0^{\circ}C}$ and s (gradient of temperature dependent thermal conductivity) are given by the material.

Heat transfer coefficients were calculated using the next equation:

$$r = \frac{d\dot{Q}}{dA(T_g - T_w)}$$

where gas temperatures T_g are determined from local measurements and interpolated analogous to the wall temperatures as described above. In addition, the code has been adapted to applications in cylindrical coordinates.

Besides the main plane (A) additional instrumentation is provided as shown in Fig. 1.2.



A) main instrumentation plane B) 2-d reference instrumentation C) circumferential reference instrumentation D) vent port E) scavenge port F) cooling duct

Figure 1.2. Measuring planes

For a lubrication oil flow of $\dot{m}_{oil,T} = 50 \cdot 10^{-3} \text{ kg/s}$ and a sealing air flow of $\dot{m}_{air, ch} = 12 \cdot 10^{-3} \text{ kg/s}$ the strong effect of rotational speed on the heat transfer characteristic is shown in Fig. 1.3.

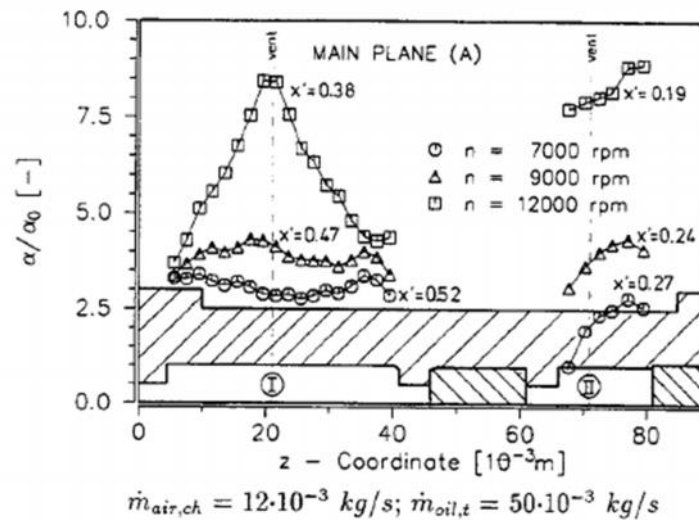


Figure 1.3. Variation of rotational speed

To measure the oil film thickness, the ultrasonic method is used, especially – the reflection of ultrasonic waves transmitting the contact surface of materials with different acoustic resistances (pulse echo principle). It notes that choosing the right sensors is very important. The thermoplastic cylinder with an acoustic density fitted to the oil through the steel housing to increase the efficiency of method. Measuring scheme is presented in Fig. 1.4.

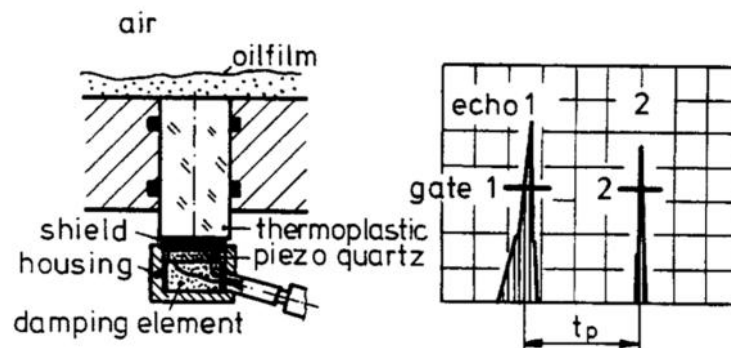


Figure 1.4. Measuring of oil film using the ultrasonic method

Oil film thickness is calculated by the next formula:

$$2h_f = a_{oil} \cdot t_p$$

where h_f – average oil film thickness; a_{oil} – velocity of sound for the turbine oil; t_p – measured time between peaks.

Features of ultrasonic method:

- nonreactive with the oil film;
- insensitive to vibrations,
- small lower limit of the measuring range of $hf = 100 \mu\text{m}$.

Results of film measuring are presented in Fig. 1.5.

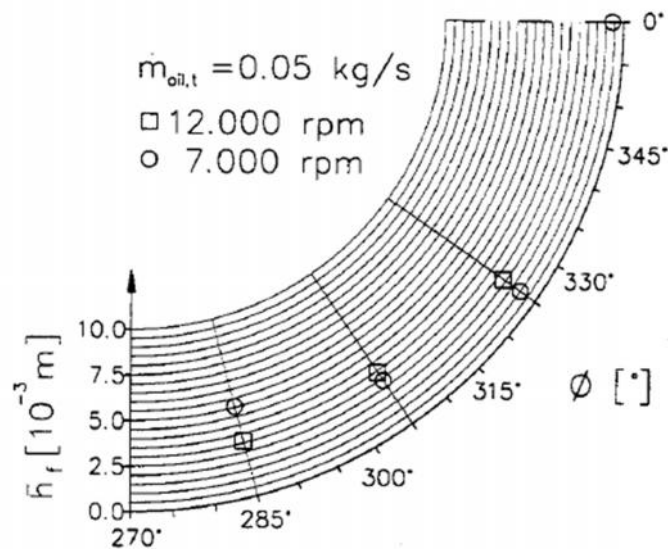


Figure 1.5. Results of oil film measurements

Article [5] present the complex investigation of processes occurred in bearing chamber and measuring the heat state in the chamber and oil film thickness. According to the test rig design it can be noted that lubrication supply method is represented only by under race lubrication; method of direct oil supply to the bearing cage was not observed. Additionally several parameters of described test rig are not enough high comparing with the typical parameters of modern aircraft engines, for instance, rotor rotational speed and oil flow. The experiment would be more complete if heat transfer will be researched not only for the several parts of cavities (outer housing, wall between cavities) but for the shaft and bearing. Additionally the paper presents the single measurements whereas it is interesting to measure the changing of oil film thickness in time. It should be noted that the influence of oil drops was did not taken into account. And it is no data about verification of measure method with some known information and dependences.

Test rig represented in paper [6] present the modification of test rig showed in Fig 1.1: bearing chambers I and II are of another dimension (both smaller in radial direction). Paper [6] deals with the oil film flow characteristics in the bottom region of chamber II at a location 30° upstream of the scavenge port, where the film velocity measurements by Laser Doppler Velocimetry (LDA) have been performed. In addition, heat transfer instrumentation is provided to this location and oil film temperatures necessary for the nondimensional treatment of oil film velocity and height have been measured next to it. For the nonreactive determination of film heights a capacitive gauge has been mounted flush with the internal bearing chamber housing wall at a position $=15^\circ$ upstream of the heat transfer measuring plane.

Exemplarily results for film heights \bar{h}_F and film velocities \bar{u}_F measured for typical aero-engine conditions are shown in Fig. 1.6.

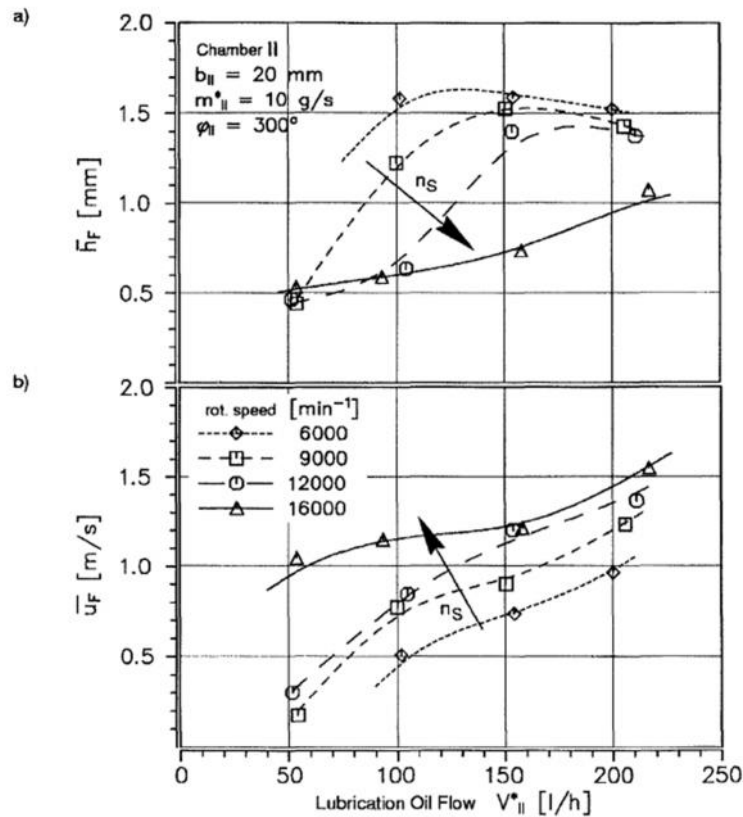


Figure 1.6. Oil film flow analysis inside chamber II:

(a) film thickness, (b) film velocity

An increase of rotational speeds causes an oil flow pattern distributed more homogeneously inside the chamber, i.e. for a given lubrication oil flow to the chamber the local oil film mass flow at a location in the bottom region decreases and the film height decreases as well. So higher lubrication oil flows give larger film heights.

As it was shown in paper [6], characterization of the momentum and heat transfer in bearing chamber oil film flows requires a proper matching of the eddy viscosity ϵ_t / ϵ_F and, in addition, an expression for the turbulent Prandtl number Pr_t . So the next expression was used for the calculation of eddy viscosity:

$$\epsilon_t / \epsilon_F = n^2 u_F^+ y_F^+ \{ 1 - \exp(-n^2 u_F^+ y_F^+) \}$$

where ϵ_t – eddy viscosity; ϵ_F – film kinematic viscosity; n – constant; u_F^+ – nondimensional film velocity; y_F^+ – nondimensional distance from the wall.

Additionally using the turbulent Prandtl number was assumed to be equal 1. The theory leads to lower predictions of the heat transfer coefficients taken from measurements but the qualitative estimate of the heat transfer characteristic is quite well. The theory approach will be considered in section 2. Considering the simplifications which have been made, the agreement between theory and experiment ($\epsilon_t / \epsilon_M \approx 34\%$) is remarkable and could be further improved by correlations which give lower values for Pr_t .

1.2 Investigation of oil film behaviour.

Researches of article [7] used the modified test rig (based on test rig showed in Fig. 1.1 with bearing chambers of another sizes) to measure the oil film shear velocity by using of fibre-optic LDV-setup (Laser Doppler Velocimetry), showed in Fig. 1.7.

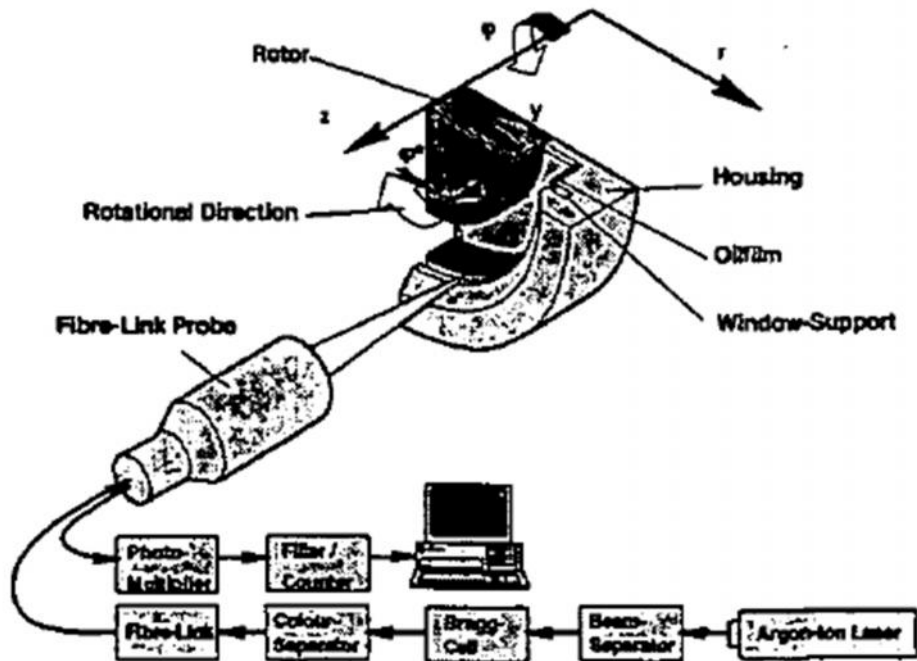


Figure 1.7. Fibre-optic LDV-setup

This investigation has been focused on the question of whether the oil film flow in bearing chambers can be characterized by a theoretical approach of the velocity profile, which is the main presupposition for any further modeling of bearing chamber flow conditions.

The system presented in Fig. 1.7 has been used for the determination of oil film velocities parallel to the housing wall. It comprises a 4 W Argon-Jon laser, a standard optic with 40 MHz Bragg-cell, color and beam separators, and a 2D fibre probe. The signals are detected in a backscatter mode by a fibre link and photomultiplier setup in combination with filters and the counter processors. Operating as a data link between the counter processors and the micro computer (PC 80386), the interface card writes all data information into the computer memory.

Due to the thin oil films in the range of $1\text{mm} < h_f < 2\text{mm}$ measurements have to be performed close to the wall and, therefore, only one component of the LDV could be used. All velocity profiles and measurements have been determined at an axial distance of 2 mm from the transparent cover large enough to avoid any effects of wall friction.

The paper uses models described by the next equations:

$$u_F^+ = y_F^+ - \frac{1}{2} \dagger (y_F^+)^2$$

$$\frac{du_F^+}{dy_F^+} = \frac{1 - \dagger y_F^+}{1 + n^2 u_F^+ y_F^+ \{1 - \exp(-n^2 u_F^+ y_F^+)\}}$$

where u_F^+ – nondimensional shear velocity; y_F^+ – nondimensional distance from the wall; \dagger – nondimensional parameter for the film velocity profile; n – constant.

The operating conditions are given by a lubrication oil flow of $V_{II} = 150$ l/h and a sealing air flow of $\dot{m}_{II} = 10$ g/s to chamber II, and by rotational speeds of $n_w = 3000$ rpm to 16000 rpm. As expected, an increase of the rotational speed results in an increase of the gas/liquid interface shear force and, as a consequence, in enhanced film velocities and decreasing film thickness.

A comparison between measurement and theory for each of the models given by mentioned above equations is presented in Fig. 1.8. Each single frame shows one operating condition characterized by air and oil flows and rotational speed.

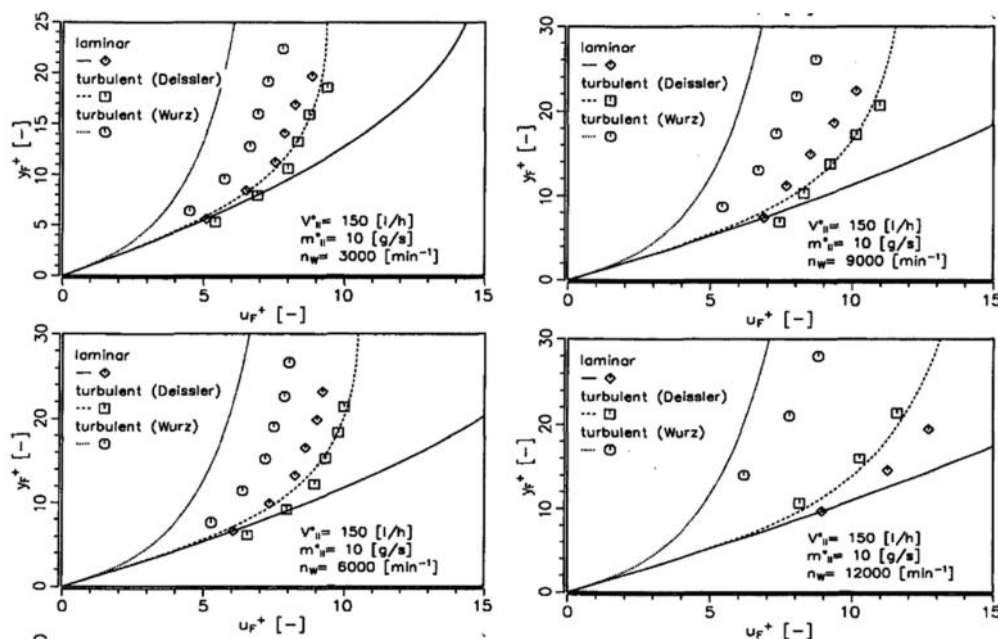


Figure 1.8 Nondimensional film velocity profiles: comparison with theory

Based on LDV-measurements of oil film velocity profiles, an assessment of three different approaches for the characterization of oil film velocities in bearing chambers has been performed. Turbulent flow conditions have been found for all operating conditions. An analytical approach considering temperature dependent liquid properties, geometrical conditions, and a correlation for the eddy viscosity has been found to reflect the measured data excellently. This leads to several benefits with respect to an analysis of bearing chamber oil film flows. Due to the knowledge of the velocity profile a further modeling of the oil film behavior is possible by reducing dimensional values for film height and velocity to non-dimensional flow parameters as represented by the Reynolds number. It should be noted that measurements were provided only on the one side of one chamber which is not

enough for full observing the processes occurred in both chambers. And the measure error of method was not observed.

Measuring of oil film thickness using capacity sensors and measuring of oil film velocity using LDV-technic is presented in [8]. Test rig used in [8] presents the equipment shown in Fig. 1.1 modified to research the bearing chambers of various sizes. In the present study the film thickness was determined as a function of the circumferential position for three different geometries by using capacitive sensors. At one angular position film velocity profiles were measured with the LDV-method. The geometries and the instrumentation are shown in Fig. 1.9.

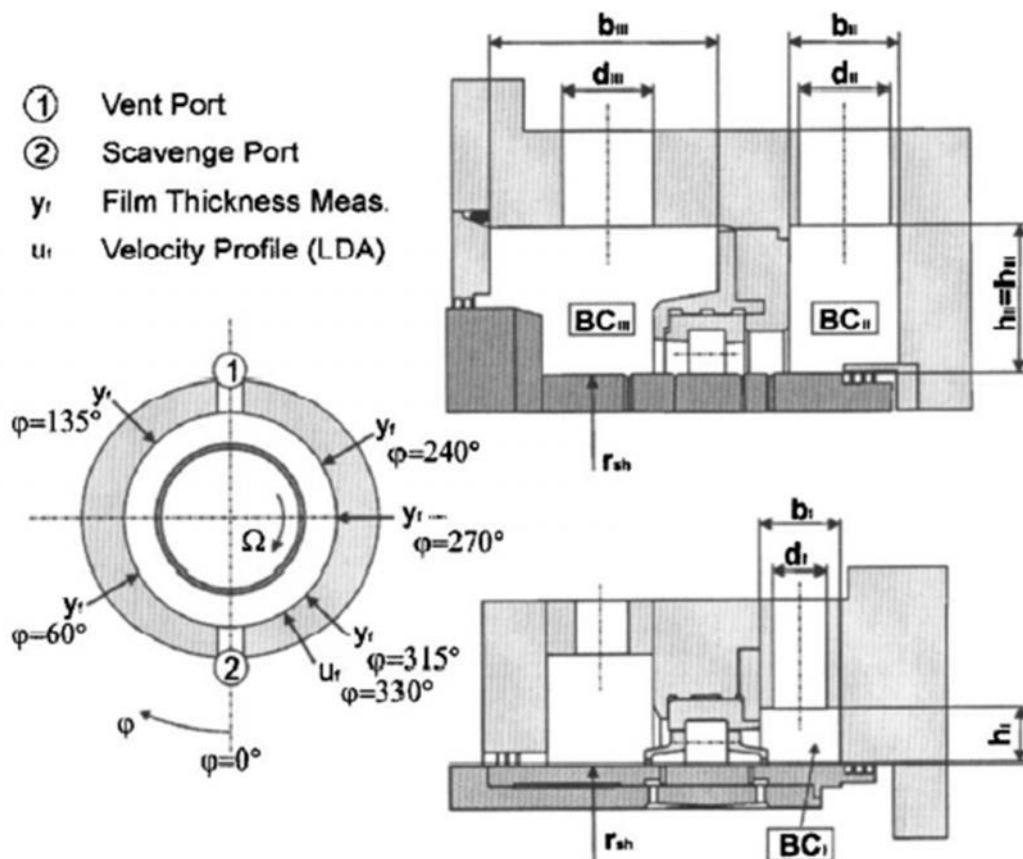


Figure 1.9. Different configurations of bearing chambers and angular positions of film thickness and velocity measurements

The experiments were focused on the characterization of the liquid wall film along the radial housing of the bearing chamber. Therefore, velocity profiles and the film thickness were determined using the LDV technique and capacitive sensors, respectively.

Capacitive film thickness sensors were used to measure the local film thickness at five angular positions in each chamber BC_I – BC_{III} (Fig. 1.9).

A capacitive determination of a liquid film thickness is based on the dependence of the capacity on the specific dielectric coefficient. In general, the dielectric coefficient depends on material properties. Therefore, the measuring device is influenced by the volume fraction of the liquid located inside the probe volume. It should be note that capacitive gauge is

insensitive to vibrations, easy to handle and adaptable to the geometry. In addition, this technique is characterized by a high resolution especially in the short range of the sensor and can easily be linked to the data acquisition system of the test facility.

An application inside the bearing chamber implies a sensor that can be adapted to the geometry without lapping into the chamber. This demand is fulfilled by the sensor shown in Fig. 1.10. Ground and shield electrode are located as concentric rings around the measuring electrode. Measuring and shield electrode are on the same electric potential, thus the homogeneity of the electric field in the short range of the sensor is given. Increasing the distance of the film surface from the sensor, the electric field becomes more and more inhomogeneous, so that the capacity C and in consequence the film thickness is determined by use of calibration functions. Therefore, the sensors were calibrated at static conditions down to a minimum film thickness of 0.2 mm.

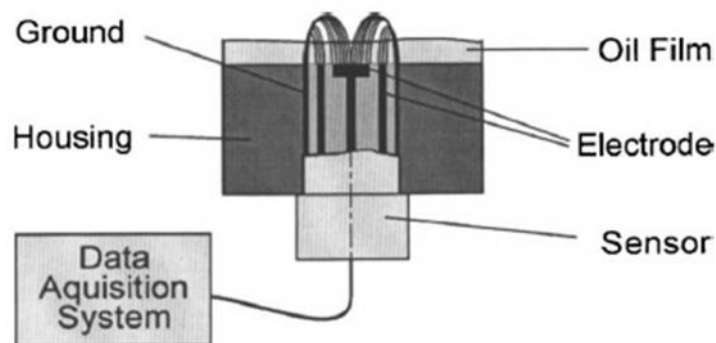


Figure 1.10. Determination of film thickness using capacitive sensors

To permit a comparison of the different configurations and to predict the film flow as a function of the circumferential location, two analytical models were introduced (see section 2). The first model estimated the tangential velocity the pure air flow in the chamber using an angular momentum balance. This velocity was used to estimate the impact of the air flow on the film for the different geometries. A comparison with experimental data revealed that this approach predicts the pure air flow with a very good accuracy. The second model was used to characterize the shear and gravity driven wall film. As it is mentioned in the paper, the suggested model uses the oil velocity and oil film thickness that were obtained by the experiment.

Papers [9, 11] present results of experimental investigation from oil film behavior in a bearing chamber test rig shown in Fig 1.11. Some modifications were made to the initial test rig (see Fig. 1.1) to understand the influence of offtakes to the observed processes:

- the vent offtake can be mounded not only in the upper part of test ring but on the various angles (Fig. 1.12). As the thread of the film thickness sensor mounts is the same as of the vent offtake mount, it can be placed at any position of a film thickness sensor and vice versa;
- design of scavenge offtake can be changed (Fig. 1.13).

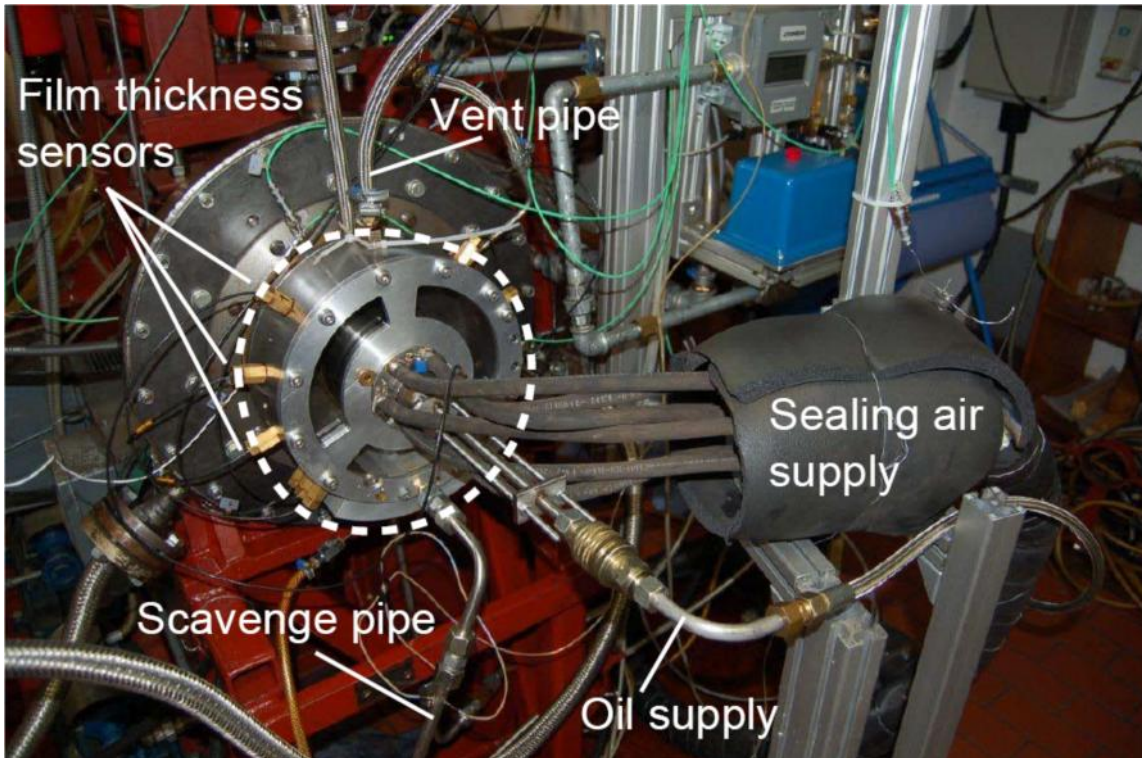


Figure 1.11. The bearing chamber test rig

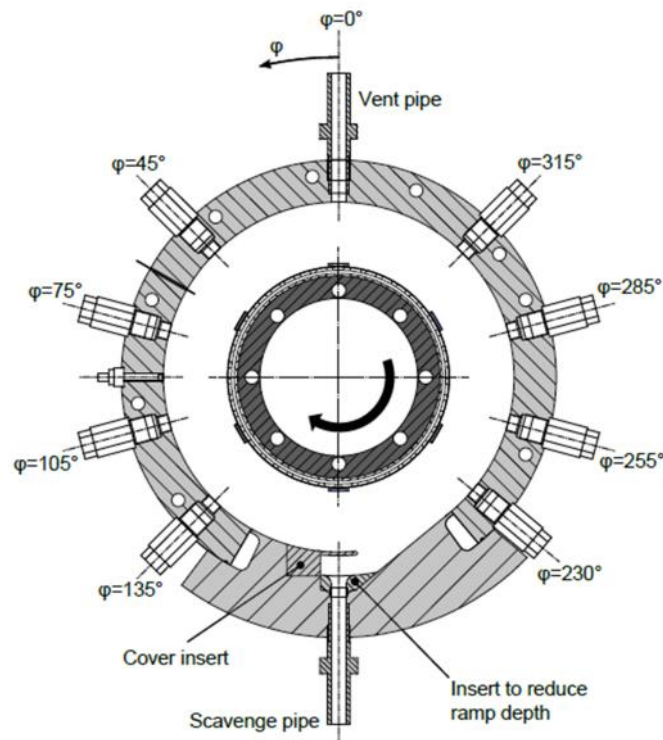


Figure 1.12. Positions of film thickness sensors; configuration with a covered shallow ramp and a flush mounted vent offtake

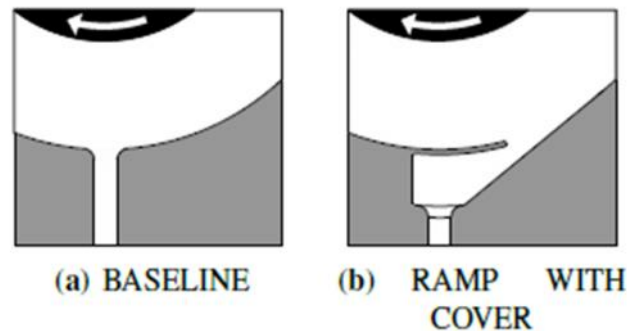


Figure 1.13. Schematics of the scavenge oftakes

Measuring of film thickness represents the modified method of [8]. To use capacitive distance sensors for the measurement of oil film thicknesses in the bearing chamber test rig, they have to be modified. First, a small polycarbonate platelet is glued onto the sensing surface, which primarily is needed to compensate a certain offset thickness of the sensor signal. After mounting the sensor-platelet assembly into the housing of the bearing chamber, the surface can be adapted to the housing curvature by polishing the polycarbonate platelet. Fig. 1.14 shows a schematic of the sensor setup in a curved surface. As a consequence, each sensor has a distinct offset voltage and a distinct correlation between film thickness and output voltage.

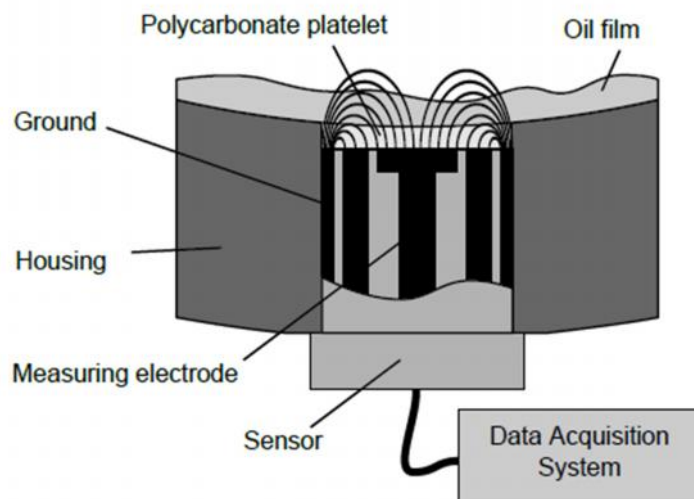


Figure 1.14. Schematic of the sensor-platelet assembly in a curved surface

For the first time ever, film thickness measurements were carried out at different pressures in the same bearing chamber configuration. The applied capacitive sensors were adapted to the surface of the chamber wall and in-situ calibrated by means of stacked adhesive tape strips. This approach yielded results with an acceptable accuracy and repeatability.

The results of [9, 10] confirm some of the findings from other experimental studies: at low shaft speeds, the oil film is mainly gravity-driven, and in the co-current half of the chamber, there is almost no interaction between the air and oil flows. The oil flow and the scavenge ratio have a minor influence. In [10], two important parameters were determined: the

pressure in the bearing chamber and the offtake design. Previous studies already indicated an influence of the chamber dimensions and of the offtake designs. A comparison of the film thicknesses in a vented versus a ventless configuration showed that the results are not transferable at high shaft speeds due to the missing outlet in the ventless configuration.

A direct comparison of film thickness at different pressure levels showed a strong increase with higher pressures in the left half of the chamber, where gravity and shear forces point into opposite directions. An analysis of the momentum flux of the air flow for each test case revealed that this parameter correlates strongly with the film thickness. The initiation of the rotation of the whole oil film could also be related to a certain momentum flux threshold.

Papers [9, 10] represent important research that shows influence of various operation factors and elements of design to the oil film thickness. But paper does not include the modeling or theoretical approach that can help to use the obtained results on the other constructions.

The investigation of flow regime in aero engine bearing chambers of various sizes is presented in [11]. In general, one of two distinct flow regimes can occur in a bearing chamber. At lower shaft speeds, the oil flow is only partially affected by the air flow, which is driven by the rotating shaft. At higher shaft speeds, however, the rotating air flow forces the oil film at the chamber walls to rotate, too. Thus, the two flow regimes correspond to two very different oil film distributions inside a bearing chamber presumably with significant consequences for the internal wall heat transfer. In order to determine the driving parameters for the flow regimes and the change between them, experiments were carried out with a bearing chamber test rig (Fig. 1.1) with some modification: the dimensions of the bearing chamber can be varied using special inserts (Fig. 1.15).

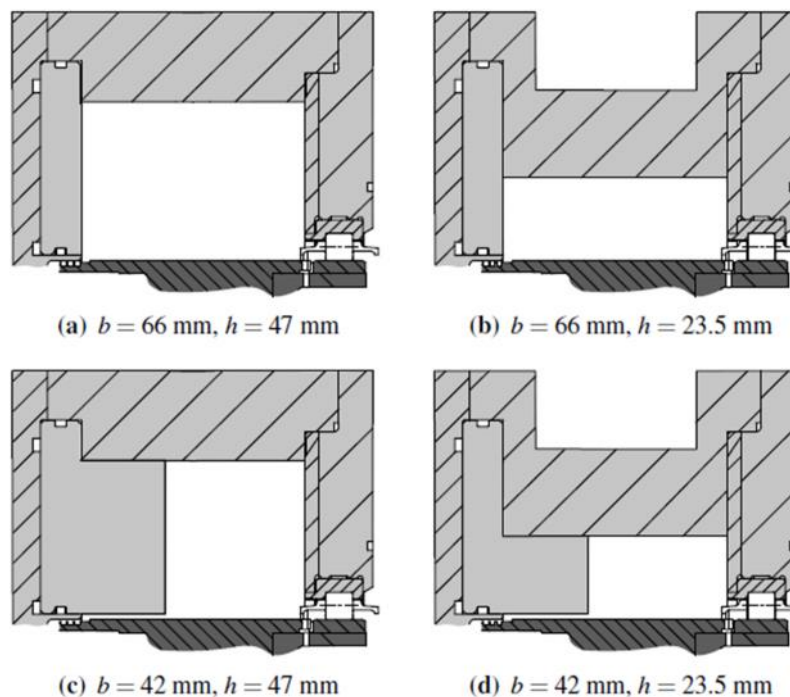


Figure 1.15. Cross sections of the four investigated bearing chambers

All parameters that define an operating point, as well as several additional control parameters were permanently measured and recorded. This includes shaft speed, oil supply

flow rate, air pressure, temperatures, scavenge flow rate, and air and oil outlet flows. Furthermore, the outer ring of the test chamber was equipped with capacitive film thickness sensors at nine different circumferential positions.

It was identified two distinguished flow regimes (see Fig.1.16) and showed their influence on the film flow inside bearing chambers.

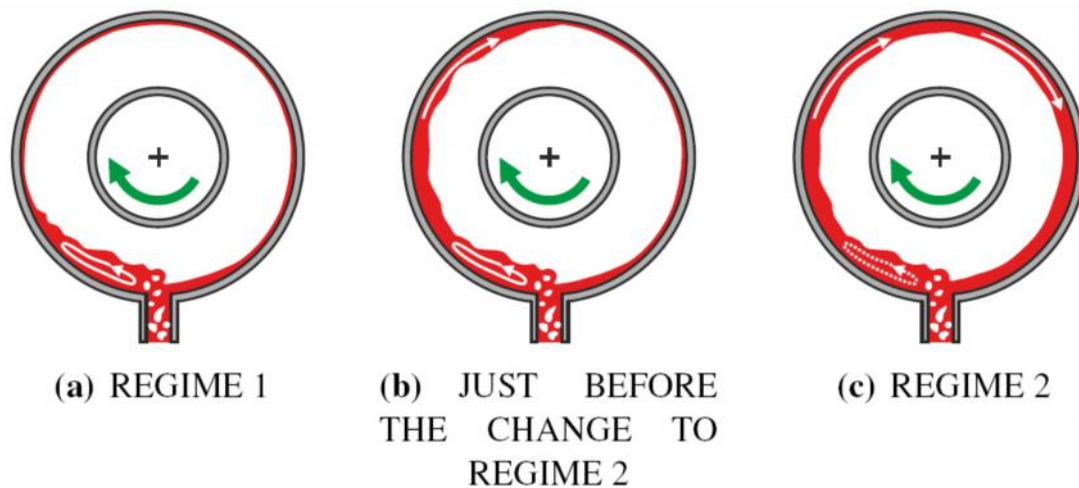


Figure 1.16. Schematic of bearing chamber flow regimes

The first regime occurred at lower shaft speeds, where the oil appears to be mainly driven by gravity. Figure 1.16a, shows a simplified schematic of that regime. The second regime, which occurred at higher shaft speeds, was characterized by a more homogeneous and rotating oil film (Fig. 1.16c). It was experimentally determined a significant influence of the flow regime on the scavenge efficiency, a parameter which describes how much oil is scavenged. It was also mentioned that the change from one regime to the other occurred at a specific shaft speed. The regime change was identified by observing the film thickness distribution along the circumference of the bearing chamber. When the regime changes to the second regime, oil suddenly flows against the direction of gravity from the left part of the chamber over the top into the right part. As a consequence the oil film thickens very abruptly in the right part of the chamber. This phenomenon was used as criterion for an objective determination of the change from regime 1 to regime 2. Changing of oil film thickness is shown in Fig. 1.17.

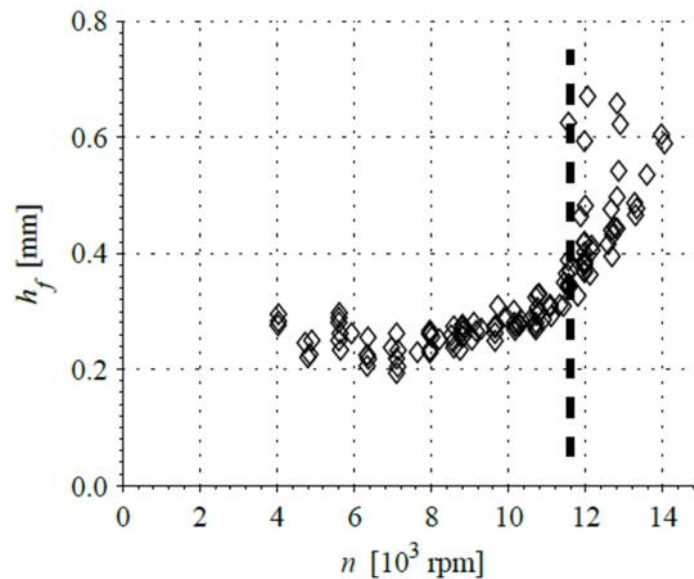


Figure 1.17. Film thickness at $\alpha = 315^\circ$ versus shaft speed (dashed line indicates regime change)

The paper represent interesting research that shows influence of bearing chamber dimensions on the operation parameters. The results had showed that the regime change occurs at a certain critical rate of momentum transfer, which is a function of the chamber outer diameter and of the oil flow rate. In general, the critical rate of momentum transfer decreases with increasing oil flow rate. In the cases where the oil flow rate from the bearing is too small to wet the upper part of the bearing chamber in the first regime, the chamber dimensions have a major impact on the critical rate of momentum transfer.

Paper [12] deals with the wall film dynamics of lubrication oil in the vicinity of the scavenge port of a typical aero engine bearing chamber. Paper presents studying of interaction of oilflow and airflow moved in one direction and in opposite direction, with various speeds and with the various incline angle.

Fig. 1.18 present the typical situation in bearing chambers where air is supported to the chamber to provide the operation conditions and oil moves on the walls under the gravity force. In this case in the right half of chamber the air moves along the oilflow direction, and in the left half of chamber air moves opposite to the oilflow direction. Co-current and counter-current regimes are studied. To provide the research, the new test rig was designed. It is shown at Fig. 1.19.

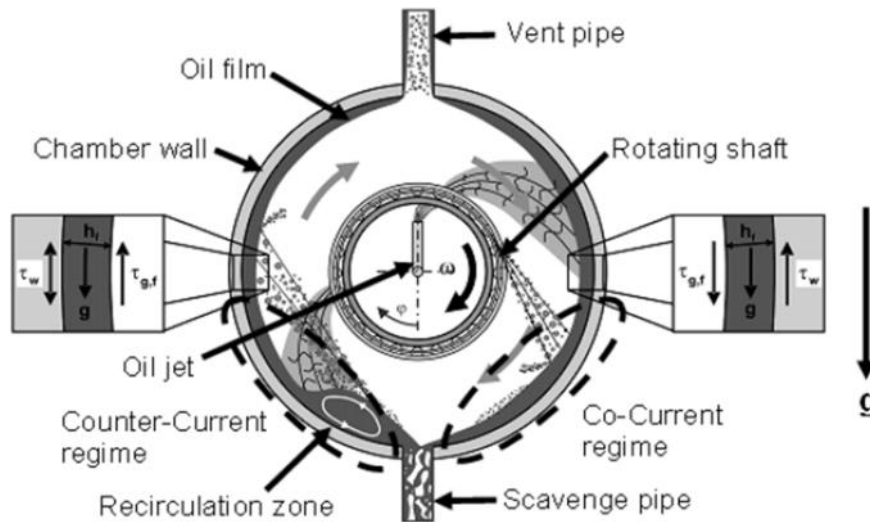


Figure 1.18. Two phase phenomena in model bearing chambers

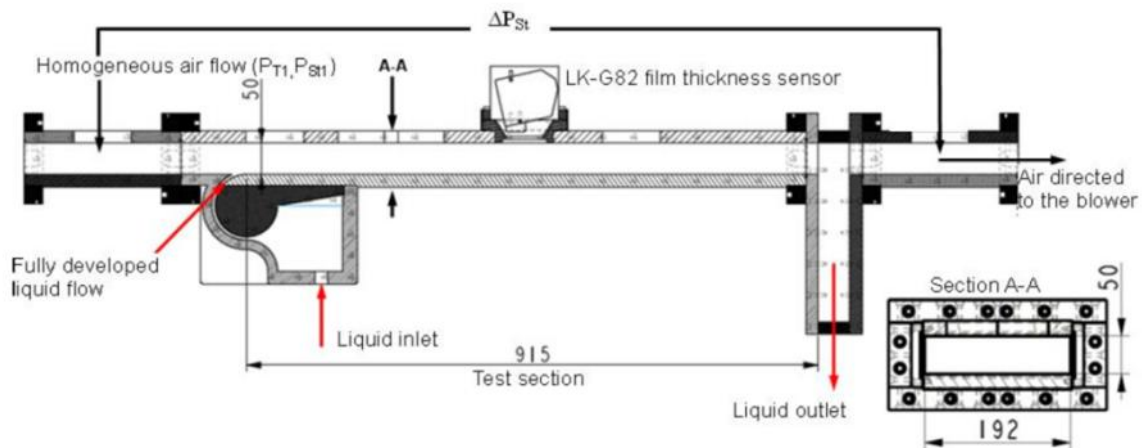


Figure 1.19. Schematics of stratified flow test rig

A transparent modular test rig with a rectangular cross-section (192mm x 50mm) and a test section length of approximately 915 mm (Fig. 1.19) was constructed. The large width of the test rig is to avoid considerable wall effects on the film flow. A uniform and homogenous liquid film is achieved by means of a compact pre-filming device designed in an iterative CFD procedure. The rig has a rotational degree of freedom of up to 45° to analyze cases under pure gravitational effects as well as combined gravitational and shear effects.

Water is chosen as working fluid because the viscosity and density of water at room temperature are similar to those of aero-engine oil at typical operating temperatures of 100...200°C.

A continuous increase in the inclination angle imparts an additional momentum to the film, which according to $L \cdot g \cdot \sin$ is governed by the film thickness and the gravitational force. For a constant film loading, the film experiences a continuous decrease in the thickness with the corresponding increase in velocity. At a critical inclination angle the film

thickness decreases to a point where the viscous force becomes equal to the gravitational force i.e. a transition from thick to thin film occurs.

It was found that the air experiences the oil film in both regimes as an additional resistance (in the test section); consequently the losses were proportional to the square of the mean air superficial velocity. With the help of qualitative analysis, the waveforms in the co-/counter-current flow regime are categorized. The qualitative analysis also indicates that the droplets in bearing chambers are most probably generated from the counter-current side. From the quantitative and qualitative analysis conducted in this paper, some plausible characteristics of the oil film dynamics near the scavenge off-take (in the absence of coexisting flow phenomena e.g. droplet interaction, off-take disturbance etc.) can be summarized, which are represented in Tab.1.1 as follows:

Table 1.1. Characteristics of the oil film dynamics

For co-current regime:	For counter-current regime:
<ul style="list-style-type: none"> • flat surface or shallow waves; • very low probability of droplet shedding; • laminar/nearly laminar; • supercritical; • can be considered as fully developed; • almost no churning loss. 	<ul style="list-style-type: none"> • big solitary waves; • droplet shedding; • turbulent; • sub-critical; • definitely undeveloped; • large churning losses.

Experiments gives us the understanding of difference between co-current and counter-current moving direction of air and oil. But many operation conditions parameter are did not observed in the paper, especially, temperature, incline angle up to 90°, using the oil itself instead of water, moving on the circle direction and others. Additionally the represented test rig can be used only to research the current phenomena.

Paper [13] deals with the measuring of residual volume of oil, film thickness using laser scanning displacement meter and void fraction depends on scavenge ratio (oil flow) and rotor rotation speed. The presented test facility consists of a test rig, shown in Fig. 1.20.

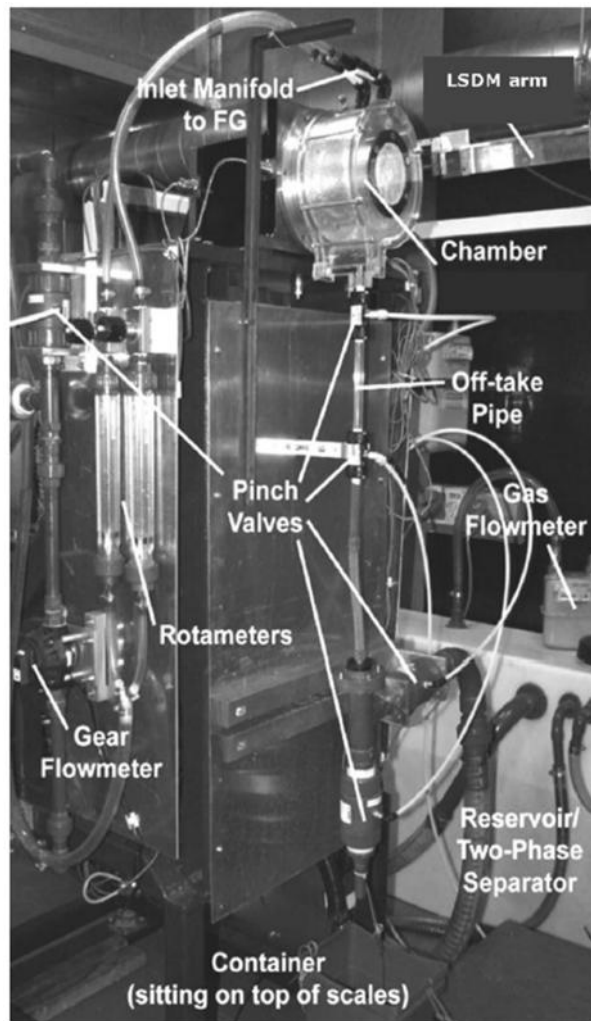


Figure 1.20. Nottingham scavenge test rig

The inner geometry of the chamber is a simple smooth cylinder without any of the complexities that can be found in a typical aircraft engine bearing chamber (such as various baffles, struts, bolts, protrusions, etc.). The simplified geometries allow for a focused study on the main flow physics and to build a firm knowledge base. A polycarbonate (Lexan) reinforced window allows for safe visual observation of the test rig from the control/observation room.

Water is chosen as the working fluid. The physical properties of water at room temperature are similar to those of engine oil (Mobil Jet Oil II) at temperatures typical of aircraft engine operating conditions.

Water from a reservoir tank is drawn by an inlet pump and is introduced into the chamber via two types of inlet systems: film generator (FG) and rotating inlet distributor (RID). The film generator introduces the water directly onto the wall of the chamber where it travels as a film towards the sump.

The rig employs a circuit of pipe work which carries water and air and this is shown schematically in Fig.1.21. In this circuit, water flows in a closed loop, whereas air flows in an open loop. A sealed polyethylene baffled water tank is used as a reservoir. Water is pumped into the chamber by an inlet pump, flowing through some pipe work, globe valves, flow

meters, and into the inlet system (FG or RID). The inlet pump runs at constant speed and the inlet flow rate is set by adjusting the globe valves and measured using the rotameters indicated. The chamber is open to atmospheric pressure. A vent hole on the front plate of the chamber allows ambient air to enter into (or out of) the chamber freely.

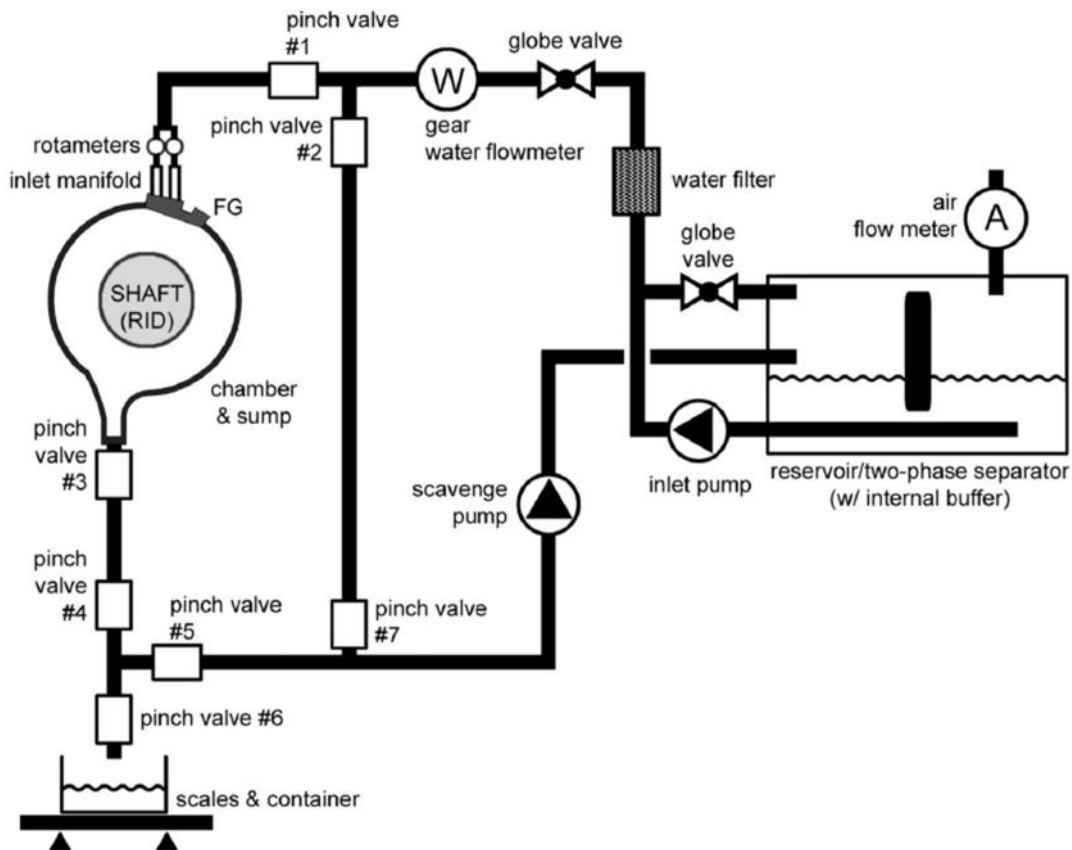


Figure 1.21. Schematic representation of the water-air circuit

Efficiency of process is measured using the ratio of total exit volume flow rate, Q_{tot} , to inlet liquid volume flow rate, Q_l , is defined as scavenge ratio, SR:

$$SR = \frac{Q_{tot}}{Q_l} = \frac{Q_l + Q_g}{Q_l} = 1 + \frac{Q_g}{Q_l}$$

The total exit volumetric flow rate, Q_{tot} , is the summation of the outlet liquid flow rate, Q_l , and the ingested air flow rate in the offtake, Q_g .

The residence volume (the amount of oil instantaneously present in the chamber at any time) is a measure of performance. A good sump is one in which liquid and gas undergo minimal mixing and from which liquid is quickly drained out, minimizing residence volume.

It is possible to view the state of the two-phase flow in this pipe and also, by simultaneously closing valves #3 and #4 (Fig. 1.8), to capture the liquid present in that pipe section. Void fraction is the volume fraction of the off-take pipe ($V_{off}=17$ cc) that is occupied by gas (void). It is obtained by measuring the liquid volume in the off-take, $V_{l,off}$.

$$r = \frac{V_{off} - V_{l-off}}{V_{off}} = 1 - \frac{V_{l-off}}{V_{off}}$$

Film thickness measurements were made optically using a Keyence LT-9030M confocal laser scanning displacement meter.

A curved wall deep sump (CWDS) geometry has been investigated and data compared where available to that previously obtained for a geometrically scaled version of the same geometry with a somewhat different liquid supply method.

Summary it can be notes that, in general, the residence volume of this CWDS is a weak function of inlet liquid flow rate and shaft speed. For all cases with FG, residence volume is insensitive to variation in scavenge ratio. The void fraction of the CWDS is only a weak function of inlet liquid flow rate and shaft speed. The film thickness of the CWDS depends on shaft speed and is a weak function of inlet liquid flow rates. It should be added that using the water instead of oil can give some mistake to the experiment.

Paper [14] presents the changing of oil film thickness on static surfaces near an aircraft engine ball bearing depending on the input oil flow rate.

The bearing oil shedding test rig includes a high-speed, single drive unit that drives the test bearing with a pitch circle diameter of approximately 260 mm. A cross-sectional isometric view of the rig is shown in Fig. 1.22.

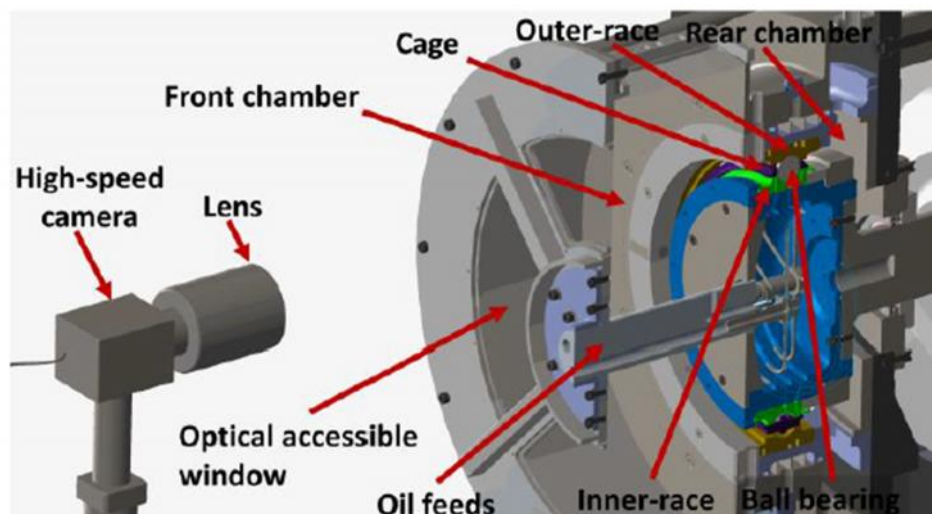


Figure 1.22. Isometric cross-sectional view of oil shedding test rig

The range of operational speed for the present experiments was 0-7,000 rpm. The test bearing assembly consists of an under race fed ball bearing with inner and outer races and a bearing cage. Oil is fed to the bearing at 3 axial locations through a series of holes that lead from an annular region. The oil feed arrangement to the annular region is different on the rig compared to what might normally be found in an aircraft engine. On the rig a series of delivery tubes feed oil into separate compartments for feed to the three locations in the inner race and under the cage front and rear. The flow through each of these three locations can be independently controlled. In the testing conducted two flow rates were employed viz. 5.2 liters per minute and 7.3 liters per minute. The axial load is provided by an electromagnet actuator capable of generating up to 35 kN of axial force which pulls the shaft towards the drive and away from front chamber.

The oil heats up as it passes through the bearing and there are four thermocouples embedded in the chamber walls near to the bearing. Oil exiting the bearing at the rig front and rig rear is separately removed using two scavenge pumps. There is also a vent pipe situated at the top section of both chambers, included to reduce to a minimum any pressure difference across the bearing and to keep rig operating pressure close to ambient.

The front chamber provides optical access and has removable front windows. These windows are positioned at angular positions 0° , 90° , 180° and 270° with top-dead-center denoted as 0° (Fig. 1.23). The use of the LDM (long distant microscope) coupled with the high speed camera enabled the investigation of film flow dynamics within a very small region of interest ($0.01\text{m} \times 0.01\text{m}$). The imaging was carried out at three axial planes in the bearing compartment: 3 mm, 10 mm and 36.8 mm from the front of the compartment with the latter plane approximately central to the bearing cage. Two viewing positions at 90° and 270° were considered: 90° is the co-current side where the interfacial shear and gravity act in same direction to produce additive effects. 270° is the counter-current side in which the above mentioned forces are oppose each other. The reason behind measuring oil film thickness () at three different axial planes is to assess its variation as the oil exits from the bearing and flows axially outwards towards front face from where it finally exits to bearing chamber.

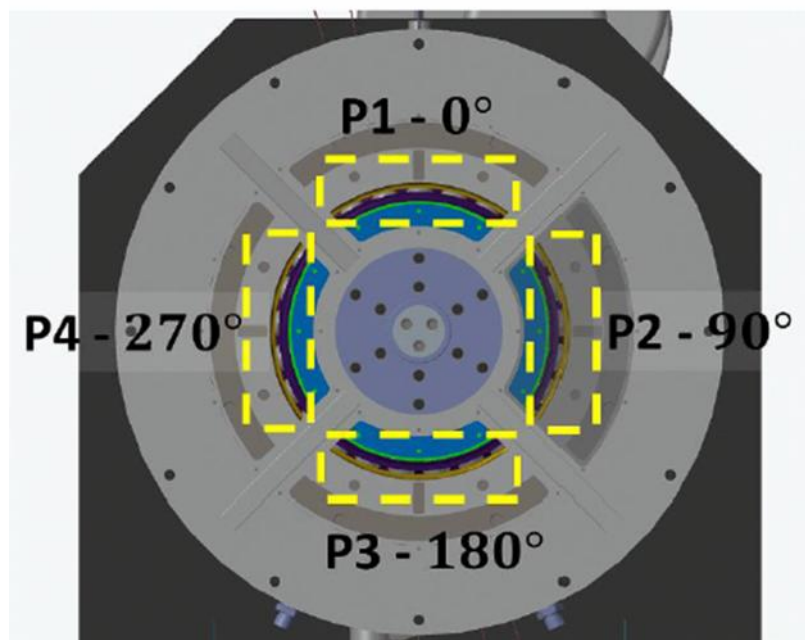


Figure 1.23. Convention for angular positions

High speed (HS) imaging is used to obtain the data that is analyzed to yield film thickness. This technique is non-intrusive, does not-interfere with the main flow and requires no change to existing bearing geometry for utilization. It also eliminates known calibration errors associated with bubble entrainment in liquid present with capacitive and ultrasonic measuring techniques. The images are taken with a high speed camera (IDT vision Os4v3). The resolution of the sensor is 1024×1024 pixels with maximum frame rate of 6,000 Hz at this resolution. With a reduced region of interest (ROI), the frame rate can be enhanced.

The oil film thickness profile is time-dependent, wavy and is formed by quasi-periodic phenomena. The steady-state features in an image are determined prior to measuring the

film thickness. In the present work, oil film thickness (δ) is calculated from 8-bit gray scale images obtained from LDM-HS imaging using the image processing technique of ‘median stacking’. This technique is more commonly found in astronomy applications, but is applicable here also. As a result the steady-state oil film thickness profile is obtained. The median stacking was performed using MATLAB R2015a. The process of oil film thickness (δ) determination from the median stacked image is detailed as follows and with reference to Fig. 1.24.

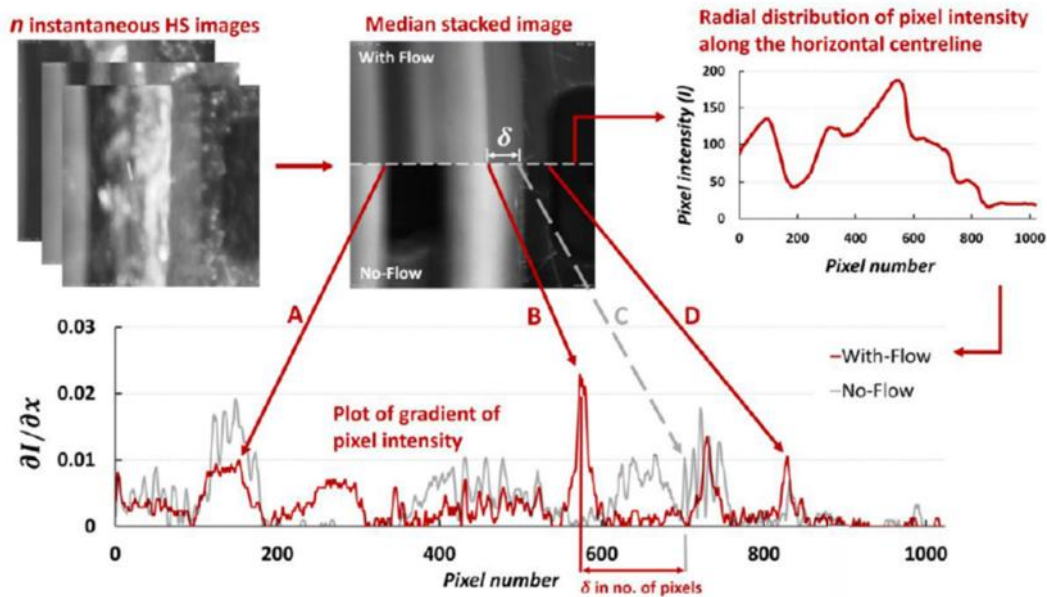


Figure 1.24. Determination of oil film thickness (δ)

It was observed that for all axial planes of measurement in both co-current and counter-current regions film thickness decreases with increase in shaft rotational speed. At 5,000 and 7,000 rpm film thicknesses are around 1 mm to 0.75 mm and are similar at 90° and 270°; at 3,000 rpm films tend to be somewhat thicker at around 1.5 mm – 2 mm and are thicker in the counter current region, particularly closer to the bearing. It is suggested that at higher shaft speeds interfacial shear dominates whereas at lower speed the effect of gravity in slowing the film in the counter-current region causes a measurable difference.

It was further observed that increasing the input oil flow rate from 5.2 liters per minute to 7.3 liters per minute did not produce significant effect on film thickness. However, the increase of axial bearing load from 10 kN to 30 kN yielded thicker films at the location above the cage.

It should be noted that experiment includes only under race lubrication method and rotational speed are slow comparing with the real aircraft engines. Additionally measurement error of this method was not calculated.

1.3 Investigation of oil droplet flow behaviour.

Paper [15] gives review of three groups of droplet impingement on surfaces:

- investigations of droplet impingement on heated surfaces, in which the temperature is above the evaporation temperature of the fluid;
- investigations of droplet impingement on cold surfaces;

- investigations of droplet impingement on films.

The liquids used to establish the different viscosities and surface tensions were ethanol, water and a mixture of water-sucrose-ethanol.

The model of deposition-splashing of the droplet is obtained using the energy and conservation:

$$E_k + E_p + E_s = E'_k + E'_p + E'_s + E'_d$$

$$m = m'$$

where E_k , E_p , E_s and E_d are the kinetic, potential, surface and dissipated energies, and m and m' are the mass of the droplets before and after impact, respectively.

Scheme of test rig for impingement and deformation process of droplets on a rigid cold is presented on Fig. 1.25.

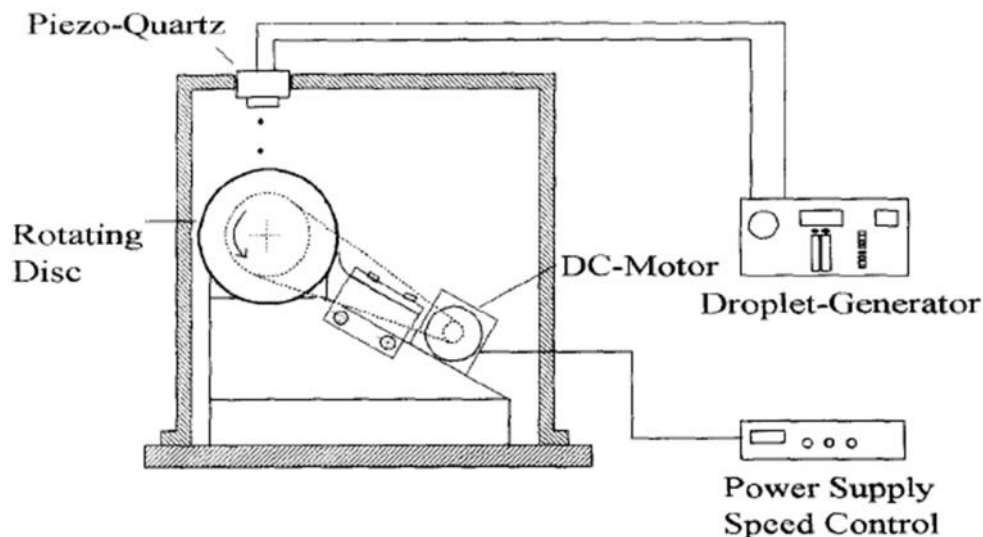


Figure 1.25. Schematic overview of the test rig

Two different rotating discs were used during the experiments. Disc 1 had a technically smooth mean roughness height (i.e. $R = 2.8/\mu\text{m}$) and disc 2 had a roughness height in the range of the impinging primary droplet diameter (i.e. $R = 78/\mu\text{m}$). A droplet generator produces a stream of monodisperse droplets in the size range of 60- 150 μm and a repetition rate of 28-65 kHz. Rotating disc with the circumferential velocity can be varied in the range of 1.3-39.3 m/s. Some instruments are used to provide the needed measurements: camera and LED for visualization; two-color phase Doppler anemometer for measuring the droplet velocity.

Experiment was provided both for the two disks with various roughness (smooth disk and rough disk) and for the different Reynold numbers. Behavior of droplet interaction with the wall was described in each case. Fig. 1.26 shows the visualization of investigated process.

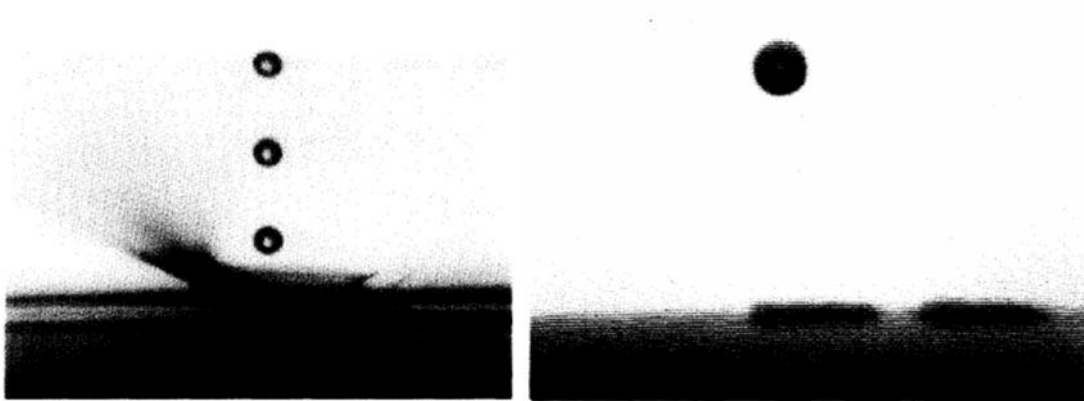


Figure 1.26. Splashing of a liquid droplet (left) and deposition of a liquid droplet (right)

Additionally the droplet sizes, impingement angle, velocity values and velocity vectors were measured while providing the experiment.

Paper [15] presents the essential investigation that can give the explanation of using the rough and smooth surface of veering chamber. But the test rig doesn't represent the separate bearing chamber. It can be considered only as additional separate instrument for investigation of droplet-wall interaction.

The paper [16] deals with oil droplet flow phenomena in aircraft engine bearing chambers. An experimental investigation of droplet sizes and velocities utilizing a Phase Doppler Particle Analyzer (PDPA) has been performed in bearing chamber. Influences of high rotational speeds are discussed for individual droplet size classes. Authors use the test rig with 2 chambers (I and II) updated to the current research as it is shown at Fig. 1.27.

PDPA measures the distance of scattered fringe patterns, which are generated by single droplets passing the measuring volume in the intersection of two laser beams. By use of two or more photomultipliers separated by fixed spacing, the fringe patterns of droplets moving through the beam intersection region are analyzed by use of the phase shift between the signals of the detectors. This phase shift shows for each scattering mode (i.e., reflection, first and higher orders of refraction) a linear relationship to the droplet diameter.

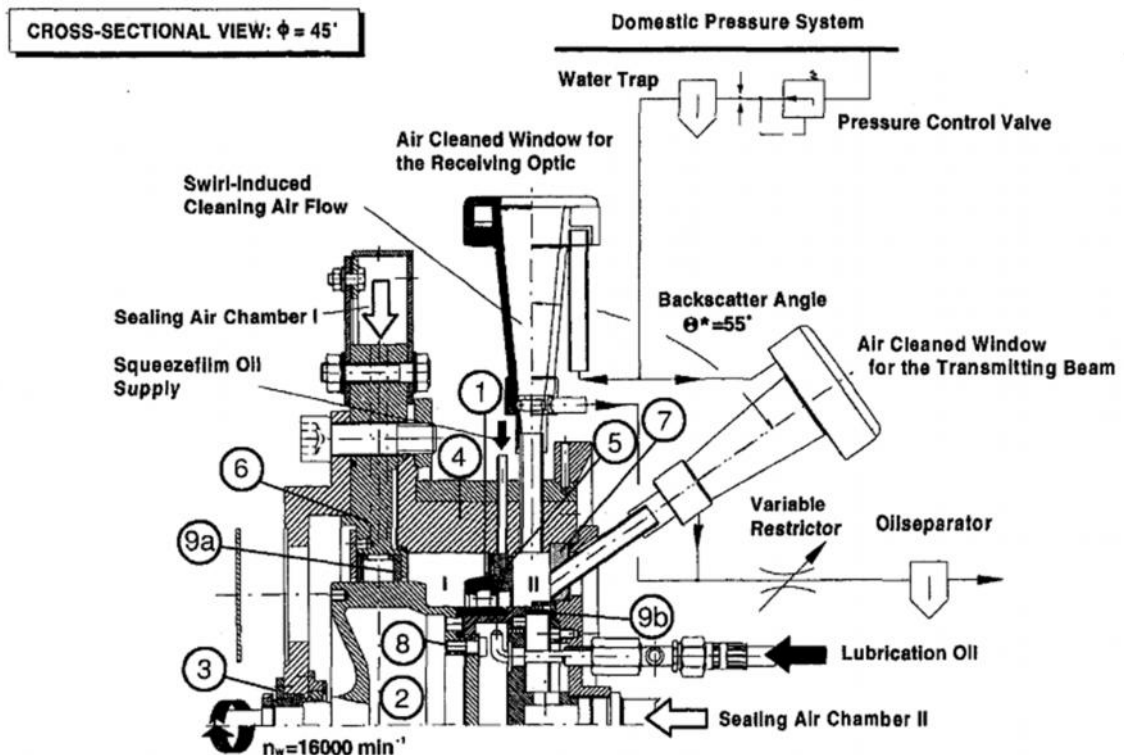


Figure 1.27. Updated high-speed bearing chamber test rig

Measurements have been performed for real engine conditions as described by sealing air flows and lubrication oil flows of $\dot{m}_{II} = 10 \text{ g/s}$ and $V_{II} = 100 \text{ l/h}$, respectively, and rotational speeds up to $n_w = 16,000 \text{ min}^{-1}$. As a result, mean values for the droplet velocity components in the radial and tangential directions according to the PDPA setup described above are shown for three discrete droplet diameter classes in Fig. 1.28 as a function of rotational speeds. It can be readily seen from the figures that the droplet flow is strongly influenced by the circumferential velocity of the rotor.

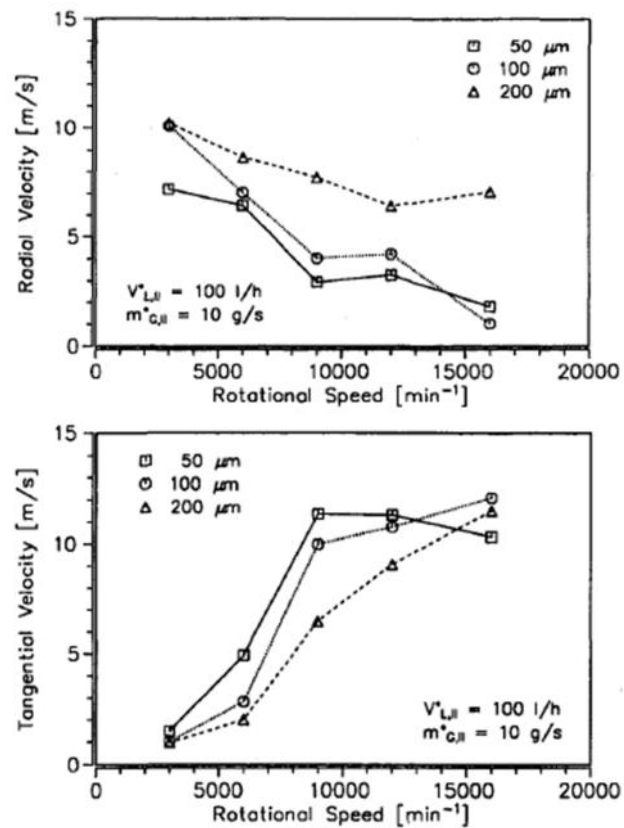


Figure 1.28. Mean radial (left) and tangential (right) velocity versus rotational speed

In general, the radial velocity of the droplet decreases, whereas the tangential velocity component strongly increases with an enhancement of the shaft speed. Thus, it can be concluded that the droplet flow angle is changing from a radial to a tangential direction, reflecting a dominant effect of air flows to the vent at low speed and dominant influences of rotating core flows inside the chamber at high speed conditions, respectively. With the exception of the highest speed of $n_w = 16,000 \text{ min}^{-1}$ this is more significant for small droplets. Larger droplets are accelerated by the rotation, but keep a radial velocity component even for high-speed conditions due to their inertia.

Droplets characterized within the experiments are exposed to the flow field of the gaseous phase predicted by use of CFD code EPOS. The aim of the numerical study is rather the qualitative visualization of the flow regime than the prediction of quantitative results. The gaseous phase of the two-phase flow in the bearing chamber is described by an Eulerian approach, whereas the dispersed phase is calculated within a Lagrangian frame of reference. The repercussion on the gaseous phase caused by the liquid phase is neglected.

An analysis of droplet flow phenomena in combination with numerical methods requires information on each individual droplet characterized by its diameter and velocities. In the present paper authors have investigated in detail the operating condition shown in Fig. 1.29 where the droplet diameter histogram for $\dot{m}_{II} = 10 \text{ g/s}$ and $V_{II} = 100 \text{ l/h}$ at rotational speeds $n_w = 12,000 \text{ min}^{-1}$. It represents a total number of 3000 valid samples and ranges from approximately $14 \mu\text{m}$ to $500 \mu\text{m}$ in diameter. The number distribution shows a maximum at diameters from $70 \mu\text{m}$ to $80 \mu\text{m}$.

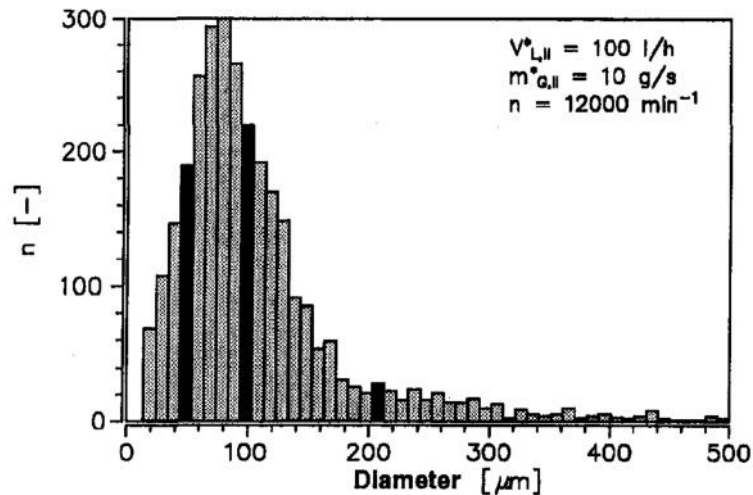


Figure 1.29. Diameter histogram

However, it can also be seen that larger droplets, i.e., $>200 \mu\text{m}$, must not be neglected. From the measured diameter distribution, droplet classes referring to those discussed above (dark bins) have been separated and the velocity distributions for both, the radial and the tangential components, have been extracted from the raw data.

Paper [17] deals with the studying of droplet generation and their propagation inside bearing chamber using the SPIV (stereoscopic particle image velocimetry) technique. Test rig consists of 2 chambers is shown in Fig. 1.1. Additionally paper describes the difference between two bearing designs – with fillets and without fillets (Fig. 1.30).

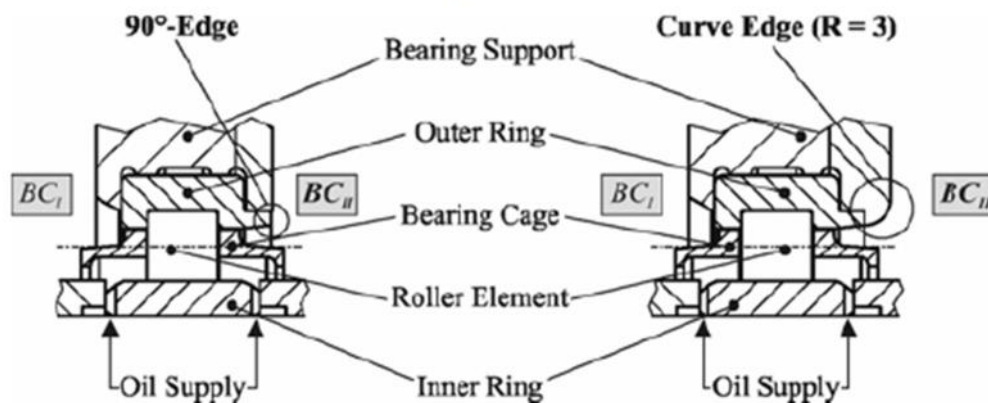


Figure 1.30. Design of bearing support: 90°-edge (left) and curved edge (right) between the outer ring and the support

The major part of the experiments concentrated on the droplet generation and their propagation inside chamber II. Therefore, SPIV (Fig. 1.31) was used to determine three dimensional droplet trajectories. In this paper only the adaptation to the bearing chamber test rig is covered.

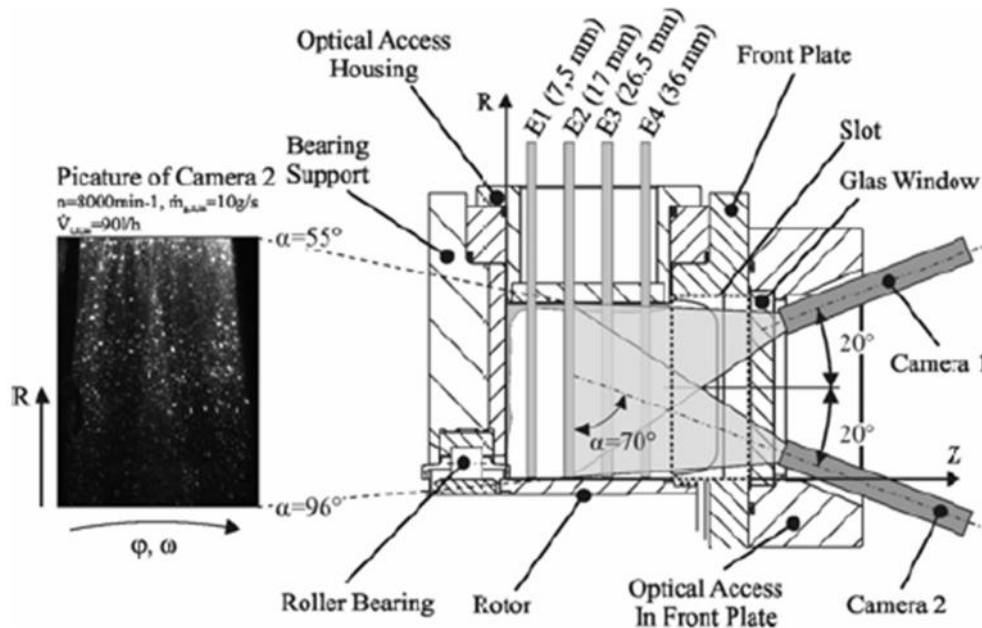


Figure 1.31. SPIV inside the bearing chamber

A double-cavity Nd-Yag Laser provided a Laser beam with a wavelength of 532 nm which was then transformed into a plane light-sheet with a thickness of 2 mm. In order to guide the light-sheet into the bearing chamber a plane window with a height of 40 mm was mounted to the housing in a position 90° downstream of the vent port. The light-sheet-optics was placed on a traverse in order to allow the investigation of four planes at different axial distances to the roller bearing (Fig. 1.31). Preliminary test of the system revealed that the light sheet was slightly distorted after crossing the oil film covering the inner surface of the housing and the window. An exemplary “raw” exposure is shown in Fig. 5. The droplet displacement was observed by two 12bit-Double-Shutter-CCD cameras (1280x1024 Pixel) positioned in a 20° angle to the normal vector of the light sheet.

The results revealed that the generation of droplets only occurred in the test rig for very limited conditions but can be controlled by the design of the bearing support and the operating conditions of the engine. The probably most important parameter is the axial airflow through the bearing which is induced by a pressure difference across the bearing. Reducing the pressure difference leads to a reduction of the droplets generated. Based on flow visualizations and a determination of droplet velocities by stereoscopic particle image velocimetry an improved understanding was derived to describe the droplet generation by roller bearings for a wide range of operating conditions. The paper presents only experiment without comparing of its results with the some model to find some relations: these relations can help to model the analogue operation conditions.

1.4 Investigation of air flow behaviour.

The test rig in [8] presents the modification of test equipment showed in Fig. 1.1. It is used for measuring of the local air / oil flow field. In the present study experiments have been carried out to determine the rotating and swirling pure airflow. Current test equipment shown at Fig. 1.32 has smaller bearing chambers.

Here the roller bearing was replaced by a so called bearing simulator. The design of the simulator maintained the main geometrical dimensions. Compared to the roller bearing the outer ring, the roller elements and the cage were merged to one single non-rotating part. The effect of the simplifications seemed to be negligible regarding the small size of the cage compared to the bearing chamber.

The mass flow rates were measured by calibrated orifices, with an error for the differential mass flow of less than 1%. The air temperature was measured in the test rig upstream the labyrinth seals and at several positions in the chamber itself using thermocouples type K. The measurements of the airflow were conducted in an angular plane of bearing chamber II. Since the flow field was assumed to be three dimensional a specially adapted 3D-LDA system was used.

The set-up of the 3D-LDA system is shown in Fig. 1.33. Argon-Ion laser in multi-mode operation and with a maximum light intensity of $P_{\max} = 10W$ was used as the light source. The entire system includes a transmitter box, two fibre-probes, one photomultiplier tube and one Burst Spectrum Analyzer (BSA) for each channel as well as the BSA Flow software.

The velocity field inside a bearing chamber was determined for fifteen different operating conditions. Measurements were conducted for four different rotational speeds ranging between $n = 3000\text{min}^{-1}$ and $n = 13000\text{min}^{-1}$ and various flow rates between $m_{\text{II},\text{in}} = 4.2\text{g/s}$ and $m_{\text{II},\text{in}} = 17.0\text{g/s}$. It should be mentioned that only a negligible airflow of about 1-2% of the total flow rate $m_{\text{II},\text{in}}$ left the bearing chamber II through the bearing simulator. In addition, the conditions in the chamber had been kept constant at a pressure of $p_{\text{II}} = 2.5$ bar and a temperature of $T_{\text{II}} = 298$ K.

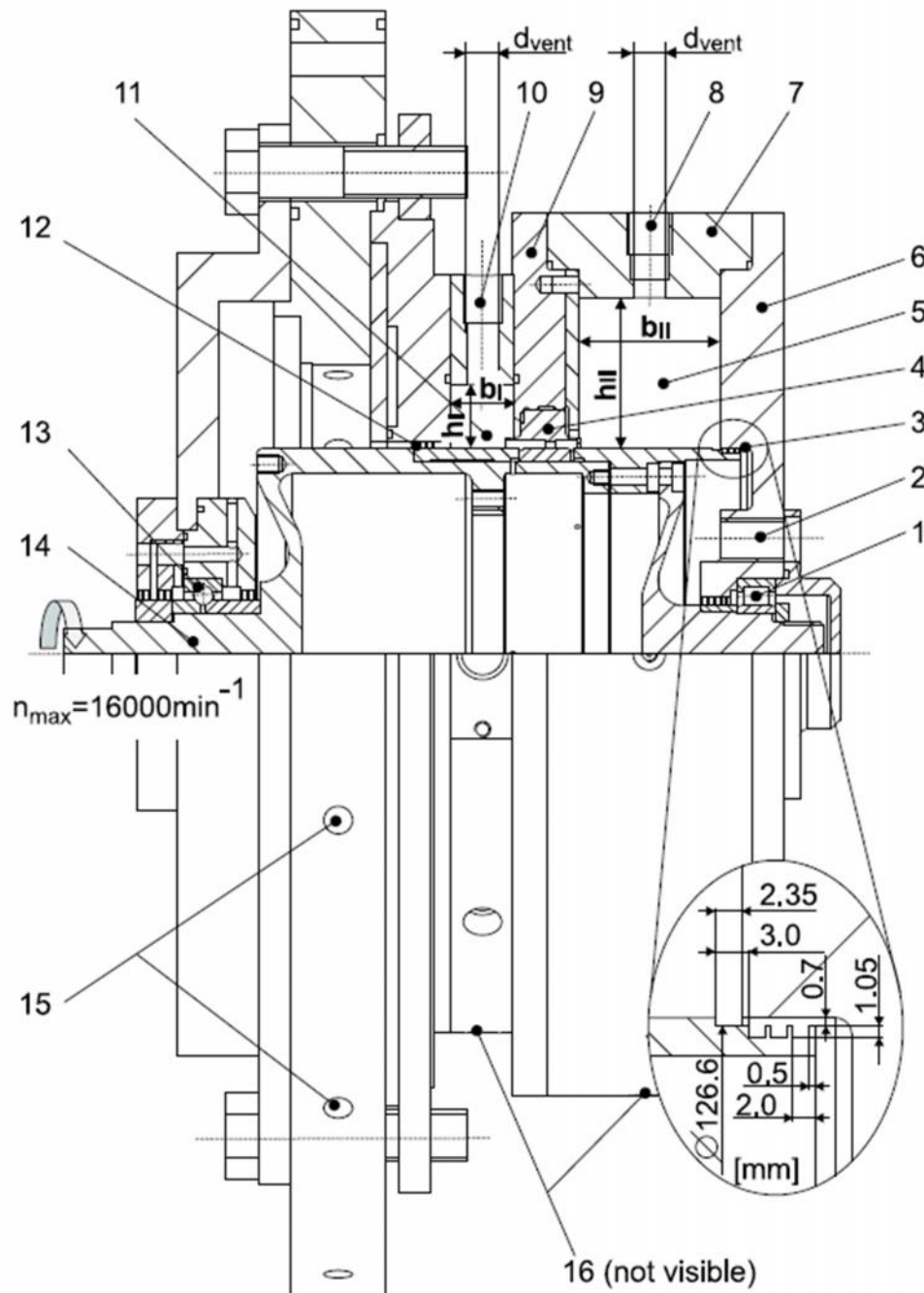


Figure 1.32. High speed bearing chamber test rig:

- 1 – cylindrical roller bearing; 2 – air supply bearing chamber II; 3 – labyrinth seal II;
- 4 – bearing simulator; 5 – bearing chamber II; 6 – front plate; 7 – bearing chamber housing; 8 – vent port II; 9 – bearing support; 10 – vent port I; 11 – bearing chamber I;
- 12 – labyrinth seal I; 13 – ball bearing; 14 – rotor; 15 – air supply bearing chamber I; 16 – scavenge ports.

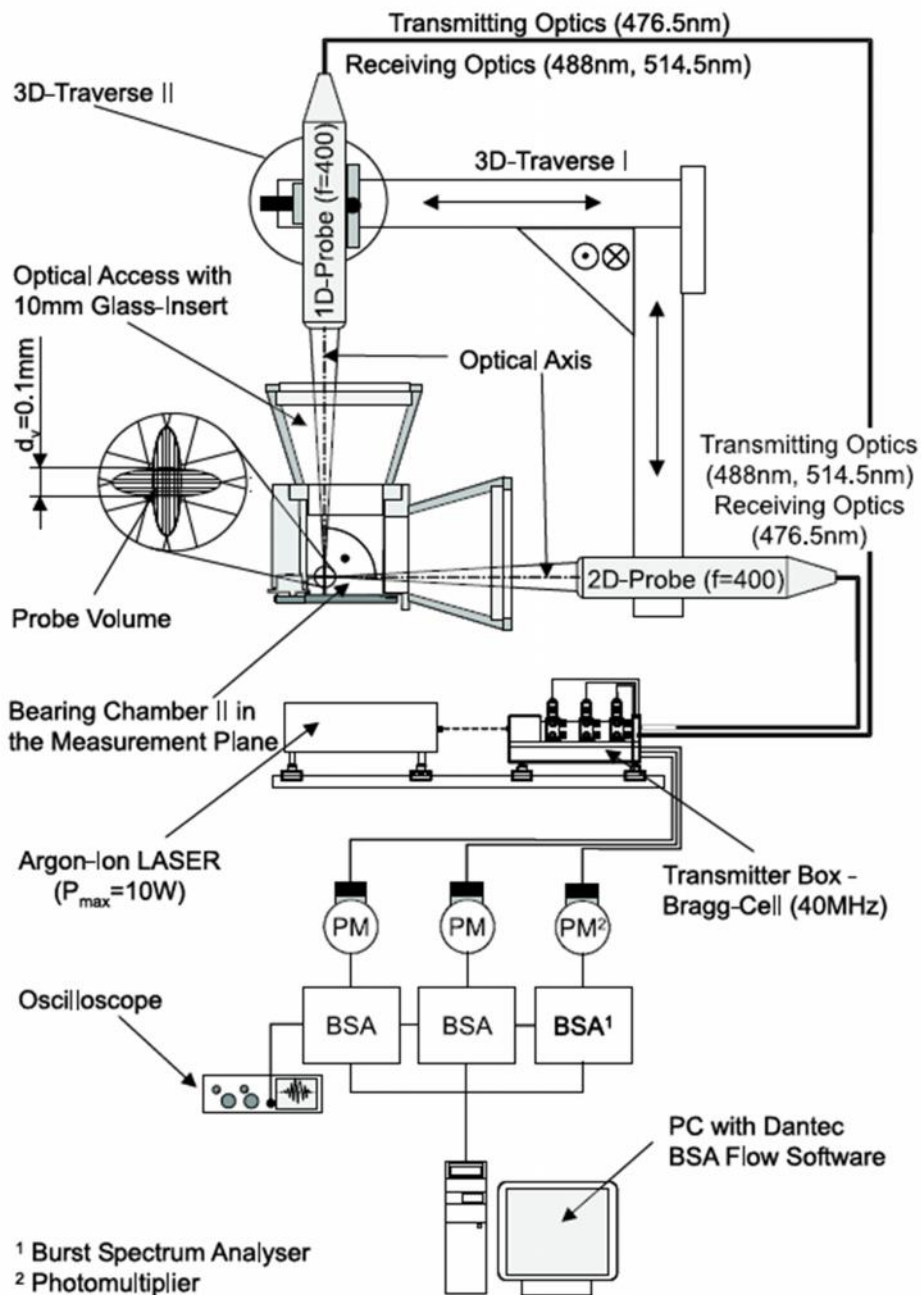


Figure 1.33. 3D-LDA technique applied to the bearing chamber test rig

The three velocity components (u_{rad} , u_{tan} , u_{ax}) were measured at 81 points in one angular plane - nine points in the radial direction and nine points in the axial direction. The excellent optical access to the test section allowed measurements in the near wall region as indicated in Fig. 1.34.

Fig. 1.35 summarizes the structure of the flow field for the wide range of operating conditions investigated. For a constant shaft speed, e. g. $Re_u = 450 \cdot 10^3$, and a low airflow rate the flow field is dominated by the rotational speed. Increasing the airflow above $Re_{in} = 110 \cdot 10^3$ the influence of the sealing air became dominant. However, if the shaft speed is increased

starting from $Re_u = 150 \cdot 10^3$ the transition between the rotational speed driven mode (RSDM) and the sealing air driven mode (SADM) occurred at linearly increasing airflow rates.

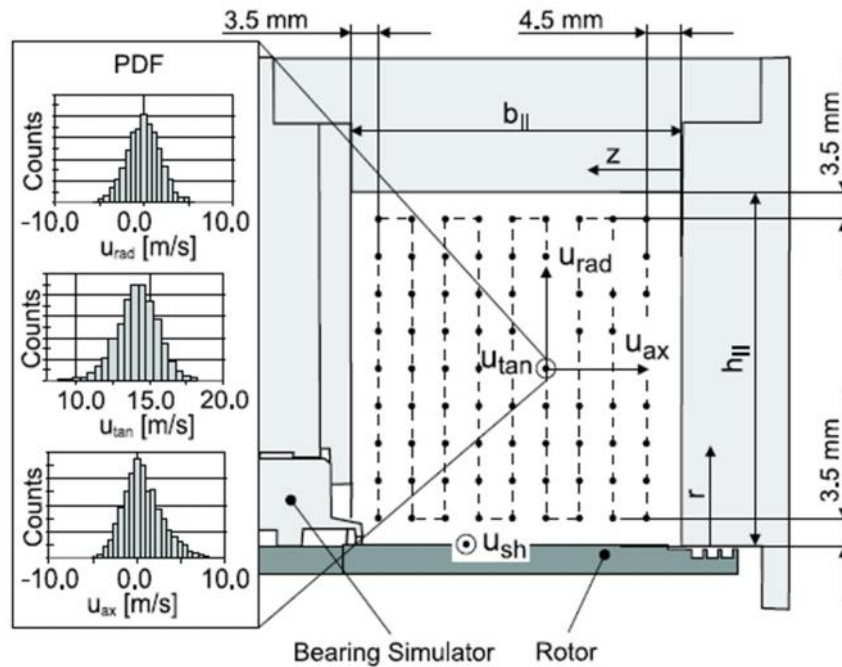


Figure 1.34. Measurement points in the measurement plane

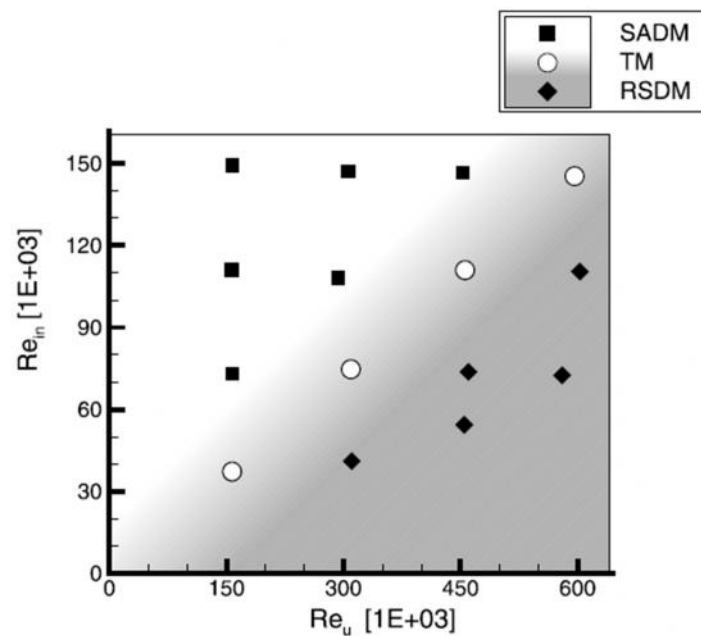


Figure 1.35. Characterization of the flow field for different operating conditions: RSDM – rotational speed driven mode, SADM – sealing air driven mode, TM – transient mode.

The knowledge gained in the present study contribute to the development of modern numerical models to predict the air-oil flow in bearing chambers. The pure airfield inside a bearing chamber was determined experimentally. The rotational speed and the sealing airflow were varied systematically in a wide range. The results revealed that the flow field strongly depended on the ratio between the velocity of the surface of the shaft and axial velocity at the inlet of the bearing chamber.

1.5 Investigation of heat transfer.

Paper [4] uses the test rig (Fig. 1.1) with modified size of bearing chambers and increased amount of thermocouples. Air/oil flow heat transfer measurements at the internal bearing chamber walls are described utilizing the temperature gradient method. It is a stationary technique based on a two-dimensional finite element calculation procedure. Based on measured temperature of housing wall, each boundary node of the finite element mesh can be interpolated and, finally the temperature distribution inside the housing wall can be determined iteratively by use of the finite element code. Thermocouples were mounted according to the Fig. 1.36.

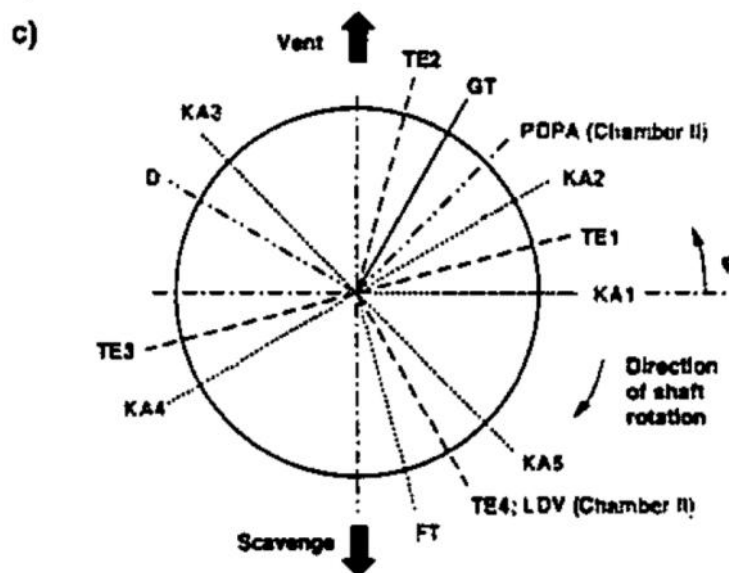
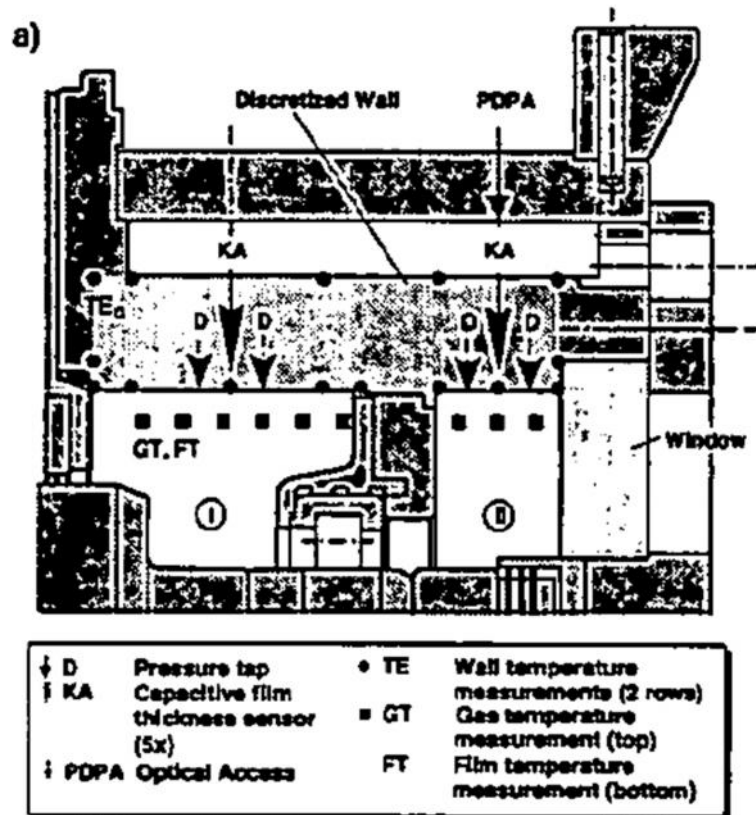


Figure 1.36. Scheme of thermocouples (TE) mounting: a) co-axial sectional view; c) instrumentation survey.

Experiments had been provided to study the influence of various factors on the heat transfer coefficients: a) operation conditions (see Fig. 1.37); b) geometry (see Fig. 1.38); c) circumferential direction (see Fig. 1.39).

Based on engine relevant pressure and temperature levels bearing chamber operating conditions are characterized by sealing mass flows, rotational speeds and lubrication oil flows and, therefore, their impact has been investigated in comprehensive studies. Typical dependences of local heat transfer coefficients in chamber I from operating conditions are shown in Fig. 1.37 where each influencing parameter has been varied independently with constant conditions for the remaining quantities. Fig. 1.39 shows influence of circumferential direction to the heat transfer coefficient in chamber I for all instrumentation planes (TE 1...4).

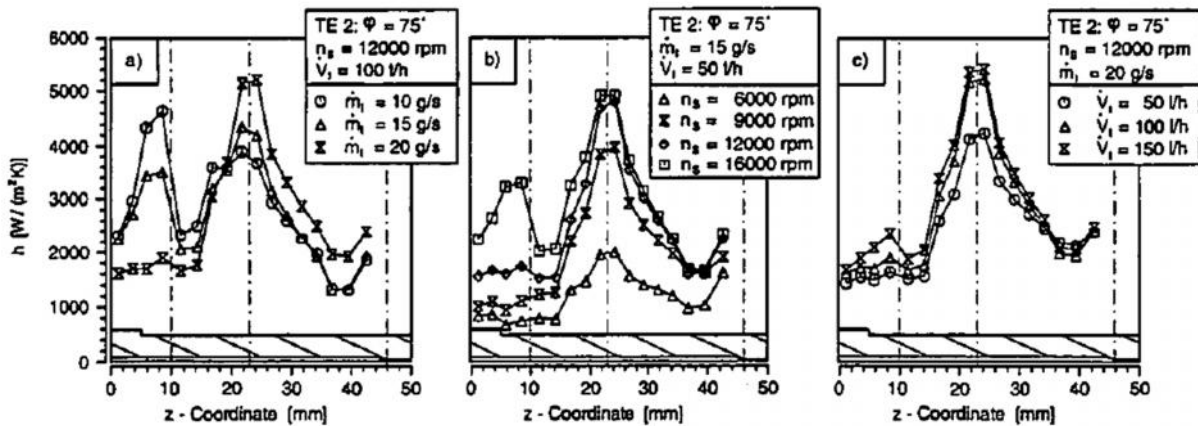


Figure 1.37. Influence of operation conditions on the heat transfer coefficient

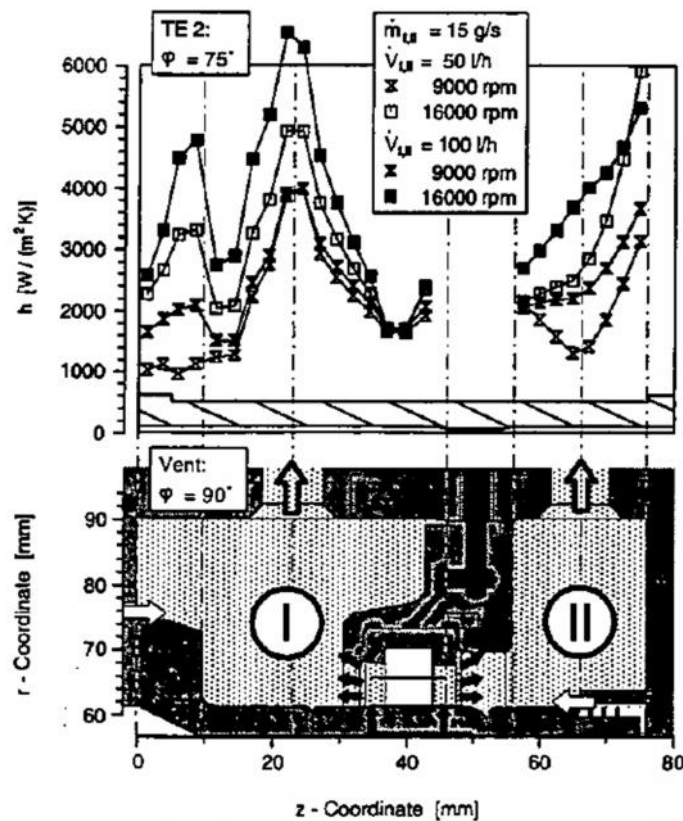


Figure 1.38. Influence of geometry on the heat transfer coefficient

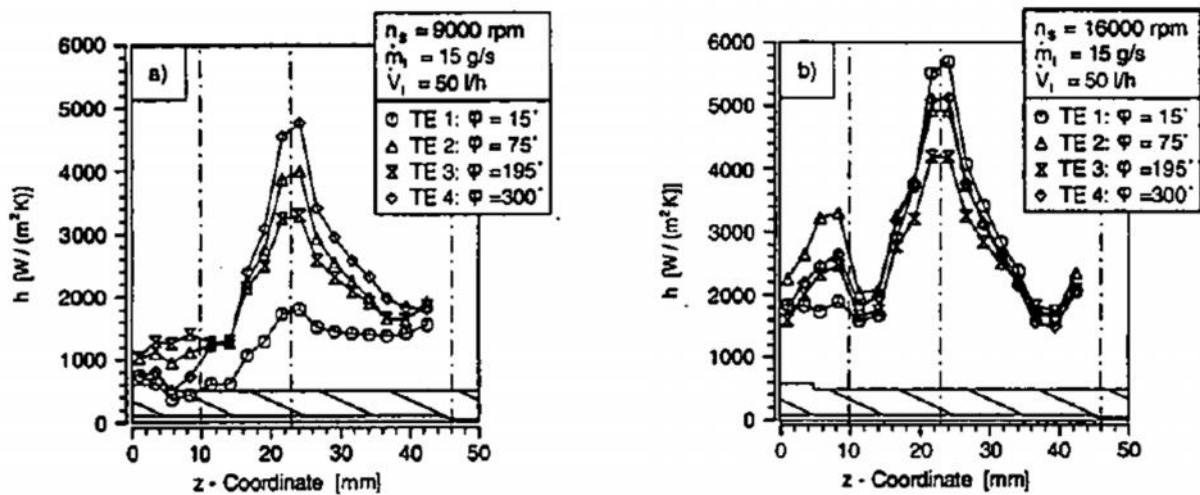


Figure 1.39. Influence of circumferential direction to the heat transfer coefficient

It has been shown that local heat transfer coefficients can increase dramatically up to values $h = 6000$ W/(m²·K) in regions which are exposed to impinging droplets, i.e. next to the vent port and in line with a disc or a shaft end at high speeds. Typical values for the highest speed condition of $n_s = 16000$ rpm range from 2500 W/(m²·K) $< h < 3500$ W/(m²·K). It should be noted that results of experiment were not compared with some theory or well-known approaches so it is hard to estimate the obtained values. Additionally the measure errors were not analyzed.

Research of bearing chamber wall heat transfer was made in [20]. To provide the experiment, it was used the test rig shown in Fig. 1.40 that represents the modification of test rig shown in Fig. 1.1. In the present study, the heat flux and heat transfer coefficients have been measured utilizing the temperature gradient method. It is the same experimental approach as chosen in [19].

Features of test rig:

- two bearing chambers (III, IV) for the investigation.
- oil flow rates up to 400 l/h;
- airflow to each labyrinth can be controlled independently and ranged between 5 g/s $< m < 20$ g/s;
- the water-cooled housing wall was adjusted and the thermocouples were artificially aged and individually calibrated in order to minimize uncertainties of the determination of the heat transfer coefficients.

Differences between both configurations of test rig (Fig. 1.1 and Fig. 1.40) are shown in Fig.1/41. Configuration 1, which was used by Glahn and Wittig [6, 7] and by Glahn et al. [19], consists of two chambers I, II of the same height, h , but different width, b . Furthermore, Chamber I introduced a step change in the rotor contour line. The disk face was shown to have a strong impact on the local heat transfer inside Chamber I, because it acts as a rotary atomizer and pumps oil radial outward. Droplets impinging at the stationary wall opposite to the disk cause a strong increase of local heat transfer coefficients. In contrast, Configuration 2 deals with strongly rectangular cross-sectional bearing chamber shapes and, in addition, both chambers have a different height.

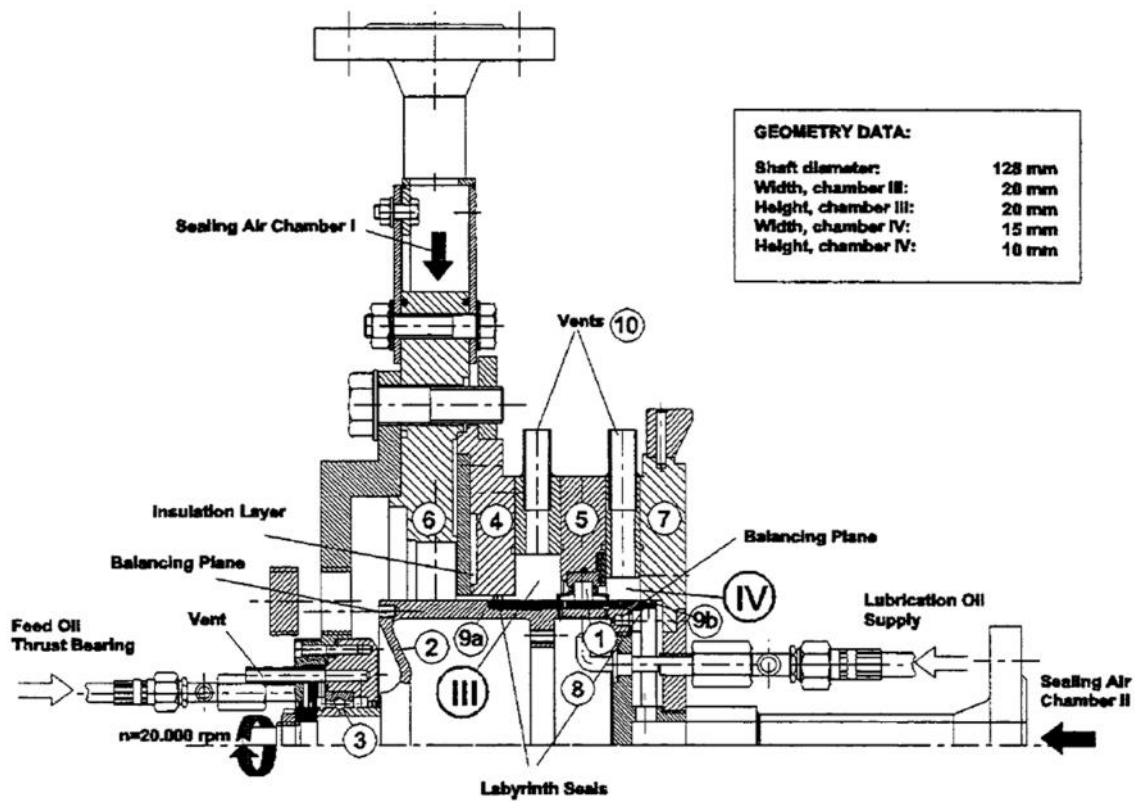


Figure 1.40. High speed bearing chamber test rig: 1 – squeeze-film-damped roller bearing; 2 – rotor; 3 – ball bearing; 4 – housing; 5 – roller bearing support; 6 – flange; 7 – chamber cover; 8 – under-race lubrication; 9 (a,b) – three-fin labyrinth seals; 10 – vent

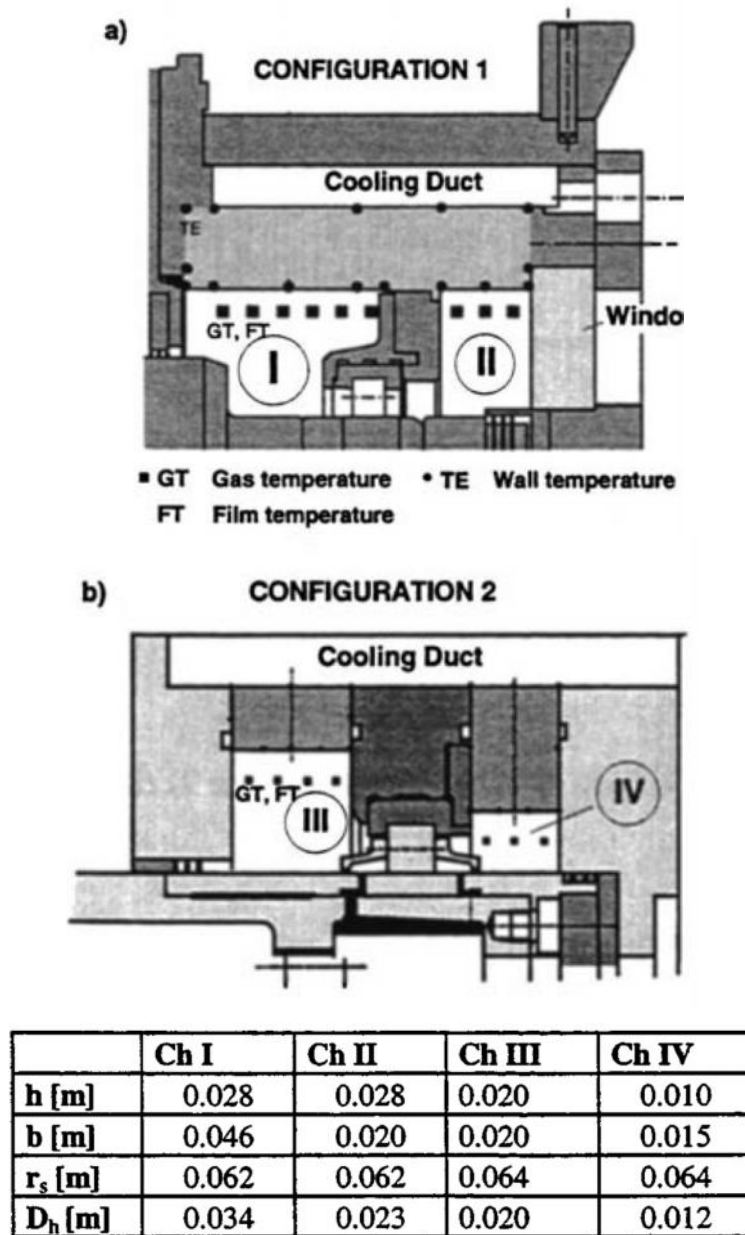


Figure 1.41. Difference between initial designed test rig and modified one
Heat-transfer in bearing chamber is provided used the thermocouples installed according to the scheme shown at Fig. 1.42.

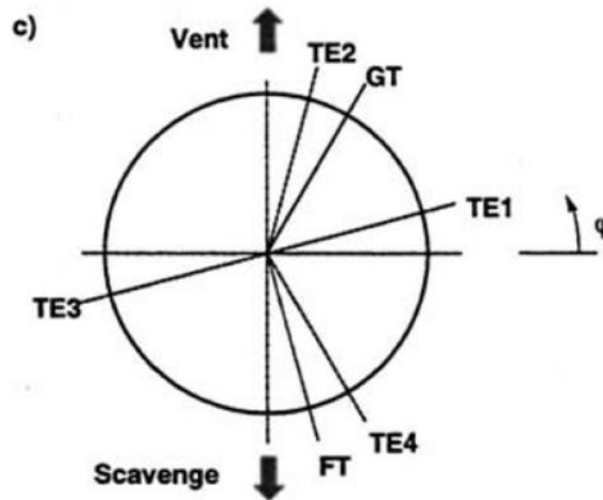


Figure 1.42. Thermocouple installation scheme

As a result of heat transfer investigation the generalized empirical formula for the internal bearing chamber heat transfer was received:

$$Nu_{D_h} = 0.35 \cdot D_h^{1.46} Re_L^{0.48} Re_F^{0.32} Re_U^{0.35}$$

where Nu_{D_h} – Nusselt number; D_h – hydraulic diameter; Re_L , Re_F – air and oil flow Reynolds numbers, respectively; Re_U – circumferential Reynolds number.

The current paper describes heat transfer measurements inside an experimental bearing chamber rig, designed for “not-end” rear bearing chambers sealed by means of labyrinths. The influence of operation condition factors on heat transfer coefficient was investigated: lubrication oil flow, sealing airflow, rotational speed. The successful outcome of this investigation is reflected by the introduction of a generalized correlation for the mean heat transfer coefficient at the internal bearing chamber housing wall.

Paper [21] suggests the newly designed test rig to measure the temperature in bearing chamber and calculating the heat transfer coefficient between oil film and wall. It is shown at Fig. 1.43. Basic structure of test chamber is presented at Fig. 1.44.

Experimental equipment includes a power system, an oil system, an air system and a data measurement system. Power system supplies power for this experiment. The rotation speed is a value range from 0 to 30000 rpm. Oil system supplied oil for the chamber, and the temperature of oil is a value between room temperature and 150°C. Flow amount value is range from 0 to 10 L/min. This oil can be scavenged using a pump with the ability to return to 25 L/min. Air system can warm outer wall of the cavity and supplied air for inner cavity. This air system can simulate a work condition of warm air in bearing chamber and pumped air into the bearing chamber. The temperature of air can be the max value 300°C, and the flow of air supply can be a value between 1 g/s and 6.5 g/s.

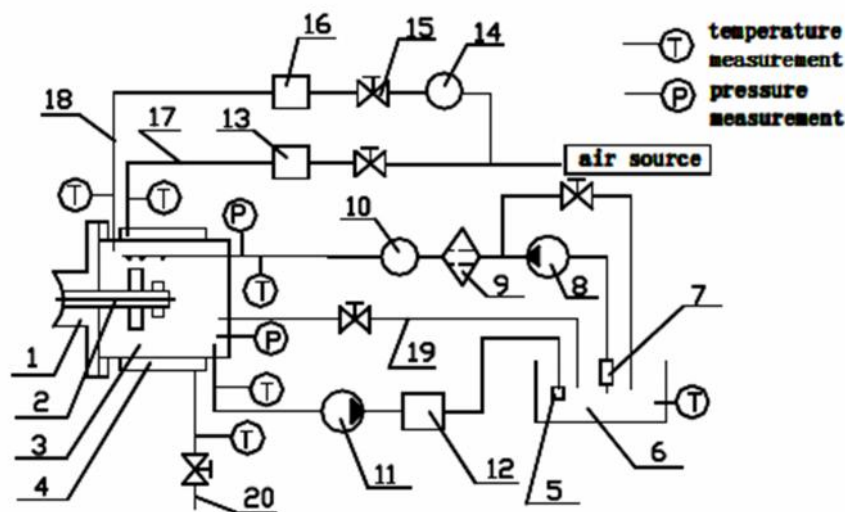


Figure 1.43. Principal scheme of test system:

1 – rotor assembly; 2 – rotor; 3 – inner chamber; 4 – heat chamber; 5 – oil/air separator; 6 – oil reservoir; 7 – coarse filter; 8 – oil supply pump; 9 – superfine filter; 10 – oil flow meter; 11 – scavenger pump; 12 – cooler; 13 – air heater; 14 – air flow meter; 15 – valve; 16 – air heater; 17 – heat air supply line; 18 – simulative sealing air supply line; 19 – vent line; 20 – heat air outlet line

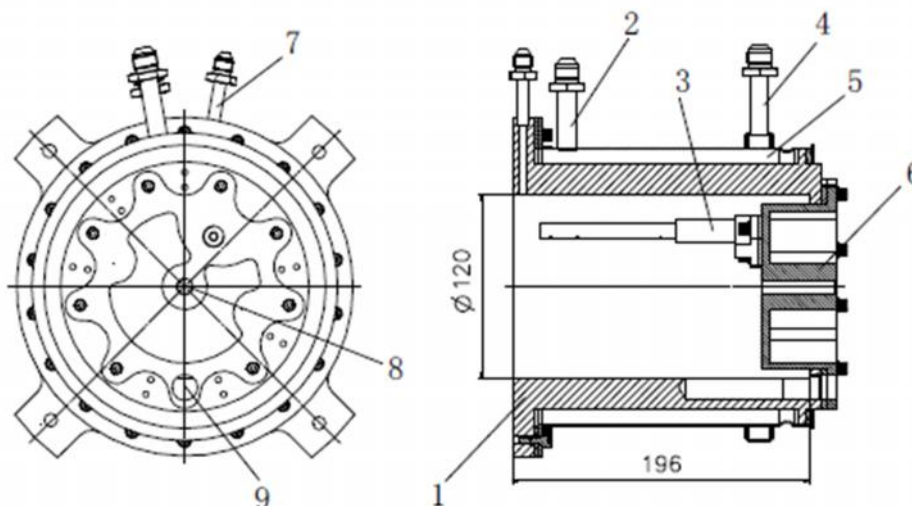


Figure 1.44. Basic structure of test chamber:

1 – housing of chamber; 2 – heat air inlet; 3 – oil nozzle; 4 – heat air outlet; 5 – heat chamber; 6 – cover; 7 – simulative sealing air inlet; 8 – simulative sealing air outlet; 9 – scavenge

Data measurement system was used to obtain several working parameters, including rotation speed, temperature in bearing chamber, oil working parameters and the temperature of wall. Oil working parameters include pressure, temperature and flow.

This experiment includes two tests:

1. Heat transfer test and air is not pumped. The air temperature in cavity is (300 ± 5) °C. The wall temperature of cavity, temperature in the cavity and scavenge oil were measured when temperature of supplied oil, supplied oil flow and rotation speed were changed.

2. Heat transfer test and air is pumped into the bearing chamber. The air temperature in cavity is (300 ± 5) °C. The wall temperature of cavity, temperature in the cavity and scavenge oil were measured when pumped air flow, temperature of supplied oil, supplied oil flow and rotation speed were changed.

This experiment aimed to the heat transfer in the outer face of bearing chamber, and a selection criterion was developed which is used to determine heat transfer coefficient between oil and chamber wall in a bearing chamber heat analysis. Heat transfer coefficient in different heat transfer type also needs to be investigated. For example, the heat transfer coefficient between air and outer cavity wall, oil and inner cavity wall, oil and bearing, oil and shaft. It should be noted that the researched chamber does not include the bearing: authors used two circles instead of bearings.

The paper [22] discusses measuring, modeling and calculating the heat transfer coefficients. The bearing chamber heat exchange experiment part adopts the common material of the aviation engine bearing chamber, namely 1Cr18Ni9Ti. According to the working state of an engine bearing chamber, were accomplished the design and process of the experiment. The assembly drawing is shown in Fig. 1.45.

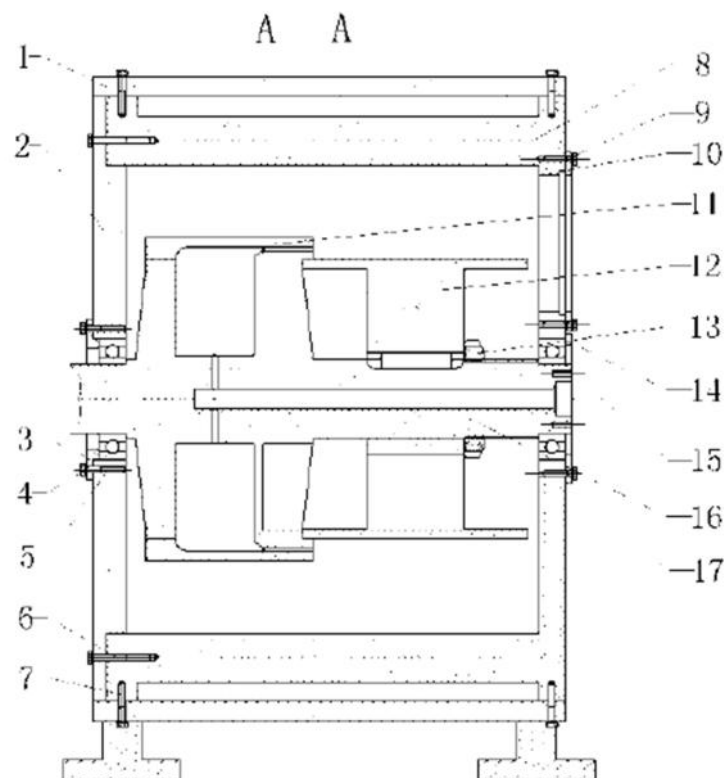


Figure 1.45. Assembly model of experiment:

1 – heating chamber shell; 2 – bearing cavity end cap; 3 – bearing retainer; 4 – ball bearing; 5,6,7,9 – screw; 8 – bearing cavity wall; 10 – observation window end cap; 11 – oil swing

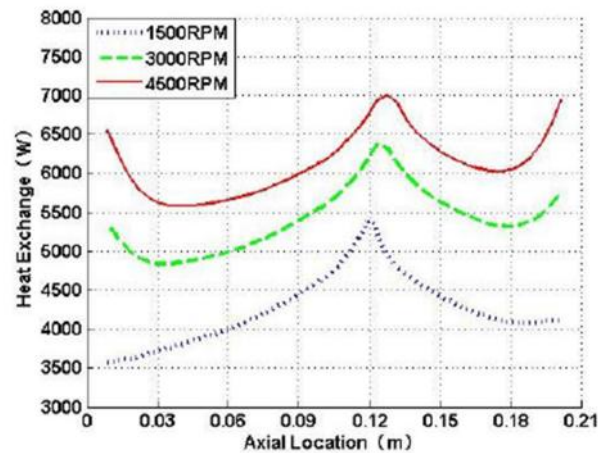
structure; 12 – rotating disk; 13 – positioning end cap; 14 – bearing retainer; 15 – ball bearing; 16 – axis of rotation; 17 – pin

The lubricating oil is sprayed into the bearing chamber by the right end of the bearing (15), and the oil is made into small particles and thrown into the bearing chamber through the swing oil structure (11) and the rotating disk (12). Then the air-oil two-phase flow field is formed. One part of oil is formed on the inner wall of the bearing chamber (8), and the other part of the lubricating oil flows out of the oil return hole. And the heating chamber is formed by the heating chamber shell and the wall surface of the bearing chamber. Then the air heated to a certain temperature through the pipeline goes into the heating chamber to heat the bearing chamber wall (8), and finally discharged from the exhaust pipe.

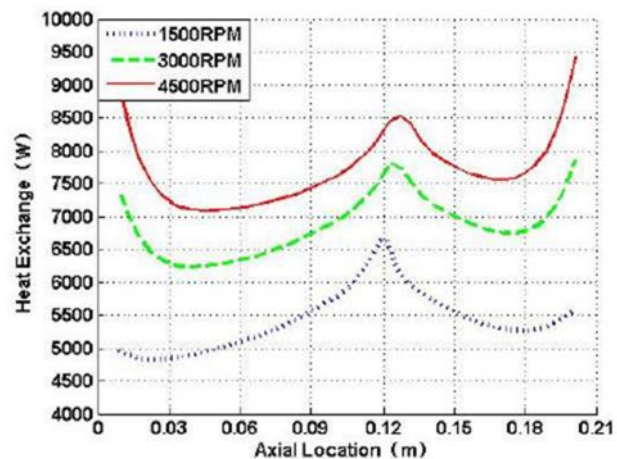
The temperature measuring points are arranged in the bearing chamber including its outer and inner walls.

The experiment on the heat transfer of the bearing chamber is carried out based on the actual working condition of aero-engine. Then the experimental results are compared with the CFD results to verify the accuracy of the two-phase flow simulation model.

The trend of the simulation results of the wall heat transfer (Fig. 1.46) is in good agreement with that of the experimental results, but the value is generally higher.



a) The oil flow rate 200L/h



b) The oil flow rate 400L/h

Figure 1.46. Heat transfer under different speed

It was shown that convective heat transfer coefficient increases with the increase of the shaft speed under the same fuel supply flow rate. The main reasons are as follows. Firstly, the increasing rotation speed generates larger shear force of the air near the surface of the inner wall, causes more complex oil flow field near the wall. Thus the flow condition is more beneficial to the conductive heat transfer. Secondly, the oil is distributed more uniformly on the inner wall surface under high rotation speed, thus increases the heat transfer within the wall surfaces. In contrast, a large amount of lubricating oil is accumulated in the oil return hole under low rotation speed.

It should be noted that the observed rotation speed – 4500 rpm – is very low for typical aircraft engines rotors. Additionally the modeling diagram shown on Fig. 48 is verified by the experiment only in the middle part of the diagram: left and right parts of modeled curve are not verified experimentally.

1.6 Experimental optimization of sump design.

Paper [9] deals with the test rig (Fig. 1.1) with modifications to estimate the influences of vent offtake and scavenge offtake on the operability of bearing chamber. Some modifications were made to the initial test rig to understand the influence of offtakes to the observed processes, same with the [10]: - the vent offtake can be mounded as it was shown in Fig. 1.12; - design of scavenge offtake can be changed (Fig. 1.47); - labyrinth seals can be installed with the eccentricity.

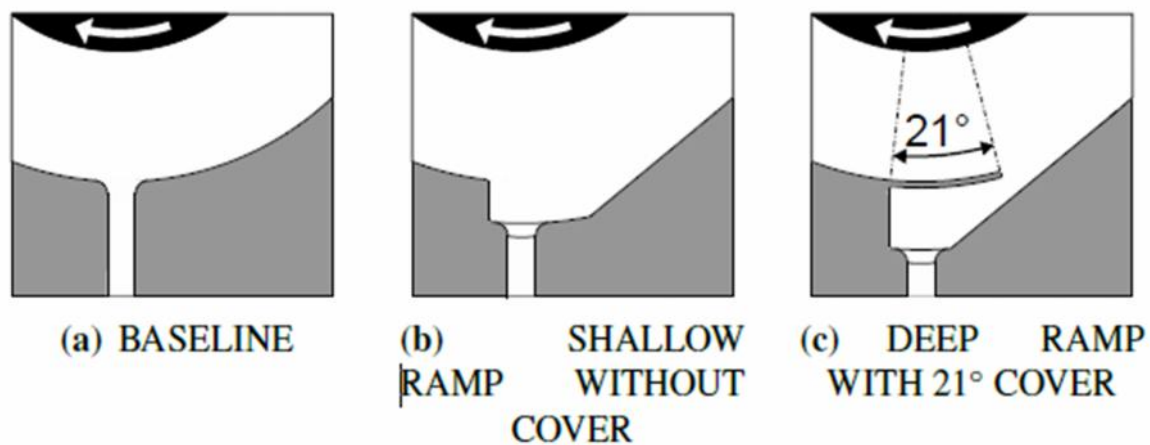


Figure 1.47. Schematics of the scavenge offtakes

As the highest changes of scavenge efficiency occurred at 15,000 rpm, the influences of the different scavenge offtake features are discussed at this shaft speed. All changings in design of test rig are estimated using the scavenge efficiency calculated by the next formula of volume flow rates:

$$y_{sc} = \frac{\dot{V}_{l,sc}}{\dot{V}_{l,in}} = \frac{\dot{V}_{l,sc}}{\dot{V}_{l,sc} + \dot{V}_{l,\epsilon t}}$$

where “l” means oil, “in” – inflow, “vt” – vent.

Scavenge efficiency was directly calculated with the measured oil flows in the vent and scavenge pipe using the measures volume flow rates.

Systematic variation of a ramp scavenge offtake yielded that a covered ramp design increased the scavenge efficiency the most. With this design, the scavenge efficiency at 15,000 rpm was at a constantly high level of $77\% < \eta_{sc} < 97\%$ compared to a wide range of $21\% < \eta_{sc} < 56\%$ for the baseline configuration at the same operating conditions.

A protruding vent was found as another measure to increase the scavenge efficiency significantly. Furthermore, a comparison of the baseline, the covered ramp scavenges and the protruding vent configuration showed a significant impact of each of the designs on the angular oil film thickness distribution. The covered ramp offtake proved to be the most efficient way to remove oil from the chamber.

The nominal labyrinth seal clearance in the test rig was $h_{seal} = 0.7$ mm. In order to ensure a uniform inflow of sealing air, the front cover plate was carefully assembled by measuring and

setting the position with respect to the rotor outer surface. Tests showed that a nonuniform seal clearance can result in either an increase or a decrease of the oil in the vent flow depending on the angular position of the maximum clearance height.

The principle of the applied film thickness measurement technique is described in [8]. As the oil has a higher relative permittivity than air the capacitance above the sensor changes with the height of the oil film. In order to prevent any disturbance of the oil film by the sensor, each sensor was equipped with a small polycarbonate platelet which was polished after the assembly of the sensor to fit the surface of the housing. Oil film thickness measurements were taken with every operating point. As the protruding vent and the covered ramp were identified to have the highest impact on the oil split, these designs were compared to the baseline configuration in terms of the oil film distribution. Some conclusions about film thickness in the observed scavenge design variants were made.

Provided experiment has showed the great influence of offtake design to the lubricant efficiency. But the obtained values can be estimated only quantitative because for the other design of test rig and operation conditions results can be significantly differ. Further investigations are necessary to identify the impact of other offtake designs and of other elements in a bearing chamber, such as oil jet blocks. Most important, however, is to extend the tests to different rotor diameters and different bearing chamber dimensions in order to render the results transferable to real engine applications.

Researching the real bearing chamber (sump) of Rolls-Royce AE3007 using the designed test rig are presented in [23]. The newly designed bearing chamber presented at Fig. 1.48.

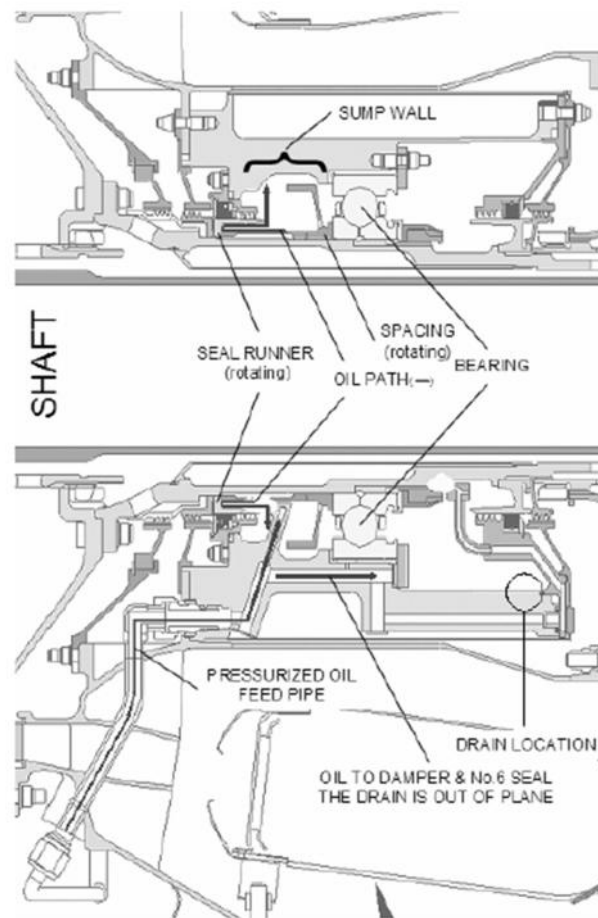


Figure 1.48. Center sump of Rolls-Royce AE3007 engine

The original design of Rolls-Royce AE3007 central sump is a tangential sump. An experimental program was conducted to investigate the characteristics of a tangential sump design. The research employed a bespoke experimental rig consisting of modular transparent chamber to allow unprecedented view of the two-phase flow inside the bearing chamber.

In this particular bearing chamber arrangement, the oil is injected towards a seal runner. Upon impact with the seal runner, the oil is atomized and picked up by the bulk rotating air flow in the bearing chamber. The atomized oil that leaves the seal runner, depending on the shaft speed, can vary in size and velocity. It can also be a mix of ligaments and airborne droplets. These oil ligaments and droplets, once entered the sump, are immediately trapped in the bulk rotating air flow induced by the highly rotating shaft. Eventually, the airborne oil mass reaches the wall of the sump and creates a highly turbulent film. The oil film on the sump wall is still highly driven by the shaft windage. It is important to note that at this stage, the oil film also has to perform its secondary objective, which is to pick up the heat from the sump wall, thus it further increases the oil temperature. The hot oil in the sump needs to be removed before the temperature climbs to beyond a safe working limit. Overheated oil can cause oil property degradation leading to coking.

Based on the lesson learnt from the study, an advanced sump design was proposed as shown in Fig. 1.49.

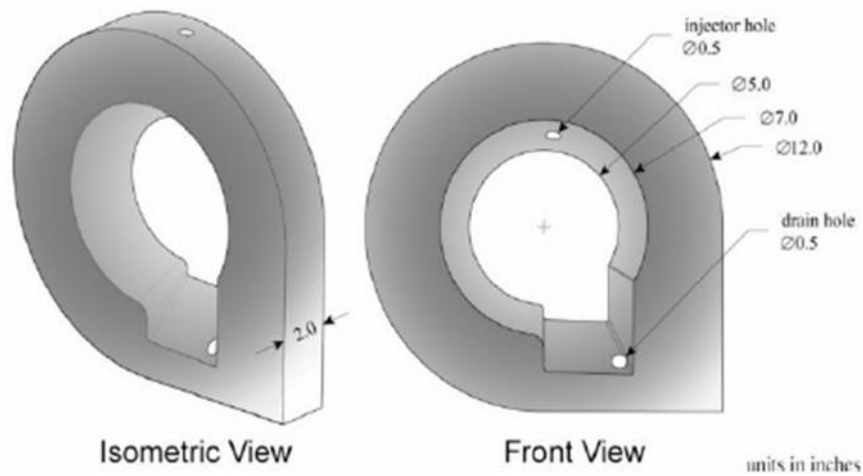


Figure 1.49. Advanced sump design (counter clock-wise shaft rotation)

An acrylic model of the advanced sump was manufactured to allow for unobstructed visual access. A closed-loop oil flow circuit is used to simulate the oil recirculation in the engine. It consists of the sump itself, a scavenge pump, a reservoir, a filter, a main centrifugal pump to inject the oil back, and rotameters. Scavenge ratio is defined as the ratio of the scavenge pump volumetric flow rate to the injected oil flow rate. The scavenge pump volumetric flow rate is obtained through calibration with liquid phase only. The scavenge pump is a constant displacement pump that is powered by a variable speed motor. The sump, including the drain region, consists of a center plate and two end-plates as shown in Fig. 1.50. The shaft can rotate up to 15000 rpm.

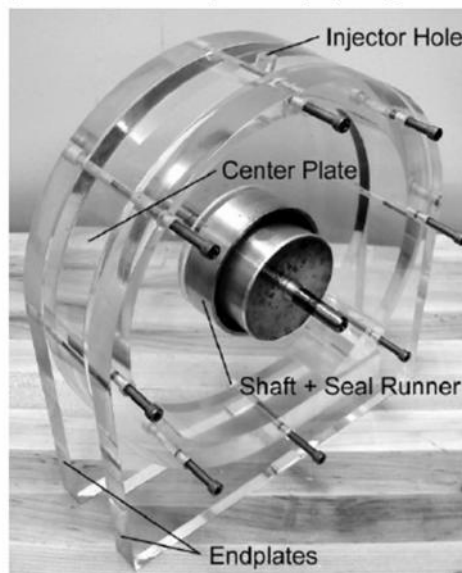
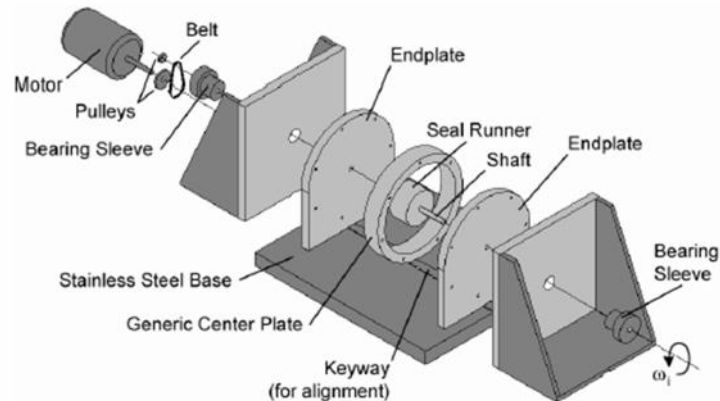


Figure 1.50. Scheme and view of test rig

Using this test rig the different change of design were provided:

- geometry and location of fence;
- geometry and location of splitter plate;
- size and location of drain hole;
- tilting effect;
- faired sub-sump;
- sump depth.

A CFD study was conducted on some faired sub-sump geometries in FLUENT (2-D air only calculation) to determine the best 2-D design. The criteria of a good sump are the one with recirculation cells that allow most of the air just above the fairing to move down toward the drain.

The efficiency of all experiments are estimated using the directly view (paper includes photo of experiments) and the residence volume of the advanced sump. Designed test rig fully

corresponds to the original aircraft engine so it is a problem to use it for the other object, but the given approach is rather good. There is lacks of sensors: temperature, film thickness, oil velocity and some others needed parameters are not measured. And it should be noted that the experiment is provided only in cold state.

1.7 Experimental investigation of leakages through the labyrinth seals.

Paper [24] deals with the experimental results identifying the influence of chamber geometry on the oil leakage (through seals) behavior of an aero engine bearing chamber. In order to assess the influence of the bearing chamber geometry on the leakage behavior, a labyrinth seal test rig was modified. It is shown in Fig. 1.51 and Fig. 1.52. The test section, highlighted by the dashed line, consists of the exchangeable rotor with five labyrinth seal fins and the stationary casing with the modular stator mount. With a modular stator mount, different designs of a so-called drip lip can be investigated.

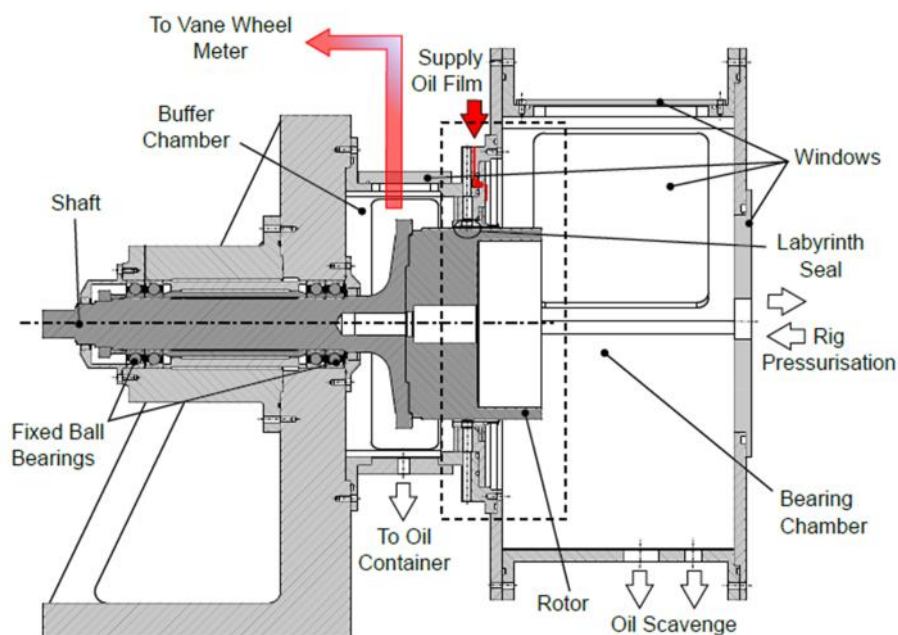


Figure 1.51. Cross section of labyrinth seal test rig with features

The aim of this feature is to guide oil flowing down the bearing chamber wall away from the rotor-stator gap. Similarly, different rotor geometries can be tested by varying the gap width between the drip lip and a so-called flinger or using a rotor without a flinger. The flinger also serves as a means of guiding oil away from the labyrinth seal gap, in this case coming from the shaft. The labyrinth seal divides the test rig into the bearing chamber compartment on the right and the buffer chamber on the left. The wall film generator, consisting of 188 narrowly spaced holes above the seal gap area, was used throughout the experiments.

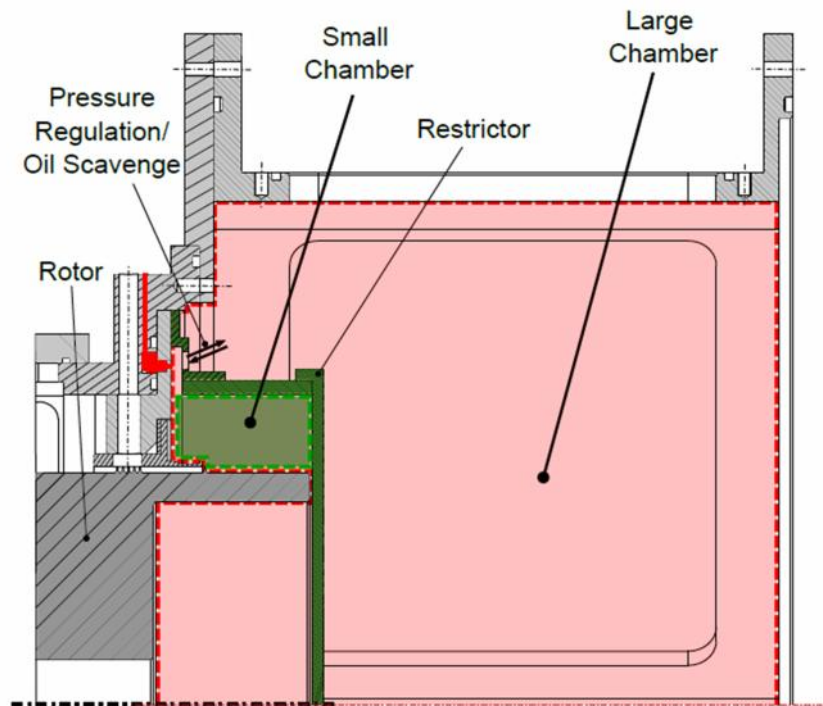


Figure 1.52. Detailed cross section of bearing chamber and restrictor

The variable parameters of the investigation are rotational speed, seal configuration (flinger, drip lip) and bearing chamber size:

- the rotational speed of the rotor was varied between 4000 and 10000 rpm at increments of 1000 rpm;
- the drip lip configuration was changed by manufacturing different stators which are shown in Fig. 1.53;
- the flinger configuration was changed by exchanging the rotor, with one rotor featuring a flinger and the other a smooth surface;

The air mass flow through the labyrinth seal air was varied from 1g/s to 2g/s. Positive values of \dot{m} air can be interpreted as air flowing into the bearing chamber. When an oil leakage rate \dot{m} oil of around 4g/s was reached, the air flow rate was not increased further to keep the leakage container from overflowing.

The air flow was controlled using two cone valves to be able to set up both negative and positive mass flow. The mass of the leaked oil was detected by capturing all leaked oil at the bottom of the buffer chamber which is connected to a container mounted on a scale.

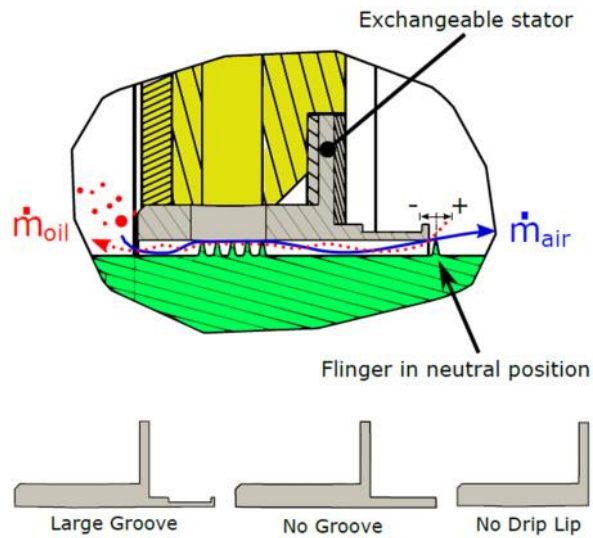


Figure 1.53. Seal area in test rig and stator configurations implementing different drip lip designs

The results of experiment had shown that oil leakage could not be observed for any of the tested operating points at positive mass flow rates. In other words air flow into the bearing chamber always prevented leakage. When the air mass flow was negative, the oil leakage behavior strongly depended on chamber size and other geometrical parameters such as presented on Fig. 1.54 and 1.55.

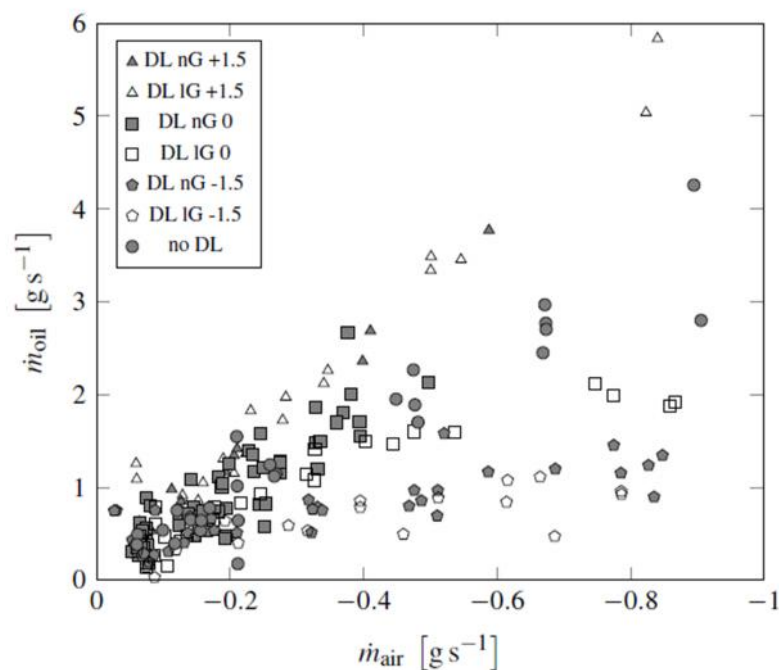


Figure 1.54. Oil leakage characteristic for various drip lip and flinger configurations at 10,000 rpm

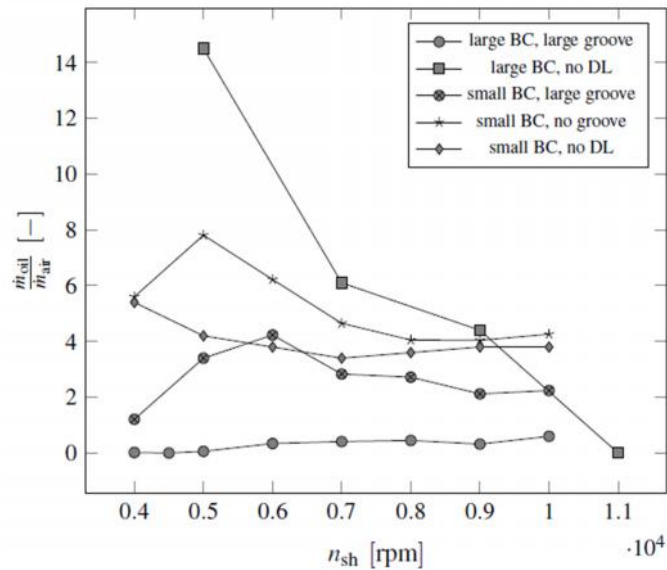


Figure 1.55. Oil leakage gradients for various configurations – neutral flinger position

The size of the bearing chamber has a strong influence on the oil leakage rate. There are multiple interdependencies between the varied parameters. Using a drip lip to reduce oil leakage under adverse conditions can be effective, especially for lower speeds. A flinger position too far away from the drip lip that might occur from relative movement of the shaft can nullify the advantage of a drip lip, however. When the flinger is located under the drip lip the system unexpectedly exhibits a very favourable leakage behavior, significantly reducing leakage for the entire rotational speed range.

Additionally the investigated labyrinth seal is representative for an engine seal under ideal design conditions and some factors are missed: shaft misalignment, thermal distortion of parts and seal wear. So the additional researches should be provided.

1.8. A review of wet gas flow rate measurements by means of singlephase meters

Paper [25] deals with the description of the possible effects of liquid presence in a wet gas and, an in-depth analysis of the limitations and beneficial effects of current single-phase flow rate sensors. Depending on the actual flow rate of the gas and the liquid, and their density, it is possible to establish how the mixture is wet, by means of the Lockhart-Martinelli parameter:

$$X_{LM} = \frac{\dot{m}_l}{\dot{m}_g} \sqrt{\frac{\rho_g}{\rho_l}}$$

where \dot{m}_g – mass flow rate of gas phase; \dot{m}_l – mass flow rate of liquid phase; ρ_g – density of gas phase; ρ_l – density of liquid phase.

A crucial aspect when measuring wet gas flows is the distribution of the liquid and gas component within a pipe, as this dispersion can affect the accuracy of the measuring device. This distribution is usually called “flow patterns” or “flow pattern models”. The various types

(Horizontal and vertical up) of flow patterns are studied. Additionally the list of 22 flow pattern maps for horizontal two-phase flow systems was presented.

This paper [25] lists the main single-phase meters currently used in oil and gas industry, emphasizing their limitations when metering a wet gas flow (or in general a two-phase flow). Both non-differential pressure meters (NDPMs) and differential pressure meters (DPMs) are discussed based on results and consideration of previous investigations found in the literature:

1. Turbines meters.

The operation and design of TMs were proven not to be suitable for measuring wet gas flows, although very little literature is available. This is due to:

- 1) damage from impacts between the liquid components and the turbine blades,
- 2) the potential wear of the bearings caused by the presence of particulate or impure fluids.

Moreover, wet gas flow measurements cause low repeatability of the results, definitely due to the liquid phase and type of flow pattern. The main studies, which were carried out by some researches with low liquid content, confirmed that these types of device should not be used in wet gas processes. But additional studies and tests on these types of sensors are required to better establish if they can be reliable wet gas meters.

2. Coriolis Meters (CM).

Although CMs have outstanding features when measuring liquids, and satisfactory characteristics when measuring gas flows, the results showed their low repeatability and high errors when measuring wet gas flows, even with a low liquid phase content. Other research verified that, at high pressure values (30 barg and 60 barg) the meter exhibited significant errors, with the tendency to measure:

- 1) a gas flow rate lower than the actual one, at low LVF and low gas flow rate;
- 2) a higher gas flow rate at high LVF and high gas flow rate.

Is it also claimed that that the measured density was significantly lower than the reference density in dry gas, and this variance increased as the liquid content increased.

Currently, the interest of research in CMs is becoming more popular in order to deal with issues surrounding the application of these devices for wet gas flow measurement and increasing their reliability and repeatability.

3. Ultrasonic Meters (USMs).

It is clear that the literature data do not suggest the use of USMs as wet gas meters, since their behavior seems to be strongly affected by the flow pattern - in real processes, it is difficult to ensure the generation of one specific flow pattern rather than another. No USM manufacturer has yet created any wet gas correlation, for this type of sensors.

4. Vortex Meters (VMs).

On the basis of the works presented in this sub section, the current status of research highlights that these meters may have promising results but need to be better investigated in order to make them reliable wet gas meters (through measure data corrections).

5. Differential pressure meters (DPM).

Usually, for wet gas flow metering, VTs are preferred, not because of greater accuracy, but thanks to their lower wear at high differential pressures, compared to orifice plates. In fact, OPs have to be frequently inspected to check if there has been any erosion, due to the liquid particle impact (if the sharp edge of the orifice is worn, the accuracy of the device strongly decreases). On the other hand, this drawback of OPs can be overcome by specific design expedients (ISO 5167-2); in fact, they are often used due to their easy installation and lower cost.

The paper [25] gives the rather full review of methods of wet gas metering. But the presented results of some researches give the conflicting information. So the additional investigations of these methods have to be provided.

2. Mathematical models of the multiphase flow in the bearing chamber

The prediction of flow distribution and heat transfer phenomena in a bearing chamber is an important objective in the design of GTE lubrication system. An adequate solution of this task can improve not only the efficiency of the lubrication system, but also the gas turbine engine as a whole. The need to improve the approaches to determine the behavior of two-phase flows in the parts of GTE lubrication system was noted by Zimmermann et al. [26]. Subsequently, this has become a topic for many studies.

2.1 A simplified models of the oil film on the housing of a bearing chamber

A simplified model of the oil film on the housing of a bearing chamber is presented in [27]. An integral approach is used and the analysis includes the effects of surface friction, heat transfer, gravity and swirl of the oil at inlet. Two-dimensionality is assumed with variations in the axial direction being neglected. The model is expected to apply at high rotational speeds where "rimming" dominates with the oil flowing around the drum in a continuous film. A similar rimming flow regime occurs in a rotating, horizontal drum partially filled with liquid and the present model was also tested against data for this problem.

No account is taken of drag at the free surface of the film or surface tension. Rough estimates of the air drag at the free surface of the film were made and suggest this is considerably smaller than the surface drag. However, formation of surface waves may lead to increased interaction and affect film break down. Modelling of the film-air interface is necessary and treating this as an average shear stress.

A thin control volume extending radially across the film is considered. For a thin film, boundary layer assumptions apply and the variation of pressure across the film is small. Since the pressure at the free surface must equal the ambient pressure, circumferential pressure gradients can therefore be neglected. Mass and angular momentum balances for the control volume then give the following differential equations.

$$\frac{m}{2f} = \frac{dm_f}{d\theta}, \quad (2.1)$$

$$\frac{m\epsilon_m}{2f} = \frac{dJ}{d\theta} + \dots gR \sin \theta + \frac{f \dots R}{2} (\epsilon - \epsilon_s) |\epsilon - \epsilon_s|, \quad (2.2)$$

Here m is the source mass flow rate per unit axial length, ϵ_m is the tangential velocity of the source flow, R is the drum radius, θ is the angular co-ordinate (with $\theta = 0$ giving the bottom of the drum), U is the film thickness, \dots is the liquid density, g is gravitational acceleration, ϵ is the tangential velocity of the film at the free surface, ϵ_s is the drum speed, and f is a friction factor (such that shear stress $\dagger = 0.5 \dots (\epsilon - \epsilon_s) |\epsilon - \epsilon_s| f$, m_f and J are fluxes (per unit axial length) of mass and momentum in the film, defined by

$$m_f = \int_{R-u}^R \dots \epsilon dr, \quad (2.3)$$

$$J = \int_{R-u}^R \dots \epsilon^2 dr, \quad (2.4)$$

where r is the radial co-ordinate. It may be seen from eqn. (2.2) that the angular momentum balance is expressed as a balance of fluxes, gravitational effects and drag on the drum. To proceed further it is necessary to make assumptions regarding surface shear stress and velocity profiles across the layer, so that the friction factor and the integrals in eqns. (2.3) and (2.4) can be evaluated.

For laminar flow it is assumed from analogy with flow between parallel plates that

$$f = \frac{4}{Re} \quad (2.5)$$

$$(\bar{\epsilon} - \epsilon_s) / (\bar{\epsilon} - \epsilon_s) = y(2 - y) \quad (2.6)$$

where the Reynolds number and film co-ordinate y are defined by

$$Re = \dots u |\bar{\epsilon} - \epsilon_s| / \sim \quad (2.7)$$

$$\sim = (R - r) / u \quad (2.8)$$

and \sim denotes fluid viscosity. From eqns (2.3), (2.4) and (2.6) it may then be deduced that

$$m_f = \dots u (2\bar{\epsilon} + \epsilon_s) / 3 \quad (2.9)$$

$$J = \dots u (3\bar{\epsilon}_s^2 + 4\bar{\epsilon}_s \bar{\epsilon} + 8\bar{\epsilon}^2) / 15 \quad (2.10)$$

For turbulent flow it is assumed by analogy with flat plate flow that

$$f = 0.045 / Re^{0.25} \quad (2.11)$$

$$(\bar{\epsilon} - \epsilon_s) / (\bar{\epsilon} - \epsilon_s) = y^{1/7} \quad (2.12)$$

From eqns (2.3), (2.4) and (2.11) it may then be deduced that

$$m_f = \dots u (7\bar{\epsilon} + \epsilon_s) / 8 \quad (2.13)$$

$$J = \dots u (\bar{\epsilon}_s^2 + 7\bar{\epsilon}_s \bar{\epsilon} + 28\bar{\epsilon}^2) / 36 \quad (2.14)$$

To close the problem conditions at the exit (at $r = 0$) must be specified. Here the film mass flux m_f is specified and the ratio J/m_f is assumed to be continuous. Clearly a discontinuity in m_f equal to the source mass flow m , is required at this point. With these conditions the above equations define the problem for calculating the film flow. The mathematical problem thus reduces to solving two simultaneous ordinary differential equations.

In practice oil will exit through the vent pipe as well as through the scavenge port. Although not reported here, the model has been extended to include this. Results did not show a great

deal of sensitivity to the proportion of oil assumed to exit through the vent (in proportion to other uncertainties) and so attention here is concentrated on the simpler configuration.

In order to obtain estimates of heat transfer, an energy equation is derived. Neglecting frictional heating, and using a similar approach to that for the flow equations, an energy balance on the control volume gives the following differential equation

$$\frac{mT_{in}}{2f} = \frac{dI}{d_r} + \frac{Rq}{C} \quad (2.15)$$

where T_{in} is the temperature of the source fluid, q is heat flux from the film to the drum, C is specific heat and I (energy flux in film) is defined by

$$I = \int_{R-u}^R \dots \epsilon T dr, \quad (2.16)$$

Assumptions are then required regarding the surface heat flux and temperature profile across the film.

For laminar flow the following relations are employed, based on a solution for duct flow with constant surface heat flux.

$$\frac{(T - \bar{T})}{(T_s - \bar{T})} = (3 - 4y - 2y^2 + 4y^3 - y^4)/3 \quad (2.17)$$

$$q = 4k(\bar{T} - T_s)/3u \quad (2.18)$$

where \bar{T} is the temperature at the free surface, T_s is the drum surface temperature, and k is the fluid thermal conductivity. Integrating eqn. (16) with the appropriate substitutions then gives

$$I = \dots u(36\epsilon_s \bar{T} + 6\epsilon_s T_s + 16\epsilon \bar{T} + 5\epsilon T_s)/315 \quad (2.19)$$

For turbulent flow, bearing in mind the high Prandtl number of oil, a flat temperature profile is assumed in evaluating 1, and a correlation for forced convection inside tubes is adapted to get a relation for the heat flux. The following equations result.

$$q = 0.00976 k(\bar{T} - T_s) Re^{0.9} Pr^{0.3}/u \quad (2.20)$$

$$I = \bar{T} m_f \quad (2.21)$$

where $Pr = \sim C/k$ is the Prandtl number.

At the exit ($r = 0$) continuity of I/m_f is assumed. The above equations then define the mathematical problem for the estimation of heat transfer.

It was assumed that pressure variations across the film are negligible when considering the angular momentum balance. However, it is clear from the equation for conservation of radial momentum that centripetal and gravitational effects will give rise to pressure gradients across the film. Provided the film is very thin these gradients will only result in small pressure

differences, so the assumption in may be justified. Nevertheless the balance of forces across the film is important when considering whether the existence of a thin film is plausible. It is assumed here that if the pressure in the film falls below that at the free surface then the film will break up or separate from the surface. Physically, this condition corresponds to the rotation of the liquid being insufficient to overcome the gravitational pull, with the consequence that the liquid falls away from the surface.

To first order in small quantities the equation for conservation of radial momentum may be written.

$$\frac{dp}{dy} = -\rho g \cos \theta - \frac{u}{r} \rho \epsilon^2, \quad (2.22)$$

Integrating between non-dimensional boundary layer co-ordinate $y = 0$ and $y = 1$ gives

$$p_s - \bar{p} = \rho g \cos \theta + J/R, \quad (2.23)$$

where p_s and \bar{p} denote pressure at the drum surface and free surface, respectively.

For the assumed form of variation of ϵ across the film, it follows that the pressure in the film will fall below the free surface value if, and only if, either $p_s - \bar{p}$ is negative or dp/dy at $y = 1$ is positive. This criterion is used in estimating the onset of film break up.

A model has been presented for the "rimming" flow regime in a bearing chamber. In this regime the flow is dominated by a continuous oil film on the outer chamber wall. The model gives an indication of the likely occurrence of this regime and predicts heat transfer rates, film velocities and film thicknesses. Either laminar or turbulent flow can be specified in the model which is based on an integral method with assumed boundary layer profiles and relations for surface shear stress and heat flux. There are similarities between the bearing chamber flow and the flow of liquid in a partially filled, horizontal, rotating drum, and so published data for the rotating drum has been used for evaluation of the present model. It was found that for laminar flow conditions predictions of the minimum drum speed at which rimming can occur were in good agreement with experiment. Predictions for a lower viscosity liquid, for which the flow is likely to be turbulent, showed greater differences with measurements, possibly indicating some shortcomings of the model assumptions.

The paper [6] represents the further development of the theoretical model, discussed in [7]. It gives a theoretical outline on liquid film flows driven by superimposed effects of interfacial shear and gravity forces and discusses related heat transfer processes which are relevant for lubrication oil systems of aero engines.

Neglecting pressure forces and any acceleration of the fluid and based on the assumption, that the time averaged film height \bar{h}_F is small in comparison to the curvature of the housing wall ($\bar{h}_F / r_i \leq 0.02$), the velocity u_F of a fluid element at a distance y from the wall (see Fig. 2.1)

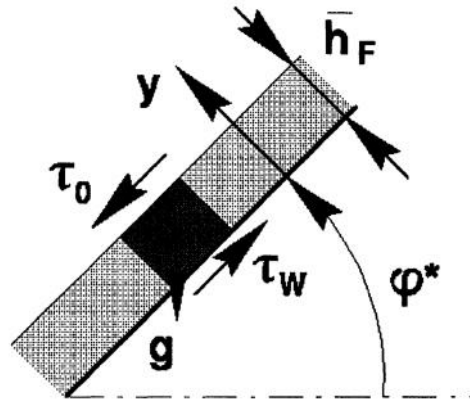


Figure 2.1. Force balance

can be obtained from the momentum equation

$$1 - \dagger y_F^+ = \left(1 + \frac{\epsilon_t}{\epsilon_F} \right) \frac{du_F^+}{dy_F^+}, \quad (2.24)$$

where \dagger – non-dimensional parameter for the film velocity profile; ϵ_t – eddy viscosity; ϵ_F – film kinematic viscosity

Film temperature T_F is given by the heat flux distribution across the film

$$\frac{\dot{q}}{\dot{q}_w} = \left(\frac{1}{Pr_F} + \frac{1}{Pr_t} \frac{\epsilon_t}{\epsilon_F} \right) \frac{dT_F^+}{dy_F^+}. \quad (2.25)$$

where \dot{q}_w – wall heat flux; Pr_F and Pr_t – film and turbulent Prandtl numbers, respectively.

Velocity, wall distance and temperature have been transferred to non-dimensional values by use of the shear velocity

$$u_{\dagger,F} = \sqrt{\dagger_w / \dots_F}. \quad (2.26)$$

where \dagger_w – shear stress near the wall; \dots_F – film density.

Thus, velocity and coordinate are

$$u_F^+ = \frac{u_F}{u_{\dagger,F}}, \quad (2.27)$$

$$y_F^+ = y \frac{u_{\dagger,F}}{\epsilon_F}, \quad (2.28)$$

and the dimensionless film temperature equals

$$T_F^+ = \frac{(T_W - T_F) \dots_F C_{P,F} u_{\dagger,F}}{\dot{q}_w}. \quad (2.29)$$

where T_w – wall temperature; $C_{p,F}$ – film heat capacity.

The parameter \dagger in Eq. (2.24) is given by

$$\dagger = \frac{\epsilon_F g \sin \{^*\}}{u_{\dagger,F}^3} \quad (2.30)$$

and expresses the superimposition of gravity and shear forces. Assuming zero interfacial shear ($\dagger = 0$), this parameter becomes $\dagger = 1/\bar{h}_F^+$ and Eq. (2.24) is equal to the approaches known from freely falling films. The other extreme case given by horizontal flow or extremely high interfacial shear is characterized by $\dagger = 0$, i.e. the shear stress is constant over the film height.

As it can be seen from Eqs. (2.24) and (2.25) a characterization of the momentum and heat transfer in bearing chamber oil film flows requires a proper matching of the eddy viscosity term ϵ_t/ϵ_F and, in addition, an expression for the turbulent Prandtl number Pr_t . Based on a comparison with measured data, typical representatives of existing models for the calculation of liquid film flows have been assessed for their potential on heat transfer predictions across bearing chamber oil film flows. It has been demonstrated that a simple analytical approach using an empirical correlation proposed by Deissler [28] for eddy viscosity

$$\begin{aligned} \epsilon_t/\epsilon_F &= n^2 u_F^+ y_F^+ \{1 - \exp(-n^2 u_F^+ y_F^+)\} \\ n &= 0.109 \end{aligned} \quad (2.31)$$

offers some scope for this task. It is shown that a simple analytical approach is able to predict measured heat transfer data fairly well. Typical deviations between measured data and predictions show values $|Ur|/Ur_M \approx 34\%$. As it has been expected due to the fact that the calculations have been performed without consideration of droplet bounded thermal energy transport from the bearing into the wall film, heat transfer coefficients obtained from theory show lower values than experimental data.

To permit a comparison of the different configurations of bearing chambers and to predict the film flow as a function of the circumferential location, two analytical models were used in [8].

The first model estimated the tangential velocity the pure air flow in the chamber using an angular momentum balance as given by Eq. (2.32), this approach is used to predict the averaged tangential velocity \bar{u}_g of the air flow, which is not affected by the oil flow. This velocity was used to estimate the impact of the air flow on the film for the different geometries.

$$M_r - M_s = \sum_{out} \dot{m}_{g,i} r_i (u_{g,t,i} - \bar{u}_g) - \sum_{in} \dot{m}_{g,i} r_i (u_{g,t,i} - \bar{u}_g) \quad (2.32)$$

where M_r and M_s – rotor and stator moment, respectively; $\dot{m}_{g,i}$ – gas (air) mass flow; r_i – radius; $u_{g,t,i}$ – gas turbulent velocity;

The rotor and stator moment are determined as follows:

$$M_r = \frac{\lambda}{8} \rho_g (\Omega r_{sh} - \bar{u}_g)^2 \int_{Rotor} r dA_r \quad (2.33)$$

$$M_s = \frac{\lambda}{8} \rho_g \bar{u}_g^2 \int_{Stator} r dA_r \quad (2.34)$$

where λ – friction factor; Ω – angular velocity of rotor; r_{sh} – shaft radius; ρ_g – gas (air) density; dA_r – surface.

Since this simplification is in contradiction to the real two phase flow in bearing chambers, this approach can only be used to estimate qualitatively the impact of the gas flow on the liquid wall film. A comparison with experimental data revealed that this approach predicts the pure air flow with a very good accuracy.

The second model, represented in [6], was used to characterize the shear and gravity driven wall film. A theoretical velocity profile is obtained from a nondimensional momentum equation (2.24), which is derived from a force balance of a turbulent liquid film at an inclined plane:

$$\frac{\tau}{\tau_w} = 1 - \tau y_F^+ = \left(1 + \frac{\epsilon_t}{\epsilon_F} \right) \frac{du_F^+}{dy_F^+}$$

The superimposed effect of gravitational and shear forces is taken into account by τ is defined by Eq. (2.30):

$$\tau = \frac{\epsilon_F g \sin \alpha^*}{u_{\tau,F}^3}$$

The accuracy of the model strongly depends on the definition of the turbulent eddy viscosity. For bearing chamber applications the approach of Deissler [28] was used.

To predict a velocity profile Eq. (8) must be integrated numerically. The wall shear stress τ_w has to be determined iteratively at the angular location α , where the velocity profile $u_F(y, \alpha)$ is known.

The local film Reynolds-number $Re_F(\alpha)$ and the film flow rate $\dot{V}_F(\alpha)$ are determined by Eqs. (2.35) and (2.24).

$$Re_F = \frac{\dot{V}_F}{b \epsilon_F} = \int_0^{h_F} u_F^+ dy_F^+ \quad (2.35)$$

where b – width of bearing chamber

With the known flow rate $\dot{V}_F(\alpha)$ and the assumption that the film flow rate increases linearly between the two ports, the flow $\dot{V}_F(\alpha)$ and the film Reynolds-numbers $Re_F(\alpha)$

can be determined for any angular position $\{\}$. Together with the assumption that the interfacial shear stress \ddagger_0 remains constant, the local film thickness $\bar{h}_F(\{\})$ and local wall shear stress $\ddagger_w(\{\})$ have to be determined iteratively.

Due to the assumptions the model is limited for the prediction of the film, but helped to derive an enhanced understanding of the complex film flow in bearing chambers. The results revealed that the operating conditions as well as the design of the chamber strongly impact the complex film flow. Furthermore, the liquid wall film was strongly affected by the design of the vent and scavenge ports, which strongly impact the discharge-characteristics of the oil-air mixture.

2.2 Mathematical model of thin film flow with droplet impingement

A dynamic mathematical model describing the thin film flow in aero-engine bearing chamber is presented in paper [4]. By analyzing the depth averaged continuity equation and momentum equation the comprehensive physical mechanisms driving thin film flow was revealed. Thin film model is based on presumed quadratic velocity profile.

If the oil film flow is treated as Newtonian, incompressible and isothermal with film velocity u_f and pressure p_f , then in general coordinates the flow is governed by continuity equation

$$\nabla \cdot u_f = 0 \quad (2.36)$$

and Navier-Stokes equations

$$\rho_f \frac{Du_f}{Dt} = -\nabla p_f + \rho_f g + \mu_f \nabla \cdot \nabla u_f \quad (2.37)$$

In Eqs. (2.36) and (2.37), ρ_f and μ_f are the oil density and viscosity respectively; g is the acceleration due to gravity.

In a typical bearing chamber configuration, the film flow is more readily described through reference to a curvilinear system of coordinates (s, y, x) , where (s, x) are the coordinates parallel to the chamber wall and y is the coordinate perpendicular to the chamber wall. Taking the film surface as $y = h(s, x, t)$, then local to the bearing chamber wall, a film flow configuration is illustrated in Fig. 2.2.

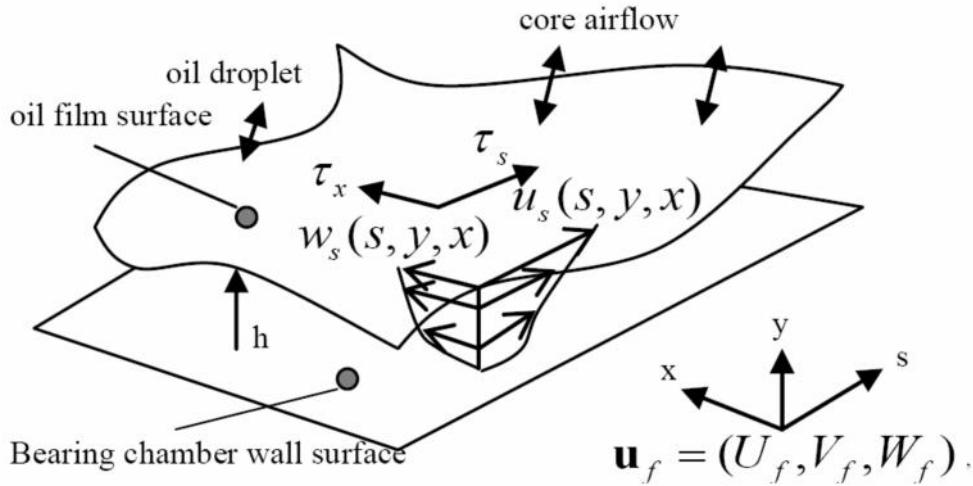


Figure 2.2. Schematic of localized oil film on the surface of the 3D bearing chamber

Since the film flow over the surface of the chamber tends to be thin, the depth averaged governing equations are used for flow analysis. The depth averaged integration is defined as

$$\bar{\xi}(s, x, t) = \frac{1}{h} \int_0^h \xi(s, y, x, t) dy$$

The typical thickness of film h is usually small compared with the radius of the chamber R , i.e. $v = h/R \ll 1$. For fluid flow this restricts the fluid acceleration across the film thickness and the flow is dominated locally by the chamber and the interface conditions. By using non-dimensional analysis, the order linked to v for each term in governing Eqs. (2.36) and (2.37) can be simplified. Keeping the terms with order up to $O(v)$ and applying depth averaging integration to continuity Eq. (2.36), the depth averaged continuity equation can be obtained as

$$\frac{\partial h}{\partial t} + \frac{\partial h \bar{U}_f}{\partial s} + \frac{\partial h \bar{W}_f}{\partial x} = V_f \Big|_{y=0} + \frac{\dot{m}}{\dots_f} \quad (2.38)$$

The term $V_f \Big|_{y=0}$ in Eq. (2.38) denotes the contribution of the oil flow at $y = 0$. Keeping the terms up to $O(v)$ and applying depth averaging integration to Eq. (2.37), a depth averaged momentum equation can be obtained as

$$C_{\zeta} = E_{\zeta} + G_{\zeta} + A_{\zeta} + W_{\zeta} + D_{\zeta} + V_{\zeta} + S_{\zeta} \quad (2.39)$$

in which, the subscript ζ denotes the coordinate direction (s or x in Fig. 2.2). Eq. (2.39) is the general depth averaged equation governing the momentum transport within film under

the thin film approximation. The physical mechanisms driving the transport of $h\bar{U}_f$ in the thin film flow can be categorized as

- *Convection of film,*

$$C_s = \frac{\partial h\bar{U}_f}{\partial t} + \frac{\partial h\bar{U}_f\bar{U}_f}{\partial s} + \frac{\partial h\bar{W}_f\bar{U}_f}{\partial x}$$

- *Variation of velocity profile within the film,*

$$E_s = -\frac{\partial}{\partial s} \int_0^h \hat{U}_f \hat{U}_f dy - \frac{\partial}{\partial x} \int_0^h \hat{W}_f \hat{U}_f dy$$

- *Gravity,*

$$G_s = h \left(\frac{g_y \partial h}{\partial s} + \frac{h}{2} \frac{\partial g_y}{\partial s} + g_s \right)$$

- *Air-film interaction (including pressure and shear stress),*

$$A_s = -h \frac{\partial p_a}{\dots_f \partial s} + \frac{\ddagger_a}{\dots_f}$$

- *Shear stress from wall,*

$$W_s = \frac{-\ddagger_w}{\dots_f}$$

- *Droplet-film interaction,*

$$D_s = -\frac{h \partial p_d}{\dots_f \partial s} + \frac{\ddagger_d}{\dots_f} + \frac{\dot{m} \bar{U}_f}{\dots_f} \Big|_{y=h}$$

- *Flow crossing the wall surface,*

$$V_s = V_f \Big|_{y=0} \bar{U}_f$$

- *Surface tension.*

$$S_s = \frac{h \partial \dagger k_l}{\dots_f \partial s} + \frac{\partial \dagger}{\dots_f \partial s}$$

Here U, V, W – film velocity components along s, y, x , respectively; $\bar{U}, \bar{V}, \bar{W}$ – depth averaged film velocity components along s, y, x , respectively; $\hat{U}, \hat{V}, \hat{W}$ – profile variation of film velocity components along s, y, x , respectively; \dagger – surface tension; p_a – air pressure; \dagger_a, \dagger_w – air and wall shear stress, respectively; \dot{m} – oil mass flux of droplet-film interaction.

The gravity term G_ζ , surface tension term S_ζ and flow extraction term V_ζ are evaluated to include the geometry of wall, surface tension properties and mass flow through the wall. Ideally, if the profile of film velocity is known, the term representing the variation of velocity profile E_ζ and the term representing the contribution of shear stress from wall W_ζ , as described above, can be evaluated. Unfortunately, the information of velocity profile is filtered by the process of depth averaging; a simple model is provided for the film velocity profile. The remaining information needed to solve Eqs. (2.38) and (2.39) are the interaction between air A_ζ and film as well as the interaction between droplet and film D_ζ . The interaction between air and film can be supplied from the computation of the core airflow directly. However, the interaction between droplets and film is complex and excessive computational resource would be needed to capture the details of droplet impingement, such as volume fraction and velocity. Usually, the droplet-film interaction is therefore simulated with recourse to a simplified model as part of thin film model framework.

The velocity profile is assumed quadratic for simplicity and, for example, the velocity component U_f may be approximated as $U_f = ay^2 + by + c$. Thus the wall shear term can be evaluated from the assumed velocity profile

$$W_s = \frac{-\dagger_w}{\dots_f} = \frac{\dagger_d}{2 \dots_f} + \frac{1 \dagger_a}{2 \dots_f} - \frac{3 \sim_f \bar{U}_f}{2 \dots_f h} \quad (2.40)$$

In Eq. (2.40), there is an extra contribution due to droplet impingement. For convenience, this term is rearranged and put into the droplet-film interaction; thus the model for the wall shear term is re-written as

$$W_s = \frac{-\dagger_w}{\dots_f} = \frac{1 \dagger_a}{2 \dots_f} - \frac{3 \sim_f \bar{U}_f}{2 \dots_f h} \quad (2.41)$$

For modelling the droplet term in Eq. (2.39), a schematic of droplet-film interaction process is shown in Fig. 2.3.

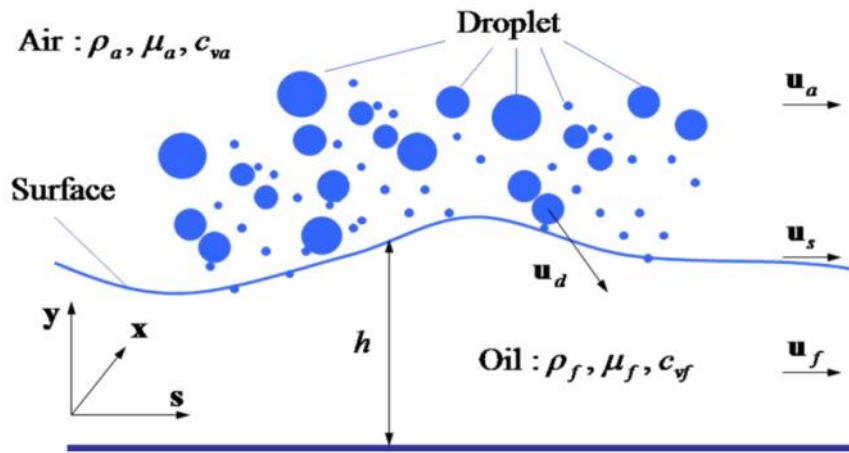


Figure 2.3. Schematic of droplets-film interaction

It is assumed that there are N droplets contacting a unit film area, each with velocity u_{di} , at one moment. Each droplet contacts film with area ratio Γ_i . A reasonable assumption is that the density of droplet is the film density \dots_f . When the considered area is reasonably small, the droplet velocity can be considered uniform locally. Also the normal component of film velocity is negligible according to the thin film assumption. Then a simplified droplet-film interaction model may be written as

$$D_s = \frac{h}{\dots_f} \frac{\partial \dot{m} U_{dn}}{\partial s} + \frac{3 U_{ds}}{2 \dots_f} \dot{m} - \frac{1 \bar{U}_f}{2 \dots_f} \dot{m} \quad (2.42)$$

Chew represented two thin film models for bearing chamber [27]: one for laminar film flow and one for turbulent film flow. According to previous work authors of [4] considered that, the thin film flow in an engine bearing chamber is observed as laminar film flow. In [6], the laminar velocity profile is assumed as $U_f / \bar{V} = y(2 - y)$, where $y = y/h$. Thus the wall shear term in Chew's model is

$$W_{s,Chew} = \frac{-\dagger_w}{\dots_f} = -\frac{3 \sim_f \bar{U}_f}{2 \dots_f h} \quad (2.43)$$

The droplet impingement is assumed at a uniform rate and so does not include the normal impingement velocity term

$$D_{s,Chew} = \frac{U_{ds}}{\dots_f} \dot{m} \quad (2.44)$$

The air-shear term $A_s = \dagger_a / \dots_f$ is to be added to Chew's model [27].

In Chew's paper, the variation of velocity profile, E_s , was not ignored and it will be in subsequent calculations, which implies that the depth averaged velocity is assumed to be dominant in the film transport. The surface tension term is ignored temporally in [4].

An air, oil droplet and film interaction model for a bearing chamber environment has been studied numerically. The numerical calculations of droplet-film interaction in a simplified bearing chamber model show that these models can capture the main features of the flows and work efficiently. By analyzing the thin film flow under weak convection, the relationship between the film mass flux and the air shear stress acting on the film was formulated. It was found that the value of shear stress taken as that at the wall between the wall and the air, ignoring the existence of a film, is not suitable to be used as the air shear stress on the film.

A thin film model developed in [4] for simulating the gas-oil two-phase flow in bearing chamber has been implemented in ANSYS Fluent. The performance of the model, which has been implemented in the commercial computational fluid dynamics software product: ANSYS Fluent, is benchmarked in [29] by comparing the computational results obtained from a Nottingham UTC in-house code and a development version of Fluent. Both codes were used to solve thin film flow in a test case configuration and based on the same finite area method. Applying this thin film model to predict the thin film flows in a simplified bearing chamber configuration, the thin film module in ANSYS Fluent is shown to be working well for higher values of air shear stress. For low values of air shear stress, unphysical discontinuities can appear in both codes, which require further examination by the team for this specific application.

An integrated model in combination with droplet movement, droplet/wall impact and film flow analysis initially based on the consideration of droplet size distribution is represented in [30]. The main approaches and equations of this model are shown below.

The oil droplets shed from bearing element are very small compared to the dimension of bearing chamber. Therefore the oil droplets moving in bearing chamber are primarily affected by air resistance, and droplets trajectories and velocities are changed at all time. In the cylindrical coordinates the kinematic equations of oil droplet in tangent, radial and axial direction deduced from theorem of momentum as follows:

$$\begin{cases} m_d \frac{du_{dt}}{dt} = \frac{1}{2} C_d A_{\dots q} |u_q - u_d| (u_{qt} - u_{dt}) \\ m_d \frac{du_{dr}}{dt} = \frac{1}{2} C_d A_{\dots q} |u_q - u_d| (u_{qr} - u_{dr}) \\ m_d \frac{du_{dz}}{dt} = \frac{1}{2} C_d A_{\dots q} |u_q - u_d| (u_{qz} - u_{dz}) \end{cases} \quad (2.45)$$

where m_d is mass of oil droplet; C_d is drag coefficient; A is windward area of droplet; \dots_q is density of air phase; u_q and u_d are velocity vector of air phase and oil droplet respectively; u_{qt} , u_{qr} and u_{qz} are tangent, radial and axial velocity of air phase respectively; u_{dt} , u_{dr} and u_{dz} are tangent, radial and axial velocity of oil droplet respectively.

Moving droplets will be resisted by different air resistant effects due to their diameter difference, and lead to the different velocities and momentum of oil droplets when the oil droplets impinge on the chamber wall. As a result, different impact statuses are also established which could be classified by the splashing parameter K [31].

$$K = We_d^{0.5} Re_d^{0.25} \quad (2.46)$$

Two impingement situations of oil droplets have been investigated, including the oil droplets depositing directly and the break-up oil droplets producing many secondary droplets. The mass of direct depositing droplets transfers to oil film, but only tangent momentum component of direct depositing droplets transfers to oil film because radial momentum component loses in the process of impingement. Deposited mass and tangent momentum component of break-up oil droplet transfer to oil film. The splashed part of break-up oil droplet forms some smaller secondary droplets in which some larger secondary droplets may be deposited again and other smaller ones are air-suspended and discharged from the vent port.

The velocity of secondary droplets is disordered when deposited, and no momentum of secondary droplets transfer to oil film, for their momentum neutralizes each other to zero. The film mass transferred from oil droplets is made up of the mass of direct deposited droplets, the deposited mass of break-up oil droplets and the subsequent deposited mass of secondary droplets. The film momentum is made up of the tangent momentum of direct deposited droplets and that of deposited part of break-up oil droplets.

The mass deposition efficiency of oil droplets y is defined as the ratio of the deposited mass of oil droplets to the mass of the oil droplets. For direct deposited droplets, $y = 1$. In the case that the oil droplets break up then come into secondary oil droplet case, y is expressed as

$$y = \begin{cases} 1 - 8.03 \times 10^{-11} K^{4.1718} + \frac{m_{sdc}}{m_d} & 57.7 < K \leq 200 \\ 0.1 + 5.792 e^{-1.15 \times 0.01K} + \frac{m_{sdc}}{m_d} & K > 200 \end{cases}, \quad (2.47)$$

where m_{sdc} – depositing mass of secondary oil droplets

The momentum transfer efficiency of oil droplets $\}$ is defined as the ratio of the momentum of oil film transferred from the deposited oil droplets to the momentum of oil droplets when shed from bearing. It is expressed as

$$\} = y_1 \frac{u_{dtz}}{u_{d0}} \quad (2.48)$$

where u_{dtz} is the tangent velocity of oil droplets when impacting on chamber wall, u_{d0} the initial velocity of oil droplets when shed from bearing, and y_1 mass deposition efficiency without secondary oil droplets.

The influence of droplet size distribution on deposited mass and momentum of oil droplets is identical to that of droplet mass distribution for spherical droplets. The mass distribution of oil droplets in bearing chamber can be expressed by Rosin-Rammler function (2.49).

$$f_m = S \left(\frac{d_d^{S-1}}{\bar{d}^S} \right) e^{-\left(\frac{d_d}{\bar{d}} \right)^S} \quad (2.49)$$

where \bar{d} is the characteristic diameter of mass distribution and has a physical meaning that the ratio of summarized mass of oil droplets whose diameters are larger than \bar{d} to the total mass of all the oil droplets is 36.8%; The values of \bar{d} and S have a close relationship with the operating parameters of bearing chamber and can be defined as

$$\bar{d} = 2.13 \times 10^6 \left(\frac{\dots_d \tilde{S}^2 d_l^3}{\Gamma} \right)^{-0.611} \quad (2.50)$$

$$S = 27.7 \left(\frac{\dots_d \tilde{S}^2 d_l^3}{\Gamma} \right)^{-0.1445} \quad (2.51)$$

where \tilde{S} – angular velocity; Γ – surface tension coefficient

The momentum of oil film transferred from deposited droplets per unit time p_c is expressed as

$$p_c = \dots_d L u_{d0} \sum_{i=1}^n \left. \right\}_i \int_{d_{di}}^{d_{di+1}} S \left(\frac{d_d^{S-1}}{\bar{d}^S} \right) e^{-\left(\frac{d_d}{\bar{d}} \right)^S} dd_d \quad (2.52)$$

where L – oil mass flow rate supplied to bearing chamber.

Since the oil film is thin compared to the dimension of bearing chamber, the oil/air interfacial shear stress along the chamber circumference is treated as a constant. The pressure difference and acceleration inside oil film are neglected. The oil film has no movement in axial direction owing to the circumference movement of rotating elements.

At high rotational speed the momentum of oil film can overcome the gravity and wall shear force, and drag oil film along the chamber wall. The oil film force balance is described in Fig.2.4b. At low rotational speed, the movement of oil film at right side of the chamber (Fig.2.4a) is in the direction of gravity force, and the oil film force balance is also shown in Fig.2.4b. But the movement of oil film at left side of the chamber is opposite to the bearing rotational direction because of small oil/air interfacial shear force and oil film momentum. The oil film force balance is presented in Fig.2.4c.

$$\begin{cases} \frac{p_c}{s} + \bar{\tau}_{int} + 3\bar{u} = \rho_d g h \sin \alpha & 0^\circ < \alpha \leq 180^\circ \\ \frac{p_c}{s} + \bar{\tau}_{int} - 3\bar{u} = \rho_d g h \sin \alpha & 180^\circ < \alpha \leq 360^\circ \end{cases} \quad (2.56)$$

where s – internal surface area of bearing chamber.

The represented in [30] model makes a contribution to provide more practical and feasible technical approach, which is not only for the study of droplet-film interaction and physical behavior in bearing chambers with oil/air two-phase flow phenomena, but also useful for an insight into the essence of physical course through droplet movement and deposition, film formation and flow. Comparison between the theoretical results and experimental results shows the correctness and validity of the theoretical model. There is a good agreement between theoretical results and experimental results [8], except that the theoretical results are slightly larger than the experimental results, especially in the vent port region. The reason of this inconsistency is probably that the balancing state between entering flows and exit flows of the oil is difficult to be determined, which needs further study.

2.3 A coupled 1D film hydrodynamics and core gas flow model for air-oil flows in aero-engine bearing chambers

A robust 1D film hydrodynamic model coupled with a 1D core gas model is represented in [32]. It can be used to predict the instantaneous mean core gas speed, film interface shear stress and liquid film distribution within an idealised bearing chamber. The bearing chamber is idealised as a one-dimensional (2D) domain with a predominantly azimuthal flow in both the rotational oil film and core gas such that axial components may be ignored. The model is composed of two components; a 1D transient oil film hydrodynamics model [33-36] which is used to predict oil film distribution; a 1D core gas model of work [8] to predict the core gas speed within the chamber. A 1D system of depth-averaged film hydrodynamics equations is used to predict oil film thickness and mean speed distributions in the azimuthal direction under the influence of interface shear, gravity, pressure gradient and surface tension forces. The driving shear stress in the film model is obtained from the 1D core-gas model [8] based on an azimuthal gas momentum conservation equation which is coupled to the film model [33-36] through the interface shear stress and film interface velocity.

In the solution algorithm, film hydrodynamics model is sequentially coupled with the core gas dynamics model via the interfacial shear stress from the air that is driving the film as well the film interface speed which is used in the core gas momentum balance equation. Both models use an explicit time-stepping routine and low Courant numbers are required in order to guarantee numerical stability of the solution. The model was developed using a fourth order finite difference method for spatial discretisation and a first order explicit time scheme for temporal discretisation.

The depth-averaged Eulerian thin-film modelling (ETFM) approach presented in [33] is used. In the ETFM model, the thin-film flow is idealised as a two-dimensional incompressible Newtonian liquid of density, ρ_l and viscosity, μ_l flowing over a solid substrate and with a free-surface exposed to an incompressible Newtonian gas of density, ρ_g and viscosity, μ_g

. The film has a spatially varying height, $h(s, t,)$ and flows with a film velocity $u(s, y, t)$ - where s is the horizontal flow direction and y is the normal direction as shown in Figure 2.5.

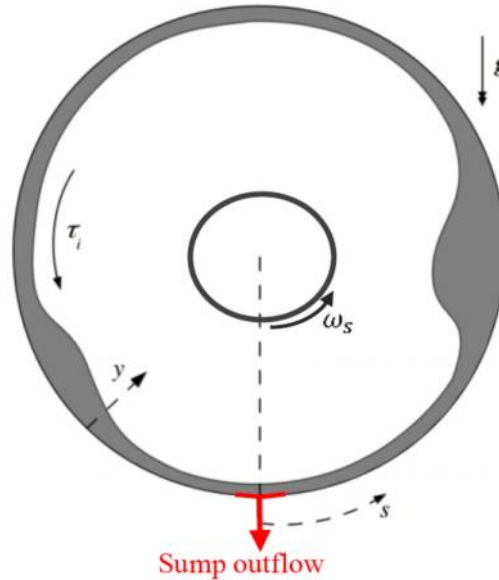


Figure 2.5. Thin-film rimming flow geometry and coordinate reference system used in the ETFM approach

The resulting film flow dynamics over the solid-substrate may be described by the depth averaged continuity and momentum equations given by Equations (2.57) and (2.58).

$$\frac{\partial h}{\partial t} + \frac{\partial q}{\partial s} = S_m, \quad (2.57)$$

$$\frac{\partial q}{\partial t} + \frac{\partial}{\partial s} \int_0^h uudy = - \frac{h}{\dots_l} \frac{\partial p_l}{\partial s} + \frac{h}{\dots_l} \frac{\partial \dagger k}{\partial s} + g_y h + S_{\dagger} + S_{MOM} \quad (2.58)$$

where $p_l = p_g - \dots g_y h$, is the film pressure which has a component from the interfacial gas pressure, p_g , and the film hydrostatic pressure, $\dots g_y h$. p_l is used to compute the film hydrostatic pressure gradient term, which is the first term on the right hand side (R.H.S.) of Equations (2.58). S_m and S_{MOM} are generic mass and source terms for the film domain.

Surface tension effects are represented in the surface tension term (second term on the R.H.S. of Eq. (2.58)), where \dagger is the surface tension coefficient for the liquid-gas interface, and k_j is the interface normal curvature in the j -direction

The third term on the R.H.S. of Eq. (2.58) represents the momentum source term due to film gravitational body forces in the direction of the film flow. Finally, the fourth source term on the R.H.S. of Eq. (2.58), S_{\dagger} , represents the balance of viscous shear forces on the film, including contributions from the interfacial shear stress driving the film, \dagger_i , and the wall

shear stress resisting fluid flow over the stationary outer chamber wall, \ddagger_c . The viscous source term, S_{\ddagger} may be computed according to Eq. (2.59)

$$S_{\ddagger} = \frac{\ddagger_i - \ddagger_c}{\dots l} \quad (2.59)$$

The film interface shear is estimated from a non-linear interaction with the core gas flow model [8]. In addition to shear and gravity forces, the surface tension and pressure gradients are included in order to extend the model to complex film phenomena such as pooling and shocks where these forces play a crucial role in solution stability and accuracy. A film profile function is assumed a-priori and used to evaluate the inertia integral. In the present study, a quartic film velocity profile has been used, which is capable of adequately representing both planar unidirectional film flows as well as non-unidirectional films with local flow separation and recirculations within the film.

For simplicity, the present film model ignores the effects of film momentum and core gas speed of the air entrained into the film and oil droplets suspended in the core flow. These conditions have however been observed to occur in bearing chamber representative conditions. Incorporating these effects is recommended as an area for future research and envisages that this would involve the addition of a film scalar transport equation for the entrained air, with appropriate source and sink terms from the entrained air mass. This would be coupled to the film momentum equation (2.58) through an additional source terms to account for the effects of locally entrained air on the film velocity. A similar approach would be envisaged for the effect of suspended oil droplets on the core gas dynamics.

The core gas flow in the annular space of the chamber is set into motion by the momentum transfer from the rotating shaft. The rotating air also exchanges momentum with the incoming sealing air flow as well as the film coated stationary outer wall resulting in a mean core gas speed, \underline{u}_g .

A 1-D core gas dynamics model is used to estimate this core gas speed based on the principal of angular momentum conservation as previously described in [8] taking into account the effects of sealing air as well as the interface shear stress acting on the film. The azimuthal momentum balance is then given by Eq. (2.60).

$$M_{shaft} - M_{film} = -M_{sealingAir} \quad (2.60)$$

where M_{shaft} is the shaft moment, M_{film} the film interface moment and $M_{sealingAir}$ is the momentum change associated with the incoming sealing air flow. The film interface is treated as a moving wall translating at the interface film speed, $u_i(s, t)$ and a smooth pipe analogy is used to idealise the core gas flow. The various moments due to the shaft and film effects on the core air flow may be estimated according to the following relations;

$$M_{shaft} = \ddagger_s A_s r_s = \ddagger_s (2f r_s^2 L) \quad (2.61)$$

$$M_{film} = \ddagger_i A_i r_i = \ddagger_i (2f (r_c - \bar{h})^2 L) \quad (2.62)$$

where \dagger_s is the shear stress on the rotating shaft, \dagger_i is the interfacial shear stress on the moving film, r_c is the stationary chamber wall radius; r_s is the rotating shaft radius; \bar{h} is the mean film thickness along the chamber wall obtained from the described above film hydrodynamics model and L is the axial length of the chamber. Taking the smooth pipe analogy as in [8] the Blasius friction factor, $\}$, may be used to estimate the shaft and interface shear stresses according to;

$$\dagger_s = \frac{\}_s}{8} \dots_g (\check{S}_s r_s - \bar{u}_g)^2, \quad (2.63)$$

$$\dagger_i = \frac{\}_i}{8} \dots_g (\bar{u}_g - u_i)^2 \quad (2.64)$$

where \dots_g is the gas density, \check{S}_s is the shaft rotational speed, \bar{u}_g is the mean azimuthal speed of the core gas and u_i is the film interface speed which is obtained from the instantaneous mean film speed, $u_i(s, t)$, according to Eq. (2.65)

$$u_i(s, t) = \frac{3}{2} u_l(s, t). \quad (2.65)$$

The Blasius friction factors, $\}_s$ and $\}_i$ for the rotating shaft and the moving film interface are computed based on a smooth pipe analogy of the core air flow according to Equations (2.66) and (2.67).

$$\}_s = 0.316 (Re_{g,s})^{-0.25} = 0.316 \left(\frac{\dots_g D_h (\check{S}_s r_s - \bar{u}_g)}{\sim_g} \right)^{-0.25} \quad (2.66)$$

$$\}_i = 0.316 (Re_{g,i})^{-0.25} = 0.316 \left(\frac{\dots_g D_h (u_i - \bar{u}_g)}{\sim_g} \right)^{-0.25} \quad (2.67)$$

Where the hydraulic diameter of the core gas in the presence of the film is estimated as

$$D_h = \left[\frac{4A}{U} \right] = \left[\frac{2L(r_c - \bar{h} - r_s)}{(L + r_c - \bar{h} - r_s)} \right] \quad (2.68)$$

Finally, the contribution from the sealing air flow is computed according to Eq. (2.69).

$$M_{sealingAir} = \dot{m}_{g,in} r_{g,in} (u_{g,t,in} - \bar{u}_g) \quad (2.69)$$

By solving the governing momentum equation for the core gas flow, Eq. (2.60), the mean core gas speed \bar{u}_g may be reliably estimated. The core gas flow model is coupled to the film hydrodynamics model through the interface film speed, u_i , which is obtained from the film hydrodynamics model used in (2.65) and (2.69) to estimate \bar{u}_g , and in turn, the interface shear stress, \ddagger_i from the core gas model in (2.64) is used to drive the moving film. This results in a non-linear coupling between the two models. The core gas equation (2.60) was iteratively solved using the non-linear system solver fsolve in MATLAB.

The represented in [32] model has been evaluated against existing experimental measurements from literature for oil film thickness in a test chamber. The air only shear stress model is shown to slightly over-predict film thicknesses and under-predict the interface shear stress, however including droplet-film momentum transfer through an equivalent droplet induced interface shear stress model is shown to lead to improved agreement with the experimental measurements. Further research is recommended in order to improve the robustness of this droplet-film momentum transfer model and include the effects of entrained air and suspended oil on air film and core gas dynamics.

3. CFD modelling of multiphase flow in the bearing chamber

A number of studies focused on numerical simulation of the air-oil flow behaviour are performed in the Gas Turbine and Transmissions Research Centre, University of Nottingham. Farrall et al. [31] developed a modelling methodology for film flow, incorporating a calculation using the commercial computational fluid dynamics CFD-code CFX4.3 to provide information regarding the distribution of the interfacial shear, mass, and momentum to the film. This paper includes the addition of boundary conditions for the vent and scavenge together with a comparison to experimental results obtained from ITS, University of Karlsruhe.

A thin film model developed for calculating the oil film flow in aero-engine bearing chamber is described in [29]. The performance of the model, which has been implemented in the commercial computational fluid dynamics software product: ANSYS Fluent, is benchmarked by comparing the computational results obtained from a Nottingham UTC in-house code and a development version of Fluent. Both codes are used to solve thin film flow in a test case configuration and based on the same finite area method.

In the paper [37], were represented results for the application of an Eulerian-Lagrangian technique to the transient simulation of an oil film formation on the walls of an aeroengine bearing chamber. The Volume of Fluid (VoF) technique offers a potential platform to model droplet-film interaction; however, it requires fine mesh details to capture the flow to the droplet level. A Lagrangian formulation is therefore proposed to represent the droplets as source terms in the Navier-Stokes equation while the film is represented using VoF.

The paper [38] is focused on the simulation of the oil behaviour inside KIT bearing chamber. The oil phase in the chamber can take different forms e.g. sprays, droplets, thin films or a combination of those. Since the use of VOF requires a refined mesh in the oil region, an adaptive mesh approach based on the volume of fluid gradient is developed and validated to control the total cell count for some of the cases reported here and limit simulation costs.

Volume of Fluid (VOF) CFD approach for the transient simulation of air/oil flows inside an aeroengine bearing chamber requires relatively fine grids and consequently small time-steps to sufficiently resolve the formation of oil films and their interaction with air flows. The need to achieve a stationary-state which requires flow times on the order of seconds makes the compromise between simulation accuracy and simulation times a challenging choice when using the VOF method. In the paper [39], the use of the Compressive Interface Reconstruction scheme with bounded second order implicit time discretization has enabled a significant speed-up of the simulation times against the previously adopted explicit Geometric-Reconstruction scheme.

Numerical methodologies for flow and heat transfer modelling in the rotor-stator systems encompass methods of the direct numerical simulation (DNS), Reynolds-averaged Navier-Stokes equations (RANS) with the turbulence models both in the general-purpose form as incorporated in the commercial computational fluid dynamics (CFD) software, and often specially modified to be used in the rotating-disk systems. They include different modifications of standard k-e, k-w and Reynolds-stress models (RSM); large-eddy simulations (LES) approach is also quite widely used.

Despite their relative geometric simplicity, enclosed rotating disk flows contain a complex physics, which makes their modelling a very challenging task for numerical methods. The flow problem presents indeed several complexities, such as the high rotation rates,

confinement effects, the coexistence of laminar, transitional and highly turbulent flow regions, three-dimensional precessing vortical structures, very thin 3D turbulent boundary layers along the disks, strong curvature of the streamlines, recirculation zones etc. When an axisymmetric jet is superimposed on this flow and impinges onto the rotating disk in a confined rotor-stator system, the flow pattern becomes even more complex with the interaction between the jet and the secondary rotor-stator flow. Numerically, there are also some additional technical constraints due to firstly the singularity in the Navier-Stokes equations when dealing with cylindrical coordinates in cylindrical (and not annular) geometries and secondly the choice of the boundary conditions at the outlet to ensure the mass conservation. Thus, most of the studies up to now have been dedicated to either enclosed rotor-stator flows without jet or impinging jet flows on a flat plate without rotation and more rarely to both problems at the same time. [40]

Three types of problems arise in the numerical treatment of free boundaries: their discrete representation, their evolution in time, and the manner in which boundary conditions are imposed on them.

In summary, the VOF method offers a region-following scheme with minimum storage requirements. Furthermore, because it follows regions rather than surfaces, all logic problems associated with intersecting surfaces are avoided with the VOF technique. The method is also applicable to three-dimensional computations, where its conservative use of stored information is highly advantageous. [41]

3.1 CFD modeling of Fluid and Gas Dynamics problems

The University of Nottingham Technology Centre (UTC) in Gas Turbine Transmission Systems has been conducting experimental and modelling work to understand the complex flow in the bearing chamber. Modelling the flow in the bearing chamber is complex because of the issues involved in representing the fluid phases present. The Volume of Fluid (VoF) method is one of the most commonly used for representing incompressible multiphase segregated flows. VoF only techniques, however, requires fine mesh details if the flow has to be captured to the droplet level of resolution [42]. Such detailed resolution would not be practical for the complete chamber geometry because of the prohibitively expensive computational overhead requirements. These authors have used enhanced VoF approaches to model bearing chamber flows for which a film generator was used. [37]

According to the [37] the flow is seen to consist of two-phase flow of air and oil. The oil phase, however, consists of two components, the flowing film and the droplets entrained in the air phase. The continuum of the air and the flowing oil phases are represented with the enhanced Eulerian VoF formulation. It should be mentioned that the droplets, when formulated in Lagrangian reference frame, are not by default coupled to the Eulerian phases. The Lagrangian formulation used is the so called Disperse Phase Model (DPM), whereas the droplets (DPM particles) are rather not resolved but represented in a mesh independent formulation that can be tracked in a 3D space. A Lagrangian formulation is used to represent the droplets as source terms in the Navier-Stokes equations. This effectively reduces the need to resolve the droplets to the computational mesh. The mesh density closer to the walls and regions with film is refined; a coarser mesh is used in the air phase thus potentially reducing computational power requirements.

Fig. 3.1 shows a simplified bearing chamber [37]. The chamber is located in proximity to the combustion chamber of the gas turbine.

The DPM-VoF model is schematically described in Fig. 3.2. A primary Lagrangian droplet approaches a surface. The surface can be a wall boundary or a free-surface. Fig. 3.2 illustrates how the mass and momentum are transferred between droplets (DPM) and film (VoF).

Practically this is done by exchanging quantities across the phases using source terms. The splashing outcomes from droplet impact are determined from the inertia and fluid parameters. The parameters that determine the outcome of a droplet impact on a film are the Weber, Reynolds numbers, as well as the relative film thickness. From these parameters the splashing conditions are determined. The number of splashed droplets, N_s , is determined from correlations to generate new DPM particles. The mass fraction absorbed, α , is governed by the balance between the predicted number of splashing droplets and oncoming particles.

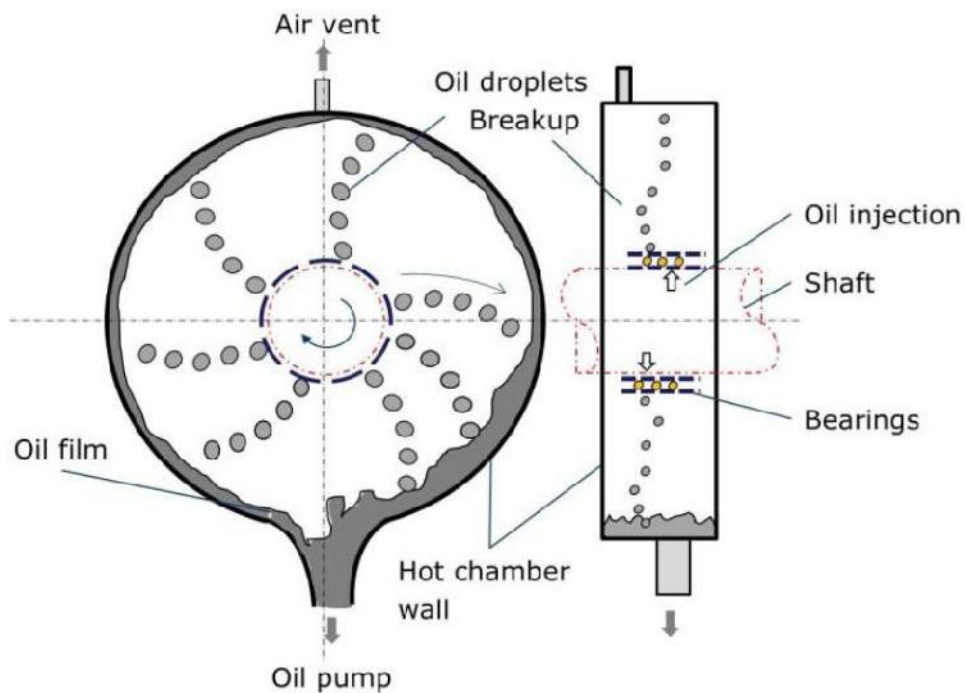


Figure 3.1. A simplified representation of the aero-engine bearing chamber

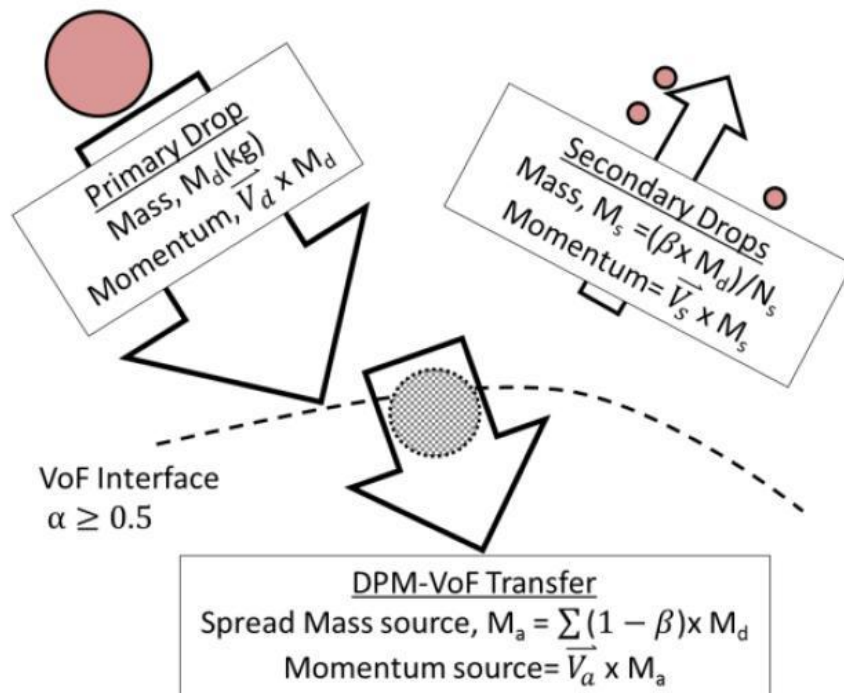


Figure 3.2. DPM-VoF Model schematic

Rotating Inlet Distributor (RID) model can be schematically represented as shown in Fig. 3.3, based on Chandra et al. [13, 37]. The RID encases the shaft. Oil is fed into the volume between the shaft and walls of the RID. The wall of the RID has several holes randomly distributed around it.

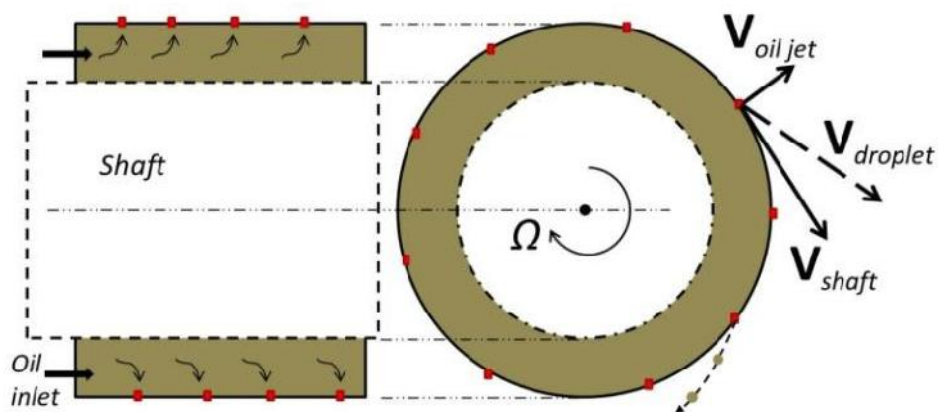


Figure 3.3. Schematic of the Rotating Inlet Distributor (RID)

For a stationary shaft, the velocity at which the oil leaves the holes can be obtained from equation

$$V_{oiljet} = \frac{1}{N \dots \cdot A_h} \dot{M}_{RID}$$

where \dot{M}_{RID} is the feed rate in kg/s, of the oil into the RID chamber and A_h is the area of each of the N holes.

The droplets initial velocities can be estimated from the vector components of the shaft tangential components and the oil jet velocity.

A complex air-oil interacting flow emerges within the bearing chamber as illustrated in Fig. 3.4. The oil escapes from the bearings in the form of film, ligaments or droplets of reasonable size which interact with the air. The formation of an oil film on the outer walls of the chamber is desirable as it facilitates its collection and removal but also permits the cooling of the chamber which can be located in challenging environments within the engine core. A suitable prediction tool must include oil representation in the form of droplets and continuous film, in a highly sheared environment, with the ability to exchange mass, momentum and energy between the two representations, but also interact with the surrounding air and the walls. [29]

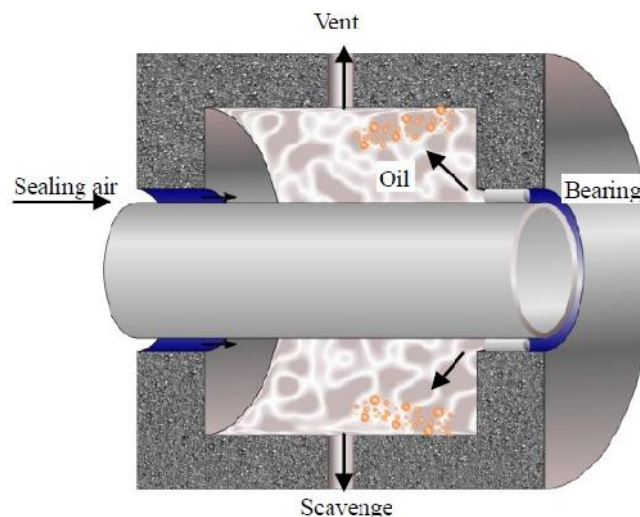


Figure 3.4. Illustration of air-droplets-film interaction in bearing chamber

An internal shaft is typically rotating at very high speed and drives the core air flow and air-oil droplet mixture, and possibly further surface interactions. In bearing chambers, sealing pressurized air is commonly used to prevent oil leakage. Relatively cool oil is injected to provide heat-to-oil cooling of walls and bearings to keep them below a critical temperature relevant to minimizing oil degradation. All these complex flow features are influenced by the collection, convection and removal of the oil film flow on the wall. [29]

According to the [43] all computations of system are performed using a cell-centre-based finite volume method on a block structured structural grid. The solution procedure is based on the pressure implicit with splitting of operators algorithm for pressure and velocity coupling in transient flows. The momentum transport equation is discretized with a second order Upwind method. The temporal discretization is carried out via the explicit first order backward difference method. Second order accuracy for the temporal discretization cannot be achieved due to the use of a geometric reconstruction scheme for the interface and an adaptive time step control which both require explicit first order accuracy. The adaptive time step is adjusted at the beginning of every time iteration loop to give a global Courant-Friedrichs-Lewy condition.

Model of the bearing chamber [43] is shown in Fig. 3.5.

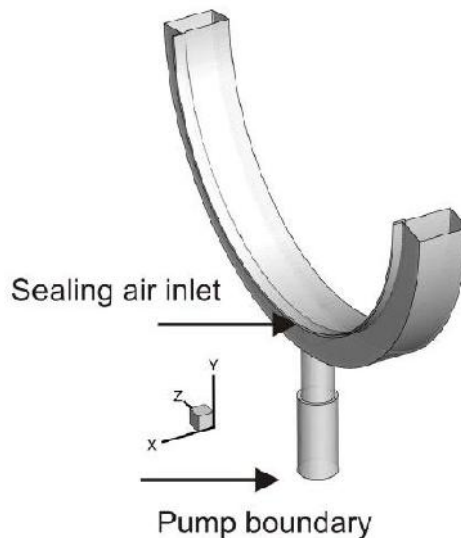


Figure 3.5. 3D model of the investigated bearing chamber

The end of the scavenge line is provided with a cylinder filled with oil and started draining at constant mass flow at the beginning of the simulation time. The volume of the cylinder was such to keep the pumping effect throughout the simulation i.e. until a quasi stationary state was achieved in the chamber. The rotating shaft is defined as a moving wall with a rotational speed of 3500rpm. The oil enters the domain via the side wall of the chamber with an assumed height and an inlet swirl of 45 in direction of shaft rotation, modelling the oil coming from a roller bearing. Introducing the oil as a film should not limit the accuracy of the simulation.

Sealing air is introduced in the domain via the labyrinth duct. The velocity profile at the sealing air inlet was calculated separately in a 2D axisymmetric labyrinth seal model to ensure appropriate profiles. correct sealing air inlet flow conditions are absolutely necessary for a detailed two-phase flow analysis inside a bearing chamber.

The VOF method works perfectly for laminar cases but shows large discrepancies for turbulent cases [43, 44]. It was shown that the discrepancies arise from the homogenous modelling approach which allows additional (false) momentum transfer through turbulent stresses between the phases. However, the interface behaves like a wall and the turbulent stresses just adjacent to the interface must be zero. This general deficiency of the VOF method is due to the absence of interface (gas-liquid) physics in the model i.e. the two phase interface is though captured but has no physical meaning in the flow governing equations.

As mentioned in the turbulence modelling section [43], the recirculation region can only be captured with interface treatment (see Fig. 3.6 (bottom)). It completely disappeared when calculated without interface treatment (Fig. 3.6 (top)).

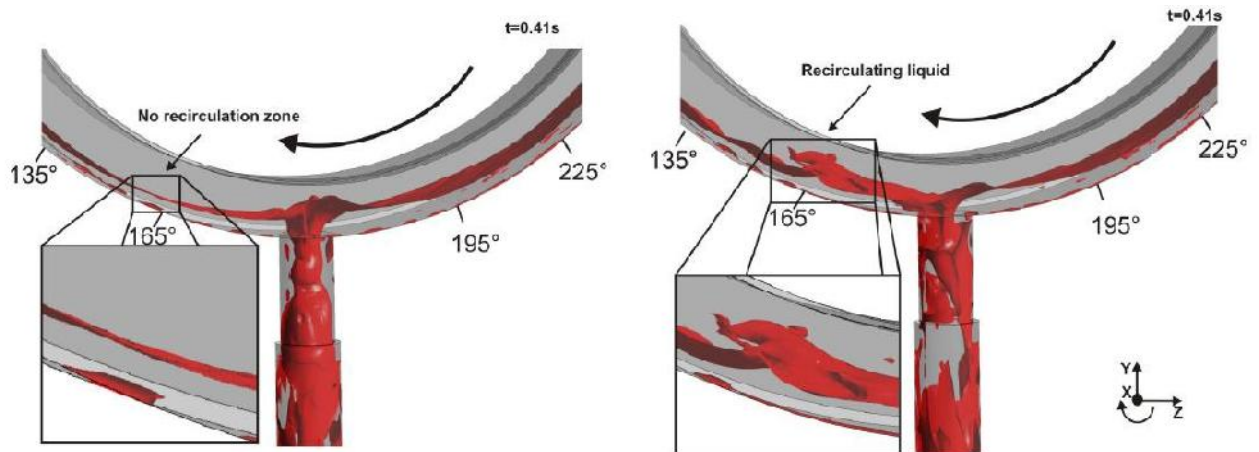


Figure 3.6. Comparison of oil volume fraction iso surface (50%) with (bottom) and without (top) interface treatment

Besides capturing the recirculation region at all, it was also found that the occurrence of recirculation is a highly dynamic phenomenon. Generally the film surface remains flat for the case without interface treatment whereas other instabilities (waves) are also evident with interface treatment. In contrast to the case without interface treatment, where a complete dry out was predicted, no large dry out (only small points) could be found in the case with interface treatment.

For the turbulence cases, plausible results could only be obtained by defining suitable interface physics usually referred to as interface treatment in literature. A simple interface treatment based on k - ϵ turbulence model is combined with the introduced methodology to correct the turbulent quantities near the interface. This interface treatment identifies the cells where the interface is located and forces the turbulent viscosity in these cells to zero. For this purpose a UDF was written to implement in the CFD solver. [43]

The CFD case presented ambioned to study the oil behavior throughout the chamber and to observe a full oil cycle from bearing to scavenge, ideally, by reproducing and improving the work carried as: a new mesh is created to improve compute times; oil inlet boundary conditions are revised. [38]

The adaptive mesh approach implemented in FLUENT can use several methods and criteria to refine the mesh (e.g. boundary, gradient or iso-value adaption methods). Because the important aspect of the bearing chamber simulation is the oil interface, the oil volume fraction gradient is chosen as the main refinement parameter. The Gradient Adaption Approach (GAA) assumes that maximum numerical challenges occur in regions of high-gradients for a chosen parameter, here the oil volume fraction. The error indicator (for a chosen parameter) can then be used as the main criterion to drive the mesh adaptation process. In addition, as the transition air-oil at the interface is not shock-like, the Curvature Method is advised for smooth transitions [45].

The parameters used for the adaptive mesh method are described in the following: Coarsen threshold-Refined threshold: 0.15-0.25 (Normalize Curvature Gradient Method); Minimum Cell Volume: $5 \times 10^{-11} \text{ m}^3$; Maximum number of Cells: 6×10^5 .

The simulation approach relies on the explicit Volume of Fluid Method coupled to a level-set function. The viscous model used is the SST k - ω scheme with turbulence damping. The Global Courant Number is set at 0.1 in support of the Geo-Reconstruct VOF Scheme

available in FLUENT. The time step is then set up as adaptable, updating following the Courant Number value. However, the time step value is also monitored and was capped at 10^6 s.

Unlike the refined fixed mesh simulation, the adaptive mesh simulation gives rise to a large amount of filaments and droplets leaving the bearing, which would seem intuitively correct. With the new oil morphology, the air flow and the initial oil velocity allow the droplets to move faster compare to the “thin continuous film”, displayed in Fig. 3.7 and Fig. 3.8. [38]

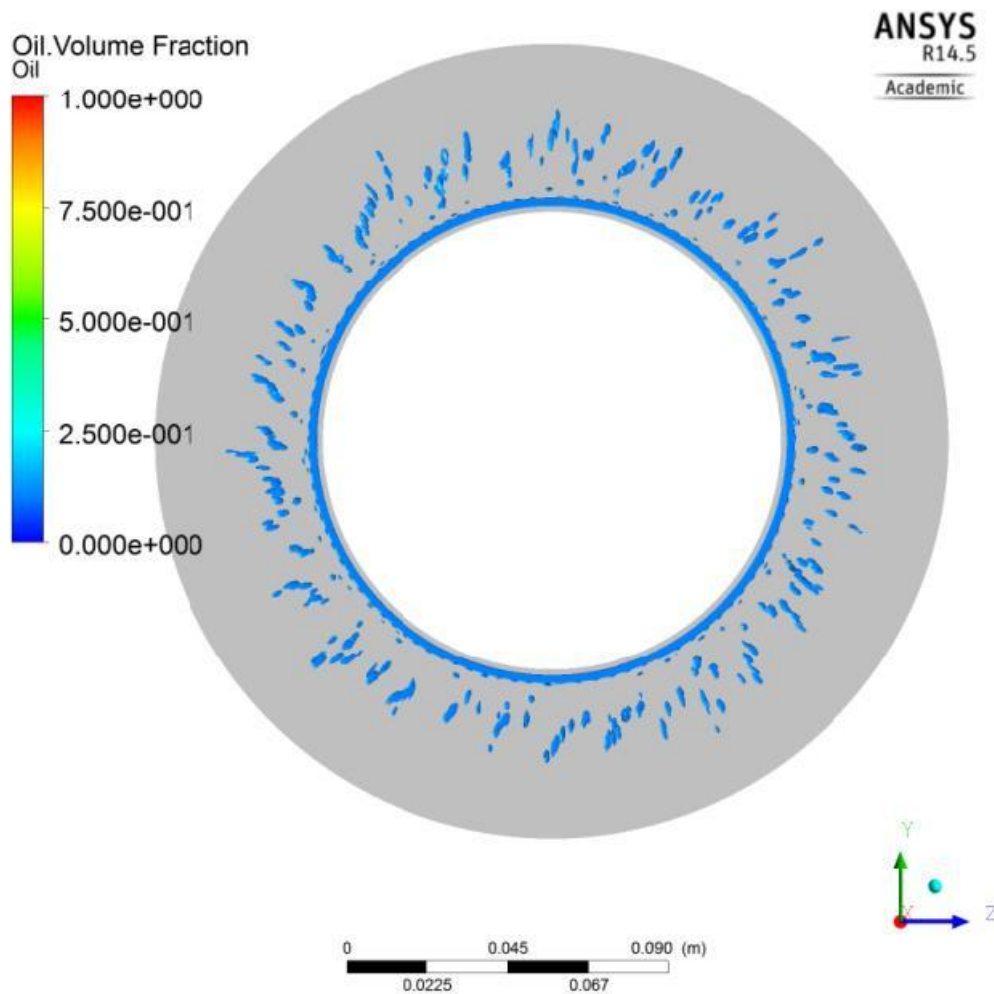


Figure 3.7. Isosurface of oil (oil volume fraction = 0.1) for the kit bearing chamber adaptive mesh simulation at $t=0.0034$ s

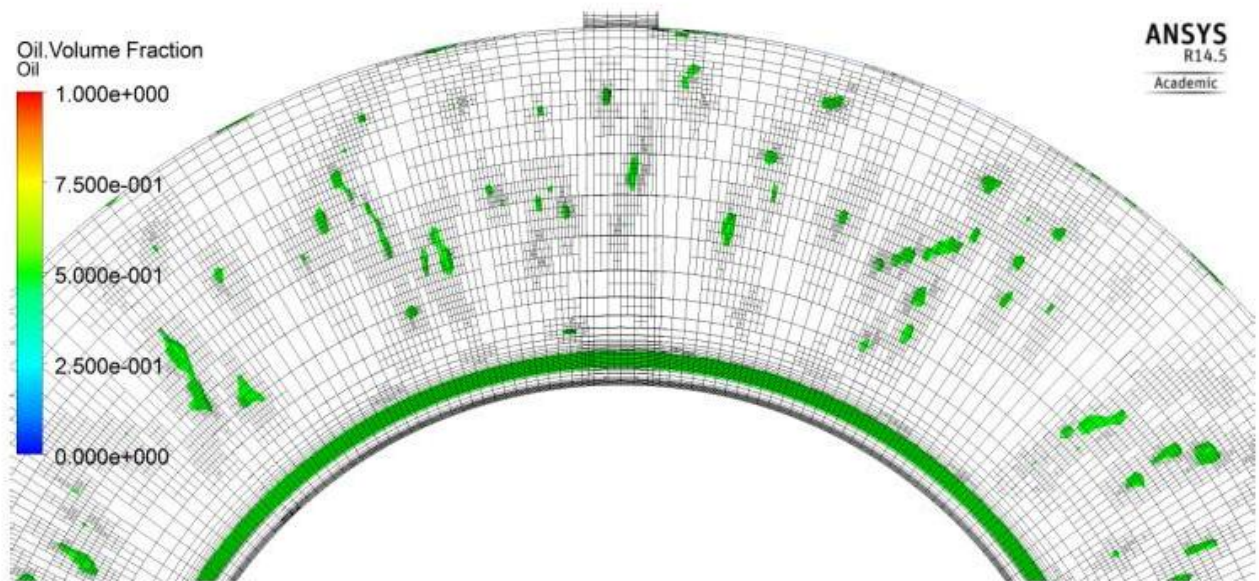


Figure 3.8. Partial view of the contour of oil (oil volume fraction = 0.5) for the kit bearing chamber adaptive mesh simulation at $t=0.0102s$ with the mesh visible

Adaptive mesh approach has allowed two essential features: (1) to (seemingly) better capture the oil morphology, including for higher oil volume fractions and (2) and do so at a fraction of the simulation cost. This approach has proved very promising, including on the (physical) modeling front. This simulation would benefit from running longer and would require validation next, though the required data are difficult to get by for such complex situation (viz. for droplets and filaments and a non-continuous film) and a full validation remains unlikely. [38]

According to the [46] for the two-phase flow modeling inside the oil-jet lubricated ball bearing, a volume fraction oil $\{\}_{oil}$ is used to mark the volume fraction of the oil phase in the VOF method. Then, $\{\}_{oil} = 0$ represents a cell that is empty of the oil and $\{\}_{oil} = 1$ represents a cell that is full of the oil. If $0 < \{\}_{oil} < 1$, it represents the interface between the oil phase and the air phase.

The subscript oil represents the oil phase properties. The interface between the oil and air phases is tracked by solving a continuity equation for the volume fraction of the oil phase. The continuity equation for the volume fraction of the oil phase is given by:

$$\frac{\partial}{\partial t}(\{\}_{oil} \dots_{oil}) + (\{\}_{oil} \dots_{oil} \bar{v}) = S_{\Gamma oil},$$

where \dots_{oil} is the oil density, \bar{v} is the velocity vector. The mass source term, $S_{\Gamma oil}$, on the right-hand side is zero for the VOF method signifying that there is no mass transfer across the interface [47].

The subscript air represents the air phase properties. In the VOF method, a single momentum equation is solved. The fields for all variables and properties are shared by both phases according to the following equation:

$$\frac{\partial}{\partial t}(\dots\bar{v}) + \nabla(\dots\bar{v}\bar{v}) = -\nabla p + \nabla(\sim(\nabla\bar{v} + \nabla\bar{v}^T)) + \dots\bar{g} + \bar{F},$$

where ... is the mixture density, \sim is the dynamic viscosity, p is the pressure, g is the gravity acceleration, \bar{F} is the external force due to the surface tension at the interface [46, 48]. The properties that appear in the momentum equation are volume-fraction-averaged properties.

The mesh images of the flow field are shown in Fig. 3.9.

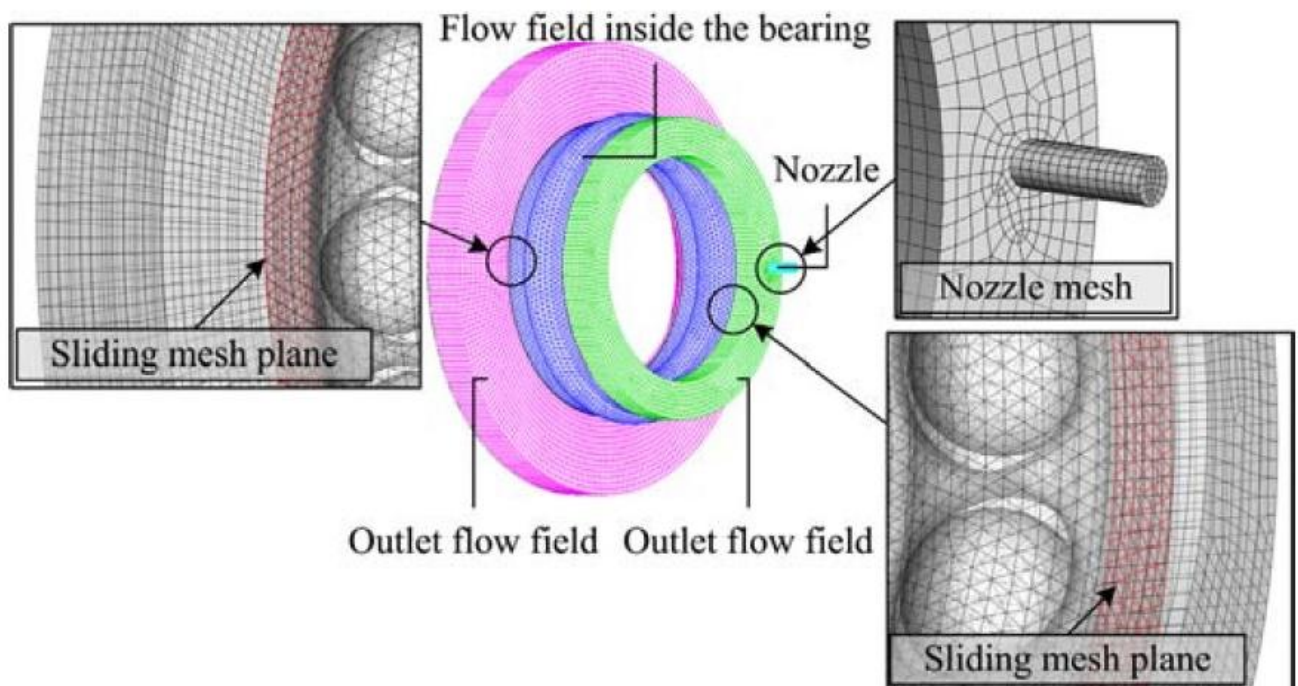
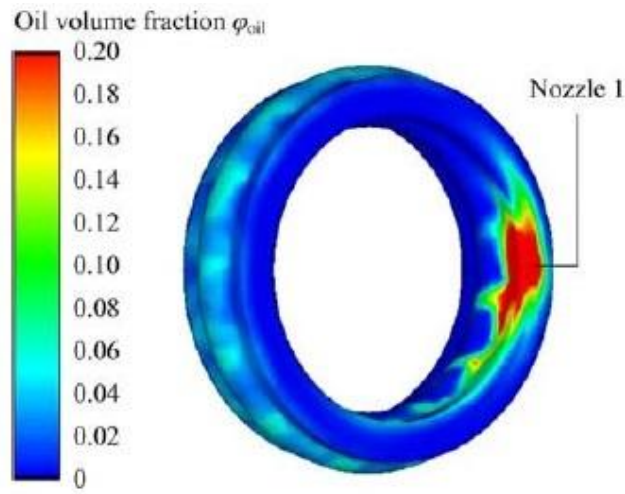


Figure 3.9. Calculating grid for the whole domain

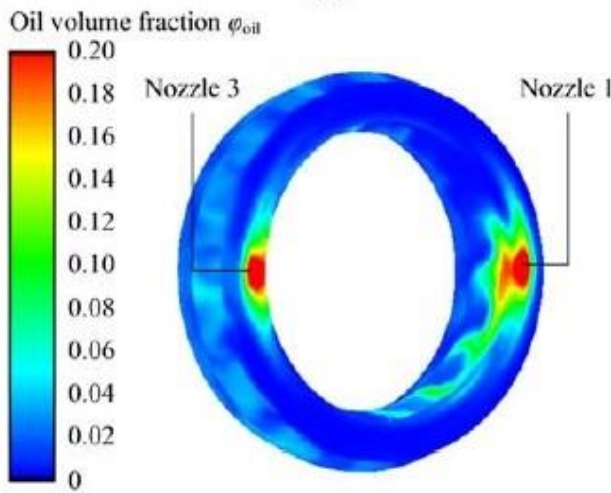
Fig. 3.10 shows the simulated air-oil distribution of different number of nozzles. The speed of the inner ring is 10,000 r/min and the oil-flow rate is 3.0 L/min. The oil viscosity is 0.02 Pa s in the calculation. The bearing temperature distribution is affected by the nonuniform air-oil distribution. The measured outer ring temperatures have represented the nonuniform characteristics, as shown in Fig. 3.10 (d) and (e).

It is seen that the circumferential air-oil distribution in the bearing is not uniform. The volume fraction of the oil phase quite close to the nozzle is much more than other positions inside the bearing. The oil volume fraction decreases along the rotation direction of the bearing. If even faster bearings are desired, the temperature difference of the outer ring should be

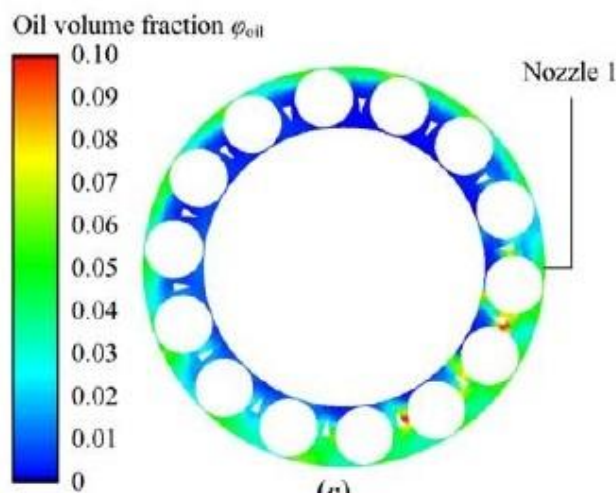
considered. When the bearing runs at higher speeds, the preload increases because of the thermal expansion caused the higher temperature. Further, the temperature difference makes the thermal expansion nonuniformity. To increase the calculation efficiency of the proposed CFD model, the effect of the temperature difference on the oil viscosity is neglected. The small temperature difference affects the oil viscosity little at higher temperatures. [46]



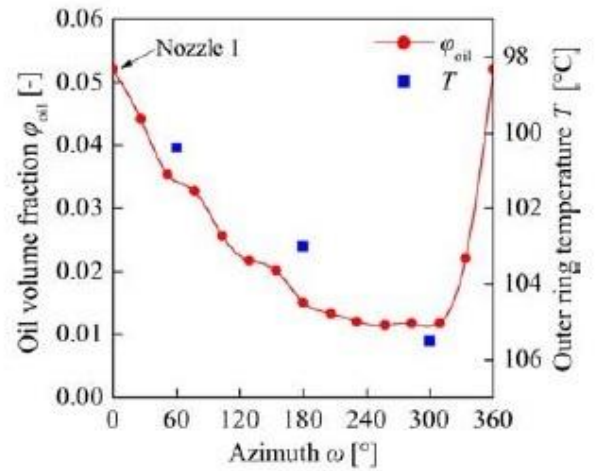
(a)



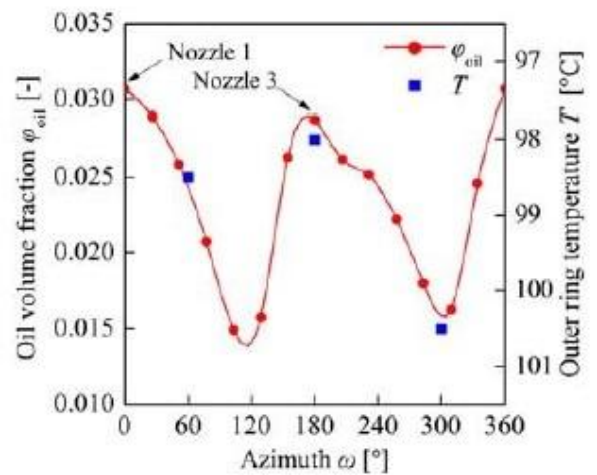
(b)



(c)



(d)



(e)

Figure 3.10. Nonuniform air-oil distribution inside the bearing.

(a) Oil volume fraction distribution under the single-nozzle oil-jet lubrication. (b) Oil volume fraction distribution under the dual nozzle oil-jet lubrication. (c) Oil volume fraction distribution due to the centrifugal force. (d) Average oil volume fraction and measured outer ring temperature under the single-nozzle oil-jet lubrication. (e) Average oil volume fraction and measured outer ring temperature under the dual nozzle oil-jet lubrication. [46]

In paper [49] a reasonable numerical simulation method is used to calculate a certain radial oil scoop. The velocity distribution of the internal air field in the lubrication structure and the oil distribution of the oil-gas two phase flow field were calculated and the scoop efficiency under different working conditions were calculated. Finally, the influence of the shaft rotation speed, the oil flow rate and the number of the oil nozzles on the scoop efficiency of the radial scoop is analyzed, and the reason of these regularities is analyzed in detail.

The mesh of domain and boundary conditions are presented in Fig. 3.11.

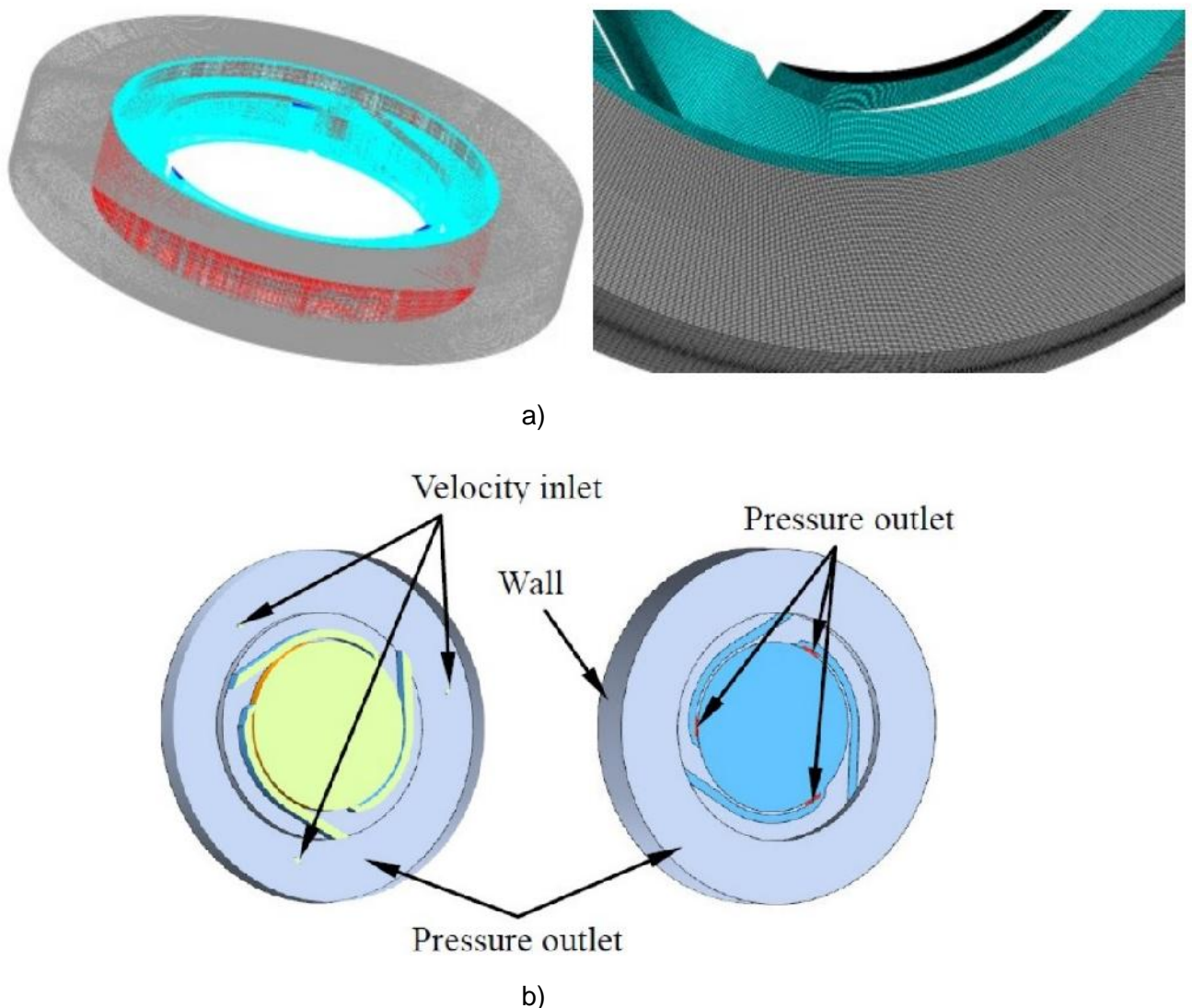


Figure 3.11. The part mesh of under-race lubrication (a) and calculate domain boundary conditions (b)

The oil is discharged from jet nozzle, when the oil jet through the air field in the bearing cavity reaches the radial oil scoop, and air will be mixed into the passage. At the same time, the centrifugal force generated by the high-speed rotation of the radial oil scoop is easy to separate the oil from the air and form a phase-separated flow. The VOF two-phase flow model and Realizable k- turbulence model are used for the calculation [49].

Distribution of air and oil field velocity at different speed are presented in Fig. 3.12 and Fig. 3.13.

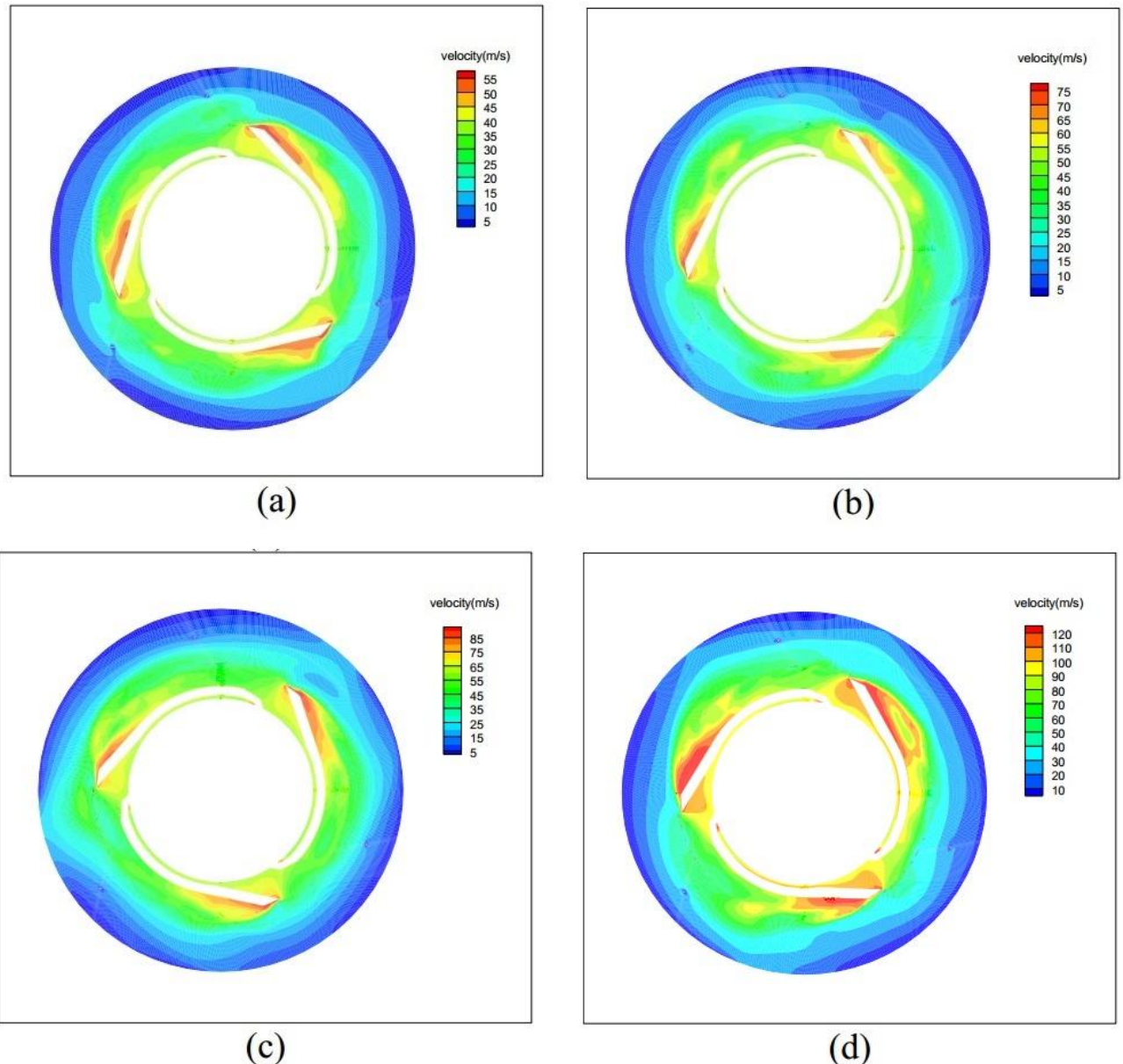


Figure 3.12. Distribution of air field velocity at different speed

The influence of the shaft rotating speed the oil flow rate and the number of the oil nozzles on the scoop efficiency of the radial scoop is analyzed [49], and the reason of these regularities is analyzed in detail:

1. The velocity distribution regularities of the air field at different speeds is the same, the higher shaft rotating speed, the higher air flow rate inside the inner-ring lubrication structure, the speed of the blade tip is the highest.
2. In high speed range, the scoop efficiency of the radial scoop decrease with the increase of the shaft rotating speed, and the increase of the shaft rotating speed leads to the adverse effect of the wind resistance and the centrifugal force greater than increasing the blade cutting the jet frequency.
3. The scoop efficiency of the radial scoop increases with the increase of the oil flow rate. The effect of the oil jet resistance on the wind resistance of the air to the collection oil is greater than the adverse effect of the deflection and splash.

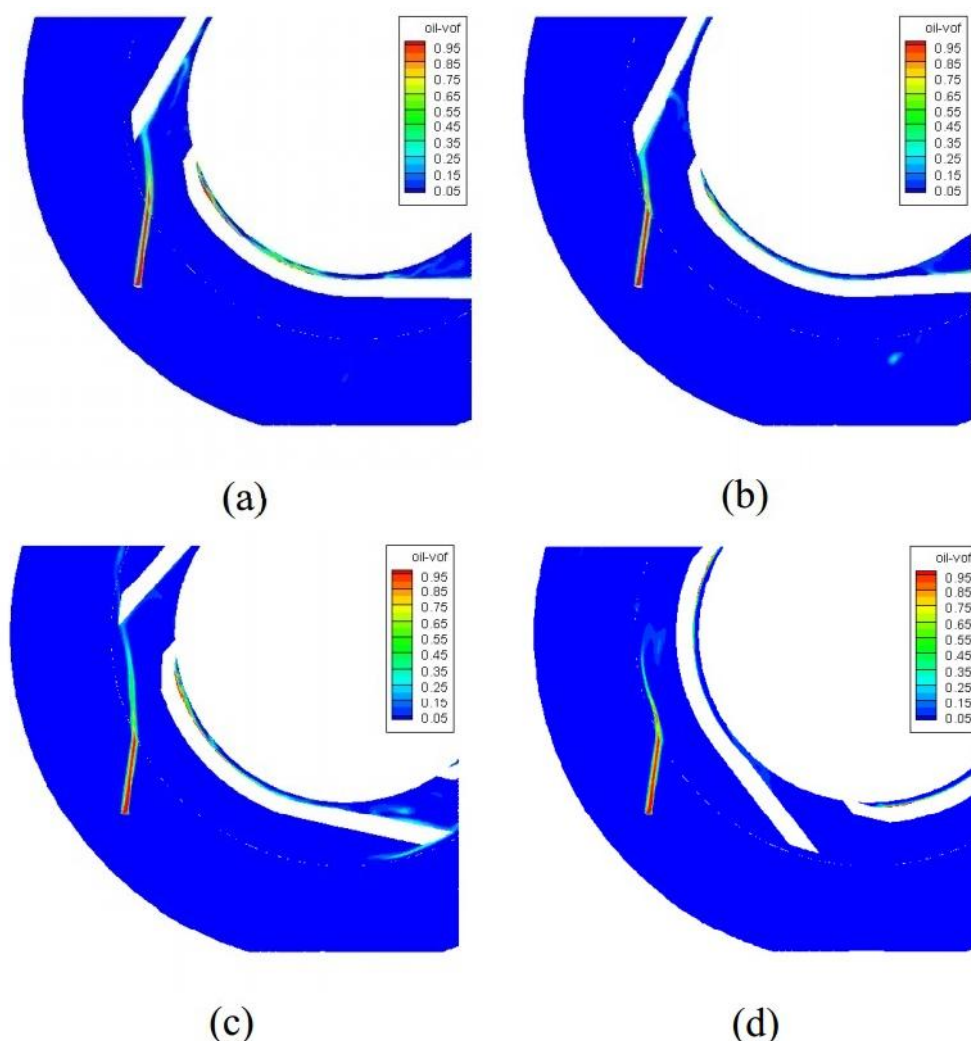


Figure 3.13. Distribution of oil field velocity at different speed

4. The scoop efficiency increases with the increase of the number of oil nozzles under the low speed conditions. When the oil inlet flow rate is low, the scoop efficiency decreases with the increase of the number of oil nozzles, and the high oil flow rate is reversed.

The work [50] presents an investigation of two numerical schemes that are available in ANSYS Fluent to track or capture the air-oil phase interface: the geometric reconstruction scheme and the compressive scheme. Both numerical schemes are used to model the oil outflow behavior in the most simplistic approximation of a journal bearing: a representation, rotating about its own axis, with a circumferentially constant, i.e. concentric, lubricating gap. Based on these simplifications, a three dimensional (3D) CFD sector model with rotationally periodic boundaries is considered.

The Fig. 3.14 and 3.15 illustrate how, compared to the baseline model, an increased time-step affects the CFD simulation results in steady state conditions, i.e. at an elapsed flow time of $t=0.02$ s, with respect to the phase interface resolution. For all simulations, the mesh from the baseline case, i.e. a total cell count of 1.42M, was used.

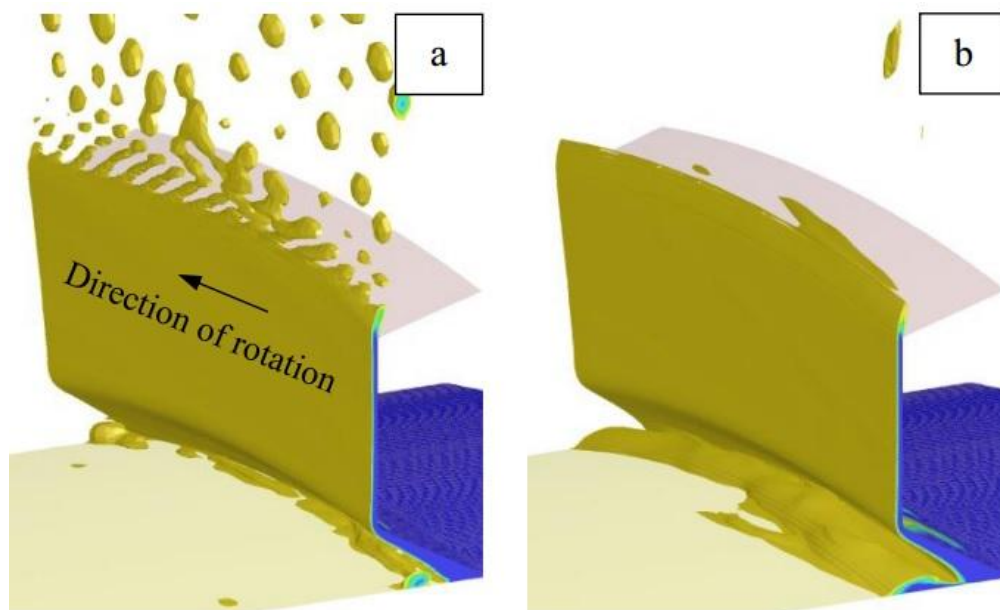


Figure 3.14. Geometric (a) and compressive, explicit (b) phase interface reconstruction with $t = 2 \times 10^{-7}$ s

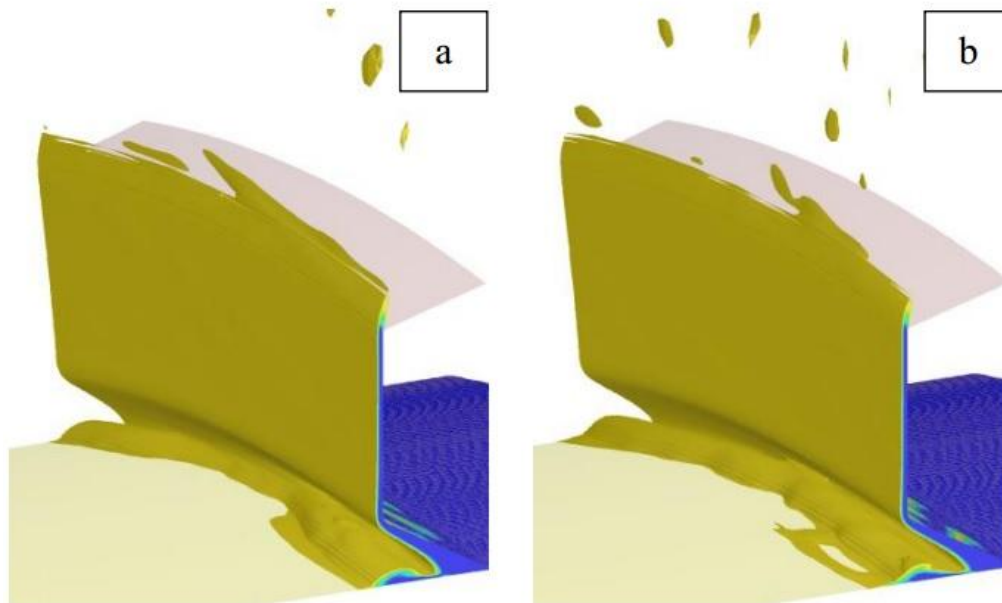


Figure 3.15. Compressive, implicit phase interface reconstruction with $t=2 \times 10^{-7}$ s (a) and $t=5 \times 10^{-7}$ s (b)

Table 3.1 lists the corresponding computing times required to simulate an elapsed flow time of $t = 0.02$ s.

As shown in Table 3.1, a significant overall reduction (-95.7%) in the computational time required to simulate an elapsed flow time of $t=0.02$ s can be achieved by using the implicit compressive phase interface reconstruction scheme, compared to the baseline settings with the geometric phase interface reconstruction.

Table 3.1. Comparison of computing times required to simulate an elapsed flow time of $t = 0.02$ s for different phase interface reconstruction schemes, discretization schemes and time-steps.

Phase interface reconstruction	Discretization scheme	Time-step Δt [s]	Computing time [min]	Max. C	Normalized oil film thickness H_f [-]
Geo.	Explicit	2×10^{-7}	6220	0.4	1.000
Comp.	Explicit	2×10^{-7}	7514	0.4	1.061
Comp.	Implicit	2×10^{-7}	8396	0.4	1.061
Comp.	Implicit	5×10^{-7}	5006	1.0	1.076
Comp.	Implicit	1×10^{-6}	2575	2.0	1.058
Comp.	Implicit	5×10^{-6}	554	10.0	1.076
Comp.	Implicit	1×10^{-5}	270	20.0	1.031

The analyses carried out allow the following key conclusions to be drawn [50].

1. The geometric phase interface reconstruction scheme is able to resolve detailed flow structures, such as ligaments and droplets. Qualitatively and quantitatively the simulated flow behavior is consistent with observations made on liquid flow over rotating cups and disks.
2. The compressive phase interface reconstruction scheme fails to resolve detailed flow structures such as ligaments and droplets.
3. The flow path prediction is independent of the chosen phase interface reconstruction scheme and the range of time-steps investigated for the case under consideration.
4. When considering the use of the compressive scheme for accelerating the computational time required to simulate a certain elapsed flow time, the convergence behavior of both interface reconstruction schemes must be considered. Changing from geometric to compressive phase interface reconstruction may not reduce the computational time required to simulate a certain elapsed flow time if the time-step remains unchanged.
5. If the accuracy of the compressive face interface reconstruction is deemed acceptable, a significant reduction in computational time required to simulate a certain elapsed flow time can be achieved by increasing the time-step.
6. The Reynolds equations approach provides an appropriate method for defining accurate inlet boundary conditions for the simulation of external oil flow from an eccentric journal bearing. This avoids CFD modeling of internal journal bearing flow.

An application of the validated numerical methodology to the drop impingement conditions relevant to aero-engine bearing chambers is presented in [51]. General description of a droplet impingement in the splashing regime is given. This is done qualitatively by characterizing the simulated temporal evolution of the crown's breakup and quantitatively by studying the wavelength selection of the instability driving the crown's sheet breakup. The numerical investigation continues with a parameter study where the influence of the We , Fr , Oh , α on the products of splashing is systematically studied by (initially) neglecting the wall-effects.

Flow field calculation of oil-gas two-phase is the basis of the heat and mass transfer study in the aero-engine bearing chamber. In order to analyze the oil-gas interaction in two-phase flow field, the oil /air two-way coupled numerical model is proposed in [52], the distributions of vortex, velocity and turbulence kinetic energy in a simplified bearing chamber are calculated, and the comparison between two-way and one-way coupled calculation results is carried out.

Two-way coupling calculation of the air field and oil droplet motion that is solved by using Lagrange method is adopted, as shown in Fig. 3.16. The oil droplet (the dispersed phase) motion will be influenced by that of the continuous one (air flow) and vice versa via displacement and interphase momentum, mass and heat transfer effects.

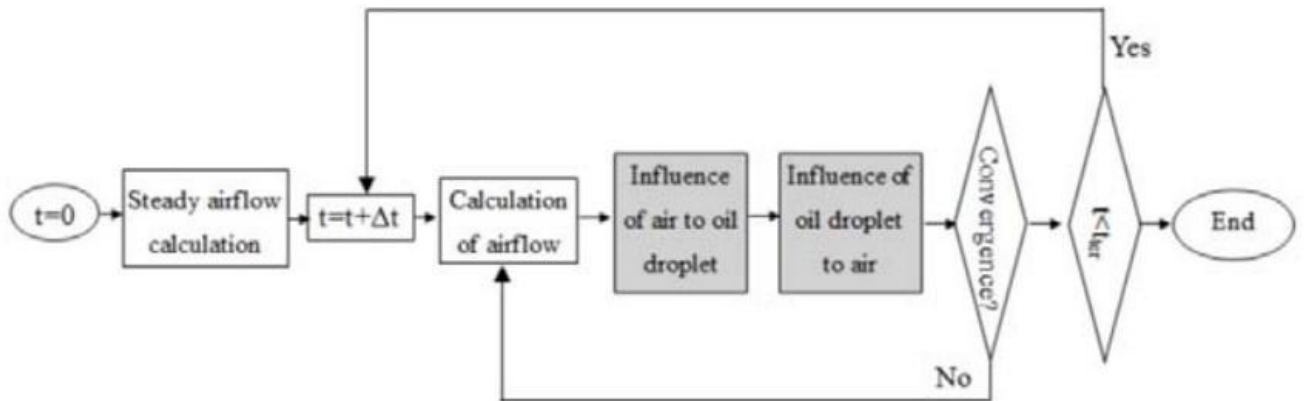


Figure 3.16. Calculation of two-way coupling model of oil and air

Fig. 3.17a shows the computed particle tracks of the released oil droplets in initial stage when the rotation speed is 8000 r/min, and the oil flow is 100 L/h. At this moment, the oil film has not been formed. As can be seen from the figure: After oil droplets impact with the wall, the oil droplet splash and secondary oil droplet generation occurred; And before the oil droplets impact with the wall, the trajectories of the majority of oil droplets have little difference compared with initial velocity, only a very few oil droplets (shown in blue trajectories) move irregularly in the bearing chamber, and fly out through the vent and scavenge port.

Fig. 3.17b shows the contours of air velocity computed by two-way coupling model in the middle section of the chamber when the rotation speed is 12000 r/min, and the oil flow is 100 L/h.

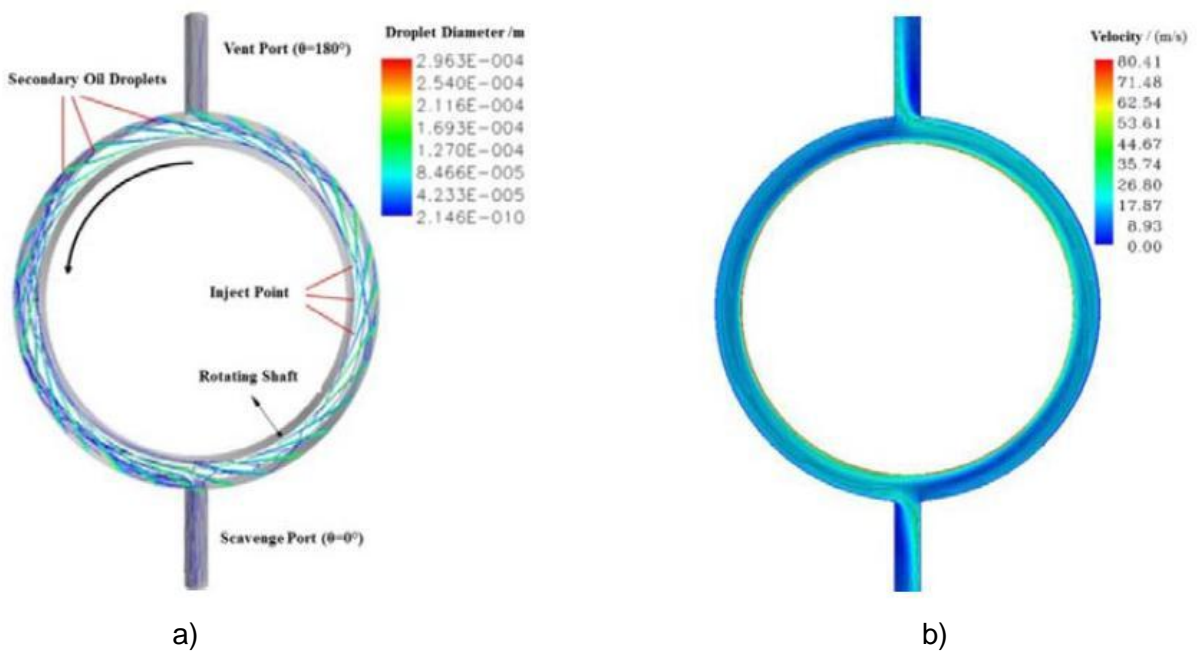


Figure 3.17. Particle tracks of oil droplets (8000 r/min, 100L/h) (a) and contours of air velocity (b)

Results show that the flow velocity of air and turbulent kinetic energy are affected greatly by the motion and evaporation of oil drops. Particularly, airflow speed of mainstream area in chamber decreases by at least 10%, and therefore the effect of oil droplets to air flow cannot be ignored in the calculation of two-phase flow. [52]

In [53] CLSVOF (coupled level set and Volume of Fluid) method is adopted to calculate oil-gas two-way coupling flow and the oil return performance. Considering the characteristics of oil-gas two-phase flow in the bearing chamber, two assumptions are made as follows: 1) the lubricating oil phase is Newtonian fluid and incompressible; 2) the oil and air are immiscible. CLSVOF method is an interface tracking method combining the advantages of Level-Set and VOF methods: on the one hand, the mass nonconservation of Level-Set method in the solving process is overcome; on the other hand, the deficiency of discontinuous interface and computational instability using VOF method are also resolved. Control equations:

$$\frac{\partial \dots(W)}{\partial t} + \nabla \cdot (U \dots(W)) = 0$$

$$\frac{\partial (\dots(W)U)}{\partial t} + \nabla \cdot (\dots(W)UU) = -\nabla p + \nabla \cdot (\dots(W)[\nabla U + (\nabla U)^T]) - F_{\dagger} + \dots(W)g$$

$$\frac{\partial (\dots(W)E)}{\partial t} + \nabla \cdot (\dots(W)E + p) = \nabla \cdot (k_{eff} \nabla T) + S_h,$$

where p , g , E , k_{eff} and S_h stand for pressure, gravity, the internal energy, effective thermal conductivity and the source term. F_{\dagger} is surface force, and CSF (continuum surface force) model is adopted:

$$F_{\dagger} = \dagger k u(W) \nabla W$$

$$u(W) = \frac{dH(W)}{dW} = \begin{cases} \frac{1 + \cos(fW/a)}{2a}, & |W| \leq a \\ 0, & \text{Otherwise} \end{cases}$$

VOF method is widely adopted currently, which can accurately simulate the oil-gas flow in the vicinity of scavenge offtake, especially for the capture of oil-gas interface. Alexandre in [38] established unsteady oil-gas two-phase calculation model based on the adaptive grid technique and VOF method, and studied the oil-gas movement and oil distribution in the initial stages. Adeniyi in [37] also employed VOF method to carry out the study of unsteady oil film distribution and heat transfer in the bearing chamber of eccentricity offtake with arc facet. [53]

According to the [33] a depth-averaged Eulerian thin-film Models approach has been successfully applied to the numerical simulation of smooth, shock, and pool type solutions. In this formulation, gravity, viscous, pressure gradient, surface tension forces, and inertia are accounted for. In smooth solutions, both pressure gradient and surface tension terms are

shown to be negligible compared to gravity and viscous terms. While in shock and pool solutions, surface tension and pressure gradients are found to play a significant role in the solutions and are of the same order as gravity and viscous terms. The effect of inertia representation has also been explored and stable shock, smooth and pool solutions are shown to be obtainable using both the simplified and full inertia formulations. However for shock and pool solutions, the simplified inertia formulation affects solution accuracy in the shock/pool region – leading to an over-predicted peak film thickness.

The results [33] demonstrate that using a fully implicit time scheme, stable smooth, shock, and pool solutions are obtained, even in cases where simplified inertia representations are used. For the rimming flow cases, where the steady solution is a stationary wave front, the capillary time constraint proposed by Denner and van Wachem [54] was found not to be a necessary condition for numerical stability.

Smooth solution, shock solution and pool solution were simulated using both a simplified- and a full-inertia representation in order to assess the role this plays in solution stability. The results of this sensitivity test for inertia representation are illustrated in Fig. 3.18. [33]

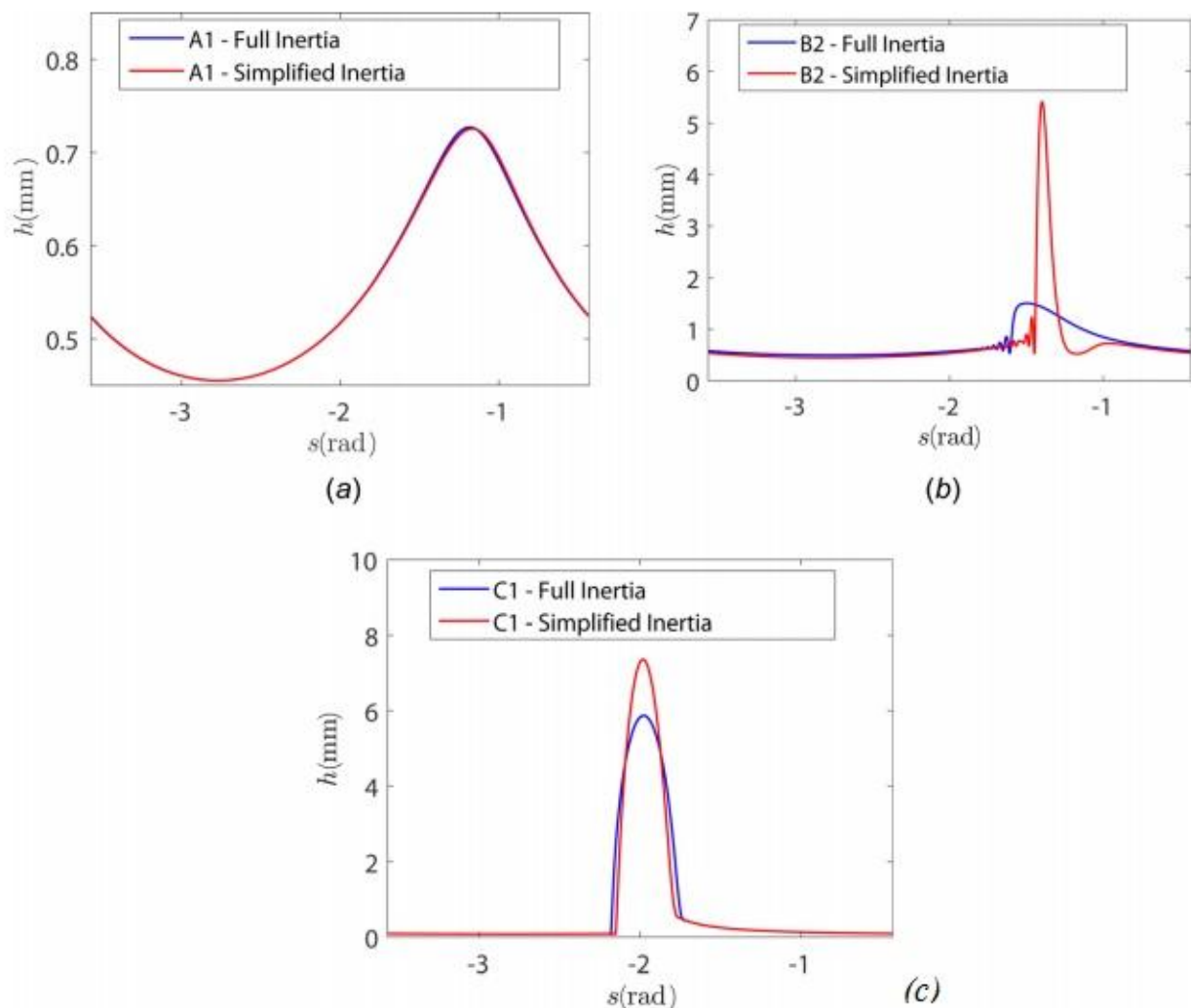


Figure 3.18. Effect of inertia representation on (a) smooth solution, (b) shock solution, and (c) pool solution

Stable smooth solutions were obtained for both the simplified inertia and full inertia as shown in Fig. 3.18a. The inertia representation sensitivity results for a shock solution are shown in Fig. 3.18b. Results for the simplified inertia case show significantly larger shock height than those obtained when the corrective source term is included to recover a full inertia formulation. Inertia effects affect the accuracy of shock solution considerably with the simplified inertia formulation shown to introduce significant errors. Similar findings to the shock solutions are observed for pool solutions as shown in Fig. 3.18c.

Augmenting the surface tension leads to an artificial smoothing of the solution, creating larger wavelength and low amplitude capillary waves that are easily resolvable on a coarse computational grid. This tends to result in a more stable solution that is easily attainable. On the other hand, with low surface tension solutions, low wavelength and high amplitude capillary waves are produced which require a much finer spatial grid resolution. Using a large surface tension coefficient, however, introduces uncertainty and may lead to excess damping of the film profile. This is illustrated by the results in Fig. 3.19, where using very high surface tension values (e.g., three orders of magnitude above the physical surface tension) results in a modified shock position and peak film thickness. The use of solution strategies depending on high surface tension should therefore be carried out with caution as significant artificial smoothing of the solution may result. [33]

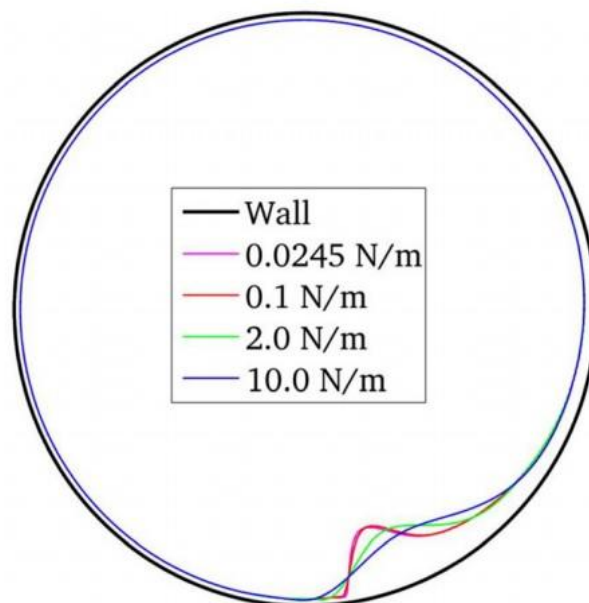


Figure 3.19. Polar plot of film solution illustrating the artificial smoothing of pool solutions due to the use of very high surface tension coefficients

An assessment of implicit and explicit time schemes has revealed that for stationary wave fronts such as in the case of rimming flows, fully implicit schemes offer considerable computational saving and the capillary time-step constraint is not a necessary condition for stability in these cases. However, for traveling wave fronts as in the case of falling wavy films, the capillary time-step constraint must be observed and this results in very low CFL (Courant–Friedrichs–Lewy) for which the explicit MacCormack scheme is more efficient than a full implicit scheme. [33]

3.2 CFD modelling of oil film behaviour

Complicated interaction between the oil film and the air, oil droplets, solid wall will occur when the oil film moves on the bearing chamber wall, as shown in Fig. 3.20, including the shear forces of air to the oil film surface, the oil droplet impact to the oil film, the heat transfer among the air, the oil film and the wall, the oil film stripping. [55]

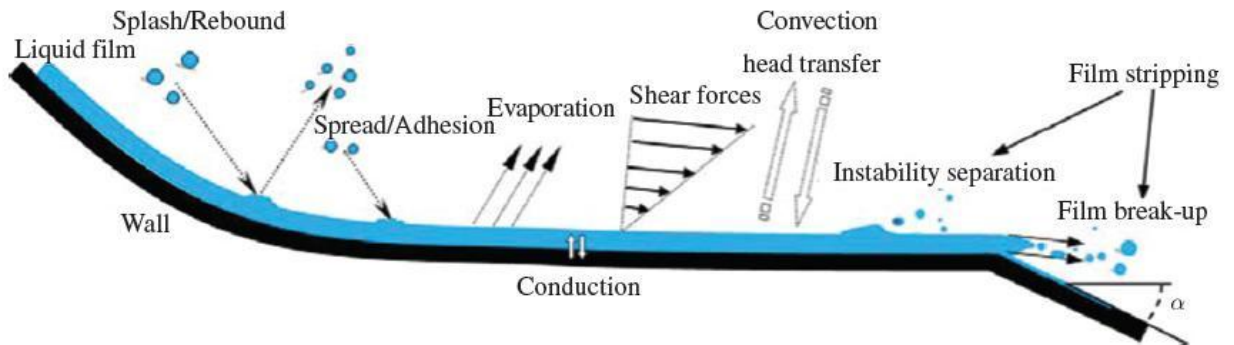


Figure 3.20. Mechanisms of mass, momentum and heat transfer for the oil film

Fig. 3.21 shows the oil film thickness distribution contours at different rotation speeds, and the unified thickness scale is set in [55] in order to facilitate comparison.

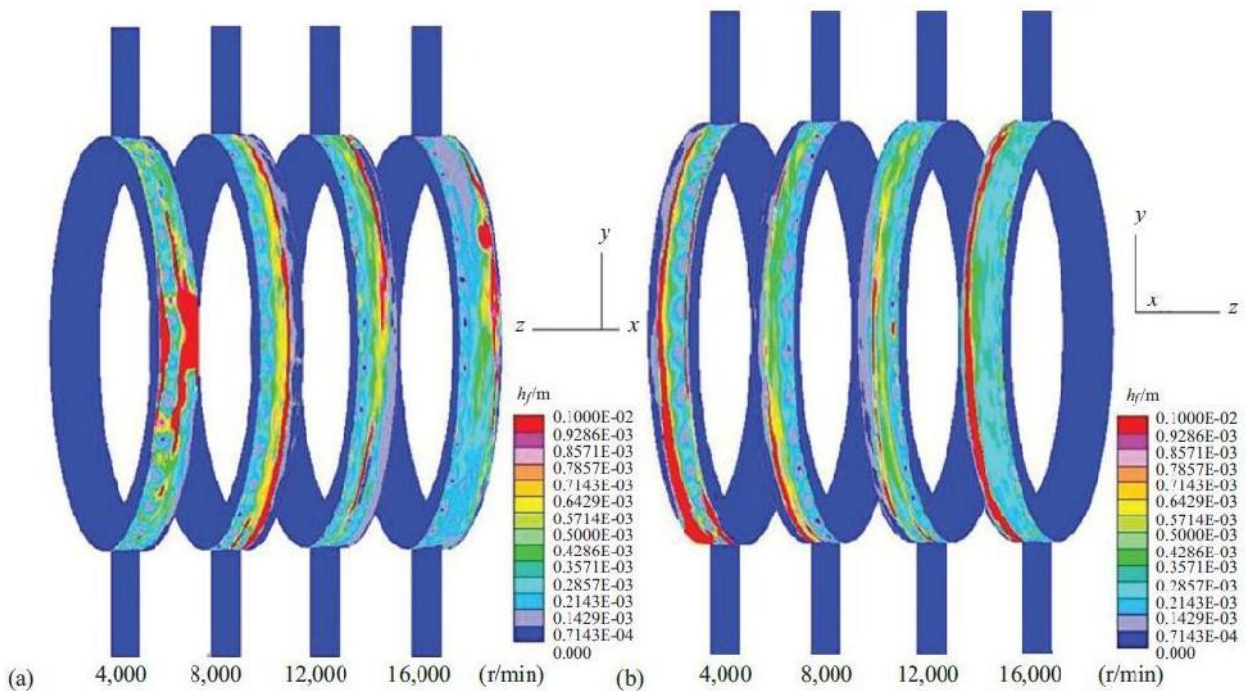


Figure 3.21. Oil film thickness contours at different rotation speeds.

(a) $0^\circ < \alpha < 180^\circ$; (b) $180^\circ < \alpha < 360^\circ$

As can be seen from the figure, firstly, the distribution of the oil film in the stable state is inhomogeneous, whether it is in the circumferential or axial direction mainly because the air shear force, gravity and the droplet impulse increment in different positions have different

effects on the oil film motion and formation. Secondly, the total mass of the oil film distribution on the bearing chamber wall shows a trend of decreasing with the increase of rotation speed, namely the effect of oil return becomes better and better. Main reason is that the air shear force becomes stronger with the increase of rotation speed, resulting in the ability that the air shear force drags the oil out of the vent and scavenges port becomes stronger also.

From the viewpoint of a CFD numerical simulation, the thin film is usually treated as a coupled boundary condition for the core air flow. However, the underlying assumptions built in the various thin film models available in the literature need to be borne in mind as, while they can facilitate the formulation of the governing equations and their numerical computation, they also limit the situations to which the models can be applied. Rourke and Amsden designed a popular (as used in the codes KIVA and ANSYS-FLUENT, for example) thin film model for port-injected engines, whereby the Lagrangian trajectory of the oil is maintained. An oil film height is computed as the ratio between the volume of the droplets found in any given wall cell and the cell area [4, 56, 57].

A first attempt at bearing chamber applications by the Nottingham team [31] oversaw the formulation of an Eulerian model and provided a first tailored CFD solution to the bearing chamber problem, albeit in a sequential manner. More recently Williams [58] investigated the impact of droplets on idealised films. [4]

If the oil film flow is treated as Newtonian, incompressible and isothermal with film velocity and pressure, then in general coordinates the flow is governed by continuity equation [4]

$$\nabla \cdot u_f = 0$$

and Navier-Stokes equations

$$\rho_f \frac{Du_f}{Dt} = -\nabla p_f + \rho_f g + \mu_f \nabla \cdot \nabla u_f,$$

where ρ_f and μ_f are the oil density and viscosity respectively; g is the acceleration due to gravity.

Depth averaged momentum equation can be obtained as [4]:

$$C_\zeta = E_\zeta + G_\zeta + A_\zeta + W_\zeta + D_\zeta + V_\zeta + S_\zeta,$$

where C_ζ - convection of film, E_ζ - variation of velocity profile within the film; G_ζ - gravity; A_ζ - air-film interaction (including pressure and shear stress); W_ζ - Shear stress from wall; D_ζ - droplet-film interaction; V_ζ - flow crossing the wall surface; S_ζ - surface tension.

An ideal formulation for thin-film flows has been presented and successfully applied to the numerical simulation of smooth, shock and pool type solutions in [34]. In this formulation, gravity, viscous, pressure gradient and surface tension forces are accounted for and an accurate inertia representation is recovered using corrective source terms. Solutions strategies that rely on using large surface tension values to guarantee stability have been investigated and shown to introduce significant artificial smoothing to the final solution especially in the case of pool solutions. A practical solution strategy for thin-film flows rimming flow subjected to physical constraints (engineering fluids) has been proposed and

requires sufficient grid refinement to resolve key flow features, as well as progressive relaxation of the surface tension from large stabilising values (used to obtain a quick initial solution) to smaller values that are within physical limits.

To undertake an optimum engineering design of systems involving thin-film flows, engineers require reliable numerical tools with which to analyze these thin-film rimming flows and associated heat transfer processes. A constraint of general numerical approaches, such as adopted within Computational Fluid Dynamics (CFD) codes is the often significant disparity in typical length scales across the domain. In this context, the numerical simulation of thin-film flows poses a particular engineering challenge due to the high computational cost that would be required to resolve the film when using more conventional multi-phase flow methods, such as the volume of fluid (VOF) approach, which are suitable for the other larger scale flows within the same system. In order to address this challenge, a number of previous numerical studies of thin-film rimming flows.

The main variables driving the dynamics of the problem and which ultimately determine the steady state flow regime include:

- the volume fraction of liquid or filling fraction;
- physical properties of the liquid such as dynamic viscosity, density and surface tension;
- the mean interfacial shear stress driving the film;
- the gravitational acceleration. [34]

The resulting film flow dynamics over the solid-substrate may be described by the depth averaged continuity and momentum equations [35] given by

$$\frac{\partial h}{\partial t} + \frac{\partial q}{\partial s} = 0$$

$$\frac{\partial q}{\partial t} + \frac{\partial}{\partial s} \int_0^h u^2 dy = - \frac{h}{\dots_l} \frac{\partial P_l}{\partial s} + \frac{h}{\dots_l} \frac{\partial \tau k}{\partial s} + g_s h + S_\tau,$$

where $p_l = (p_g - \rho g_y h)$, is the film pressure which has a component from the interfacial gas pressure, P_{gas} , and the film hydrostatic pressure, $\rho g_y h$. p_l is used to compute the film hydrostatic pressure gradient term, which is the first term on the right hand side (R.H.S.).

Surface tension effects are represented in the surface tension term is estimated according to

$$k = \frac{\frac{d^2 h}{ds^2}}{\left(1 + \left(\frac{dh}{ds}\right)^2\right)^{1.5}}$$

The correct representation of the inertia term is therefore key to the development of a robust thin-film formulation. "Simplified inertia" approximation would only be valid for uniform film profiles, which are unrealistic under conditions of a strong driving shear at the film interface with a no-slip wall condition. The implications of this inertia simplification on the stability of thin-film solutions therefore need to be verified. In this study, rather than assume a uniform

film velocity profile, a more general quadratic film velocity profile is assumed. The inertia term is then modelled as being composed of a simplified inertia component and a correction source term to recover a “full inertia” representation given by

$$\frac{\partial}{\partial s} \int_0^h u^2 dy = \frac{\partial \overline{huu}}{\partial s} + \frac{\partial}{\partial s} \int_0^h u^{\wedge 2} dy$$

An assessment of implicit, semi-implicit and explicit time schemes has revealed that the use of semi-implicit and explicit schemes leads to numerical instability as well as a considerable increase in the overall computational cost due to the very low Courant numbers required to ensure numerical stability. It is therefore recommended that in addition to ensuring sufficient grid resolution and accurate inertia representation, the thin-film equations be solved with a fully-implicit time scheme in order to guarantee numerical stability and reduce computational cost. [34]

An Eulerian thin-film model (ETFM) has been successfully coupled with a steady state Finite Volume solution of the single phase vapour flow above a film in order to simulate the thin-film flow over a rotating plate. For uni-directional flows with no vertical velocity component normal to the wall and smooth film profiles, the ETFM with a simplified inertia formulation offers a computationally efficient simulation approach. It allows for the use of coarser numerical meshes without the need to resolve film thickness with the grid leading to considerable computational savings. Comparison of thin-film predictions against experimental data have shown that the ETFM model gives a comparable accuracy to the more computationally expensive 2D axisymmetric VOF CFD calculations. [59]

Fig. 3.22 shows the steady state film-thickness distribution on the plate. The solutions predicted are characterized by smooth film profiles with gradual changes in film thickness. The overall maximum film thickness is shown to decrease with increasing plate rotational speed due to increased centrifugal force acting on the film.

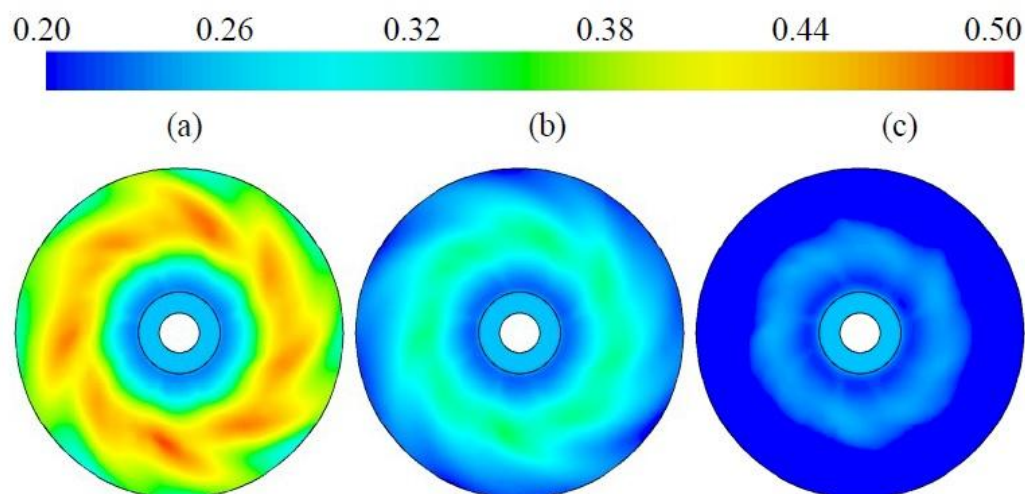


Figure 3.22. Steady state thin-film thickness profiles (in mm) for a 15LPM film flux and varying rotational speeds of; (a) 50 RPM in case 1b, (b) 100 RPM in case 2b, (c) 200 RPM in case 3b

The paper [60] presents a coupled ETFM-VOF framework for the numerical simulation of multi-scale thin liquid films. A depth averaged Eulerian thin-film model (ETFM) is used to simulate the oil flow in very thin-film regions where film thicknesses are below the grid resolution while elsewhere in the domain where grid resolution is sufficient to resolve the film, a traditional. Volume-of-Fluid (VOF) approach is retained. The two approaches are coupled through momentum and mass conserving source terms and a transition criterion is introduced where the total liquid volume fraction in each cell is evaluated and either the ETFM or VOF approach used depending on the sufficiency of the local grid resolution. The model builds upon currently available ETFM and VOF approaches to thin-film modeling and represents a novel approach to the numerical simulation of multiphase flows involving a varying range of film thickness scales in space and time.

VOF and ETFM modelling capabilities available in commercial CFD code ANSYS FLUENT version 16 have been coupled using a User Defined Function (UDF) developed by the authors to facilitate the multi-scale simulation of thin-film flows. The resulting coupled non-isothermal VOF-ETFM formulation is summarized in equations 3.1-3.3 for the VOF regions and equation 3.4-3.5 for the ETFM regions with coupling source terms. [60]

$$\frac{\partial r_1}{\partial t} + \frac{\partial}{\partial x_j} (r_i u_j) = S_{m-VOF} \quad (3.1)$$

$$\begin{aligned} \frac{\partial}{\partial t} (\dots_m u_i) + \frac{\partial}{\partial x_j} (\dots_m u_i u_j) = & -\frac{\partial \dots}{\partial x_i} + \dots_m \frac{\partial^2 u_i}{\partial x_j x_j} + \dots_m g_j + \\ & + S_{MOM-VOF,j} \end{aligned} \quad (3.2)$$

$$\frac{\partial T}{\partial t} + \frac{\partial}{\partial x_j} (\dots_m T u_j) = \left(\frac{k_m}{\dots_m C_{p,m}} \right) \frac{\partial^2 T}{\partial x_j x_j} + S_{T-VOF,j} \quad (3.3)$$

$$\frac{\partial h}{\partial t} + \frac{\partial q_j}{\partial x_j} = S_{m-ETFM} \quad (3.4)$$

$$\begin{aligned} \frac{\partial q_j}{\partial t} + \frac{\partial}{\partial x_j} \int_0^h u_i u_j dy = & -\frac{h}{\dots_f} \frac{\partial \dots_f}{\partial x_j} + \frac{h}{\dots_f} \frac{\partial \dagger k_j}{\partial x_j} + g_j h + \\ & + S_{\dagger,j} + S_{MOM-ETFM,j} \end{aligned} \quad (3.5)$$

where S_{m-VOF} and S_{m-ETFM} , are the mass transfer source terms for the VOF domain and the ETFM domain respectively; $S_{MOM-VOF,j}$ and $S_{MOM-ETFM,j}$ are the VOF and ETFM momentum transfer source terms respectively. S_{T-} , and S_{T-ETFM} are the energy transfer source term for the VOF and ETFM domains respectively. These source terms are jointly used to couple the VOF domain with the ETFM domain and effect a transition from one to another through conservative mass, momentum and energy transfer between the two domains based on a given transition criteria.

The coarse grid is used to simulate the rimming flow using a coupled ETFM-VOF approach. Contours of the total liquid volume fraction are shown in Fig. 3.23a for the stationary outer

wall. The corresponding film thickness from the ETFM model in these regions is shown in Fig. 3.23b.

During the simulation, some cells were transitioned from ETFM to VOF representations and vice-versa depending on the local volume fraction of liquid in the cell. The ETFM-VOF simulations were run on a cluster with Intel Xeon E5-2670 processors and required approximately 6,650 CPU Hours for each second of flow simulated. The ETFM-VOF solution is shown to provide a considerable saving in computational costs due to the relaxed grid resolution requirements. In addition, no artificial dry-out of the film is predicted as even very low liquid volume fractions may be accounted for using the ETFM approach where they are below the VOF threshold. [60]

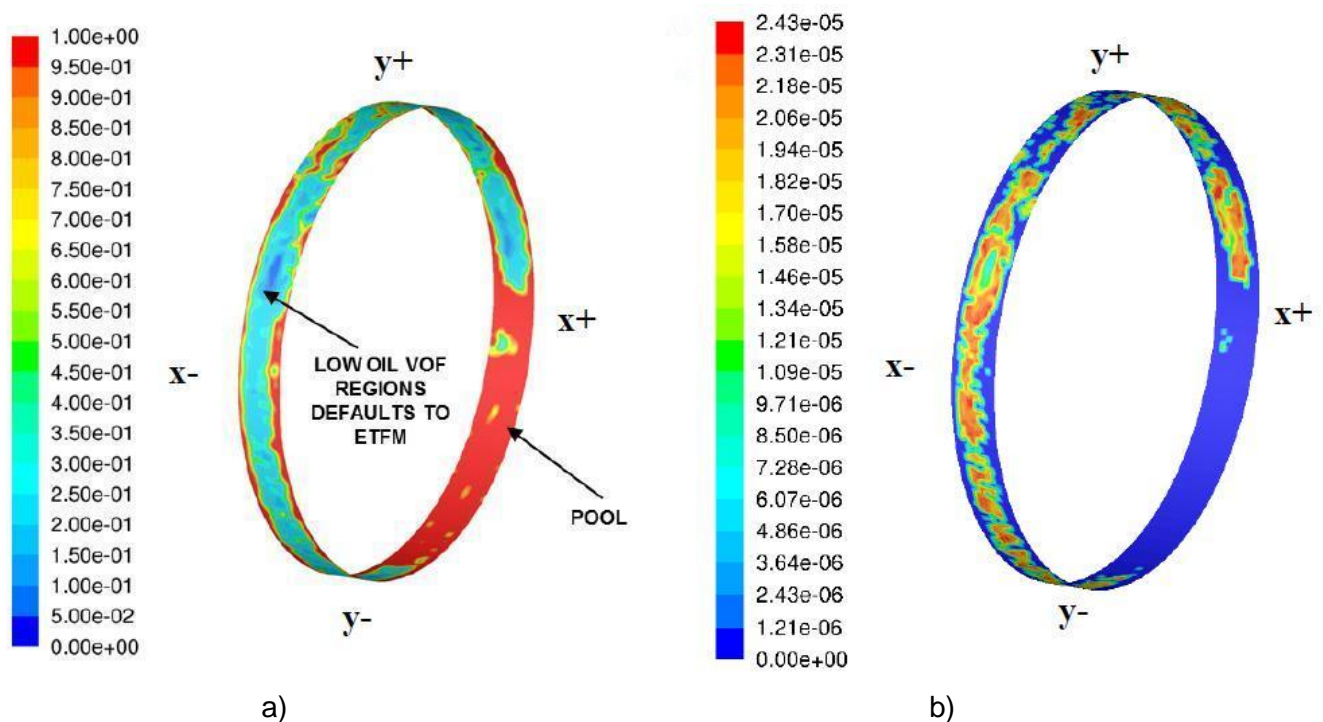


Figure 3.23. Contours of total liquid volume fraction for the coupled ETFM-VOF simulation (a) and film thickness (m) in the ETFM region for the coupled ETFM-VOF simulation (b)

In work [61] is looked at a detailed computational fluid dynamics (CFD) simulation of one of the inserts that performed well. This aids understanding of the flow characteristics of using an insert to improve oil residence in a bearing chamber. The CFD geometry and mesh are shown at the Fig. 3.24.

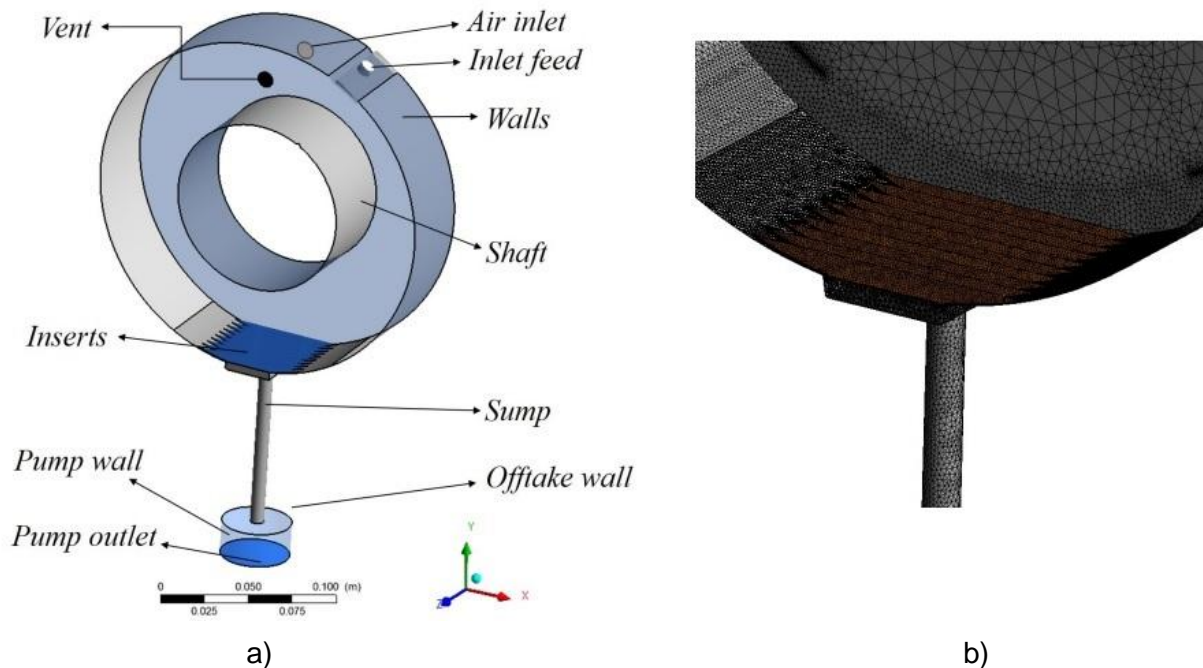


Figure 3.24. CFD geometry for the domain (a) and computational mesh (b)

Fig. 3.25. shows that the hydraulic jumps do not extend chamber wide. The 3D air windage drives the film to the side walls creating a thinner layer of film towards the middle.

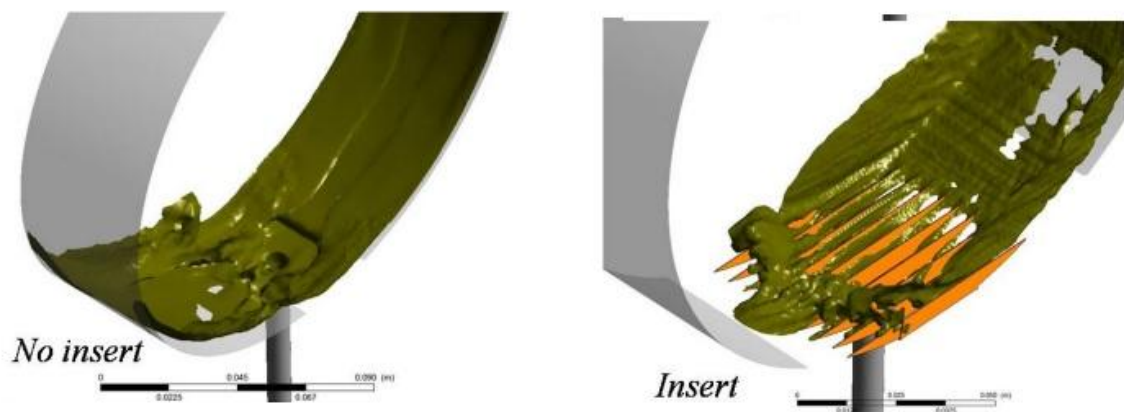


Figure 3.25. 3D film structure in the sump

The insert creates some damping effect. Thus the film tends to slow down faster inside the sump compared with the one without the insert. There is less ingestion of air into the offtake pipe. A suggestion to improve the scavenging will therefore be in the form of making short grooves on the inside of the bearing chamber outer curved wall extending from the insert. This might create less film on the outside walls and such grooves would guide the film to the sump quicker but with lower velocity. There is a bubbly ingestion of air into the offtake in both cases. Fig. 3.26 shows a higher volume of air ingestion into the offtake pipe without the insert at the instance shown. There is always water present in the gap between the sump and the insert. This means having the insert is likely going to make for a better scavenge efficiency.

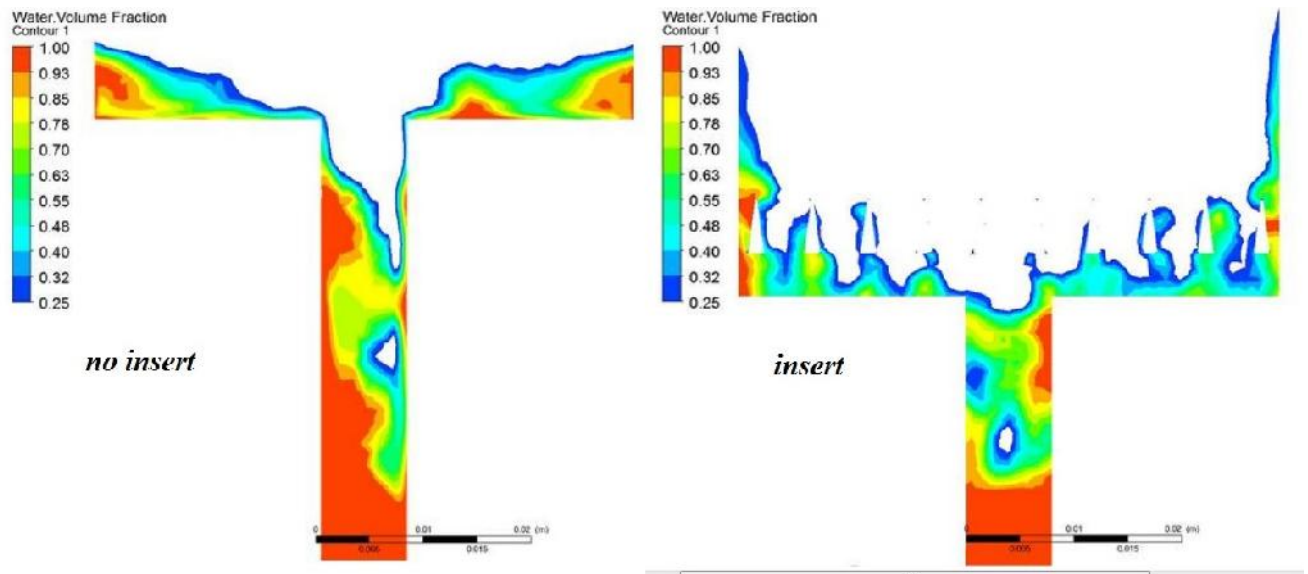


Figure 3.26. Offtake pipe air ingestion

Fig. 3.27 shows film thicknesses along the chamber wall at 105° , 135° and 160° respectively for the two cases. The angles are measured clockwise with 0° being at 12 o'clock. The film thicknesses, H_f , have been normalized as a function of the bearing chamber outer radius, R_w . The bearing chamber axial locations, Z , have been normalized with its axial width, Z_w . The results show that the film is generally about 4 times thicker without the inserts. The film thickness distribution is almost uniform in both cases.

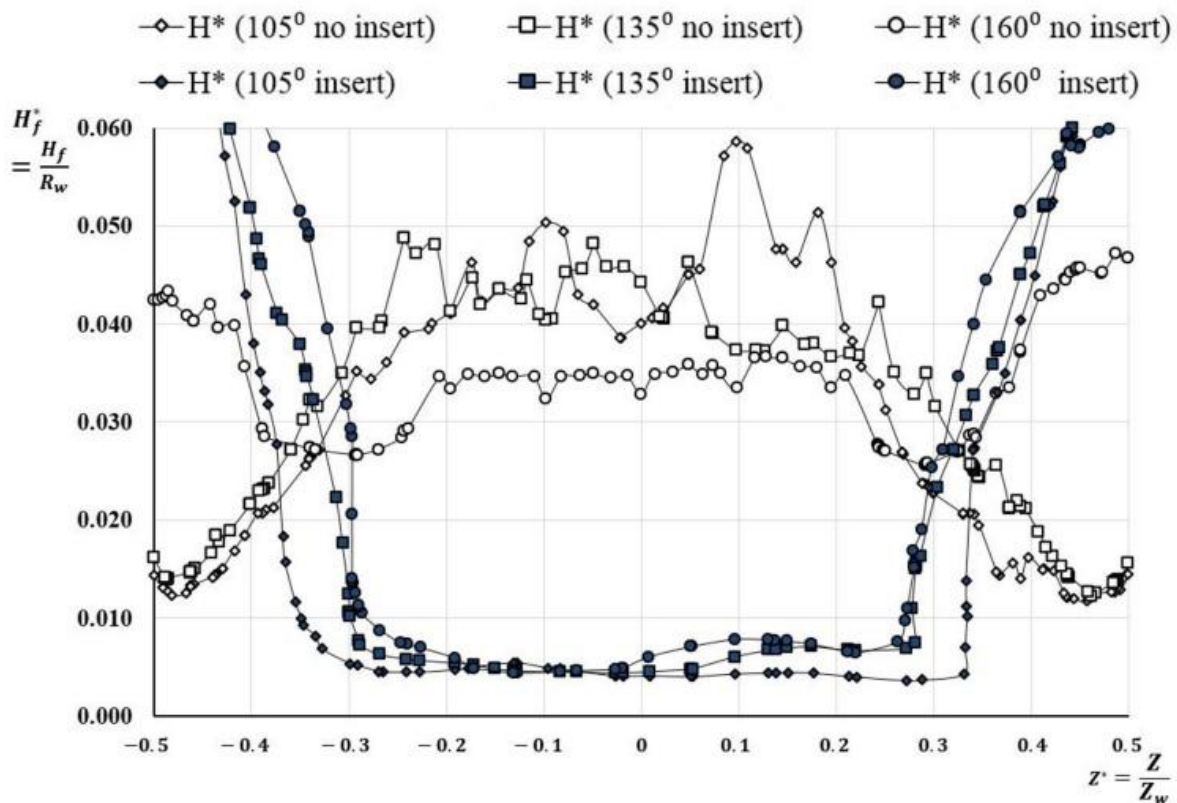


Figure 3.27. Film thicknesses

The simulations [61] suggest that the residence volume is higher for the baseline geometry than for the modified sump, contrary to what was found in the experiment. With the “dry patches” seen on the outer walls of the bearing chamber, it is very likely that there has been mass loss as result of the inability of the VOF model to capture very thin film unless the mesh is “fine” enough. This is a possible reason for the discrepancies in the residence volumes compared with the experiment.

The interaction of two fluids with very different densities makes bearing chamber design challenging, as the oil distribution and split between scavenge and vent pipes can vary significantly when the operating conditions change. CFD simulations can enhance the predictive capabilities of bearing chamber design, and provide an unprecedented insight into the flow dynamics taking place during engine operation. Among the simulation techniques available, the VOF method has been applied multiple times on bearing chamber flows [62]. The damping function adopted in it work is the one proposed by Egorov [63], who was the first to introduce a wall-like turbulence damping at the gas-liquid interface of shear-driven flows, for a two-fluid method. The turbulence damping approach followed by Egorov modifies the \tilde{S} equation of the $k-\tilde{S}$ turbulence model to introduce a solid wall-like damping at the gas-liquid interface. This modification was developed and tested for a stratified, smooth, shear-driven liquid flow in a rectangular channel. It was later made available by Tkaczyk et al. [64] in the VOF method and further tested on stratified channel flows [62].

The geometry adopted in this study represents the baseline configuration of the experimental bearing chamber reported in the work of Kurz et al. [9]. The chamber has a rectangular cross-section and cylindrical vent and scavenge pipes of the same diameter located on its centerline. The computational grid is a structured multi-block mesh made with

ANSYS ICEM. The mesh has 2.7×10^6 hexahedral elements. To ensure sufficient resolution in the region where the oil film thickness is measured, the height of the first cells layer on the chamber outer wall is of the order of $50 \mu\text{m}$.

The results of calculation show that oil re-distributes starting from a thin film covering the front half of the chamber ('smooth' solution, Fig. 3.28a) to a large, unsteady thick film region in the rising side of the cylinder ('pool' solution, Fig. 3.28b). Contours of Oil Film Surface Velocities is presented in Fig. 3.29.

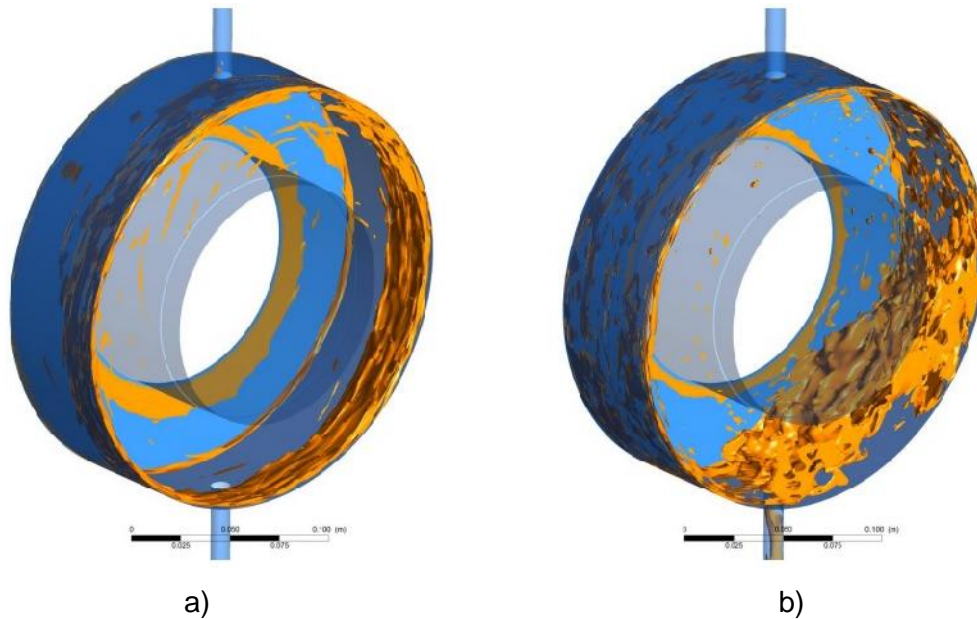


Figure 3.28. Effect of Turbulence Damping on Oil Film Distribution. Contours of Iso-Surfaces of $\Gamma_0 = 0.5$: (a) $t/\tau = 44.7$; (b) $t/\tau = 138.3$

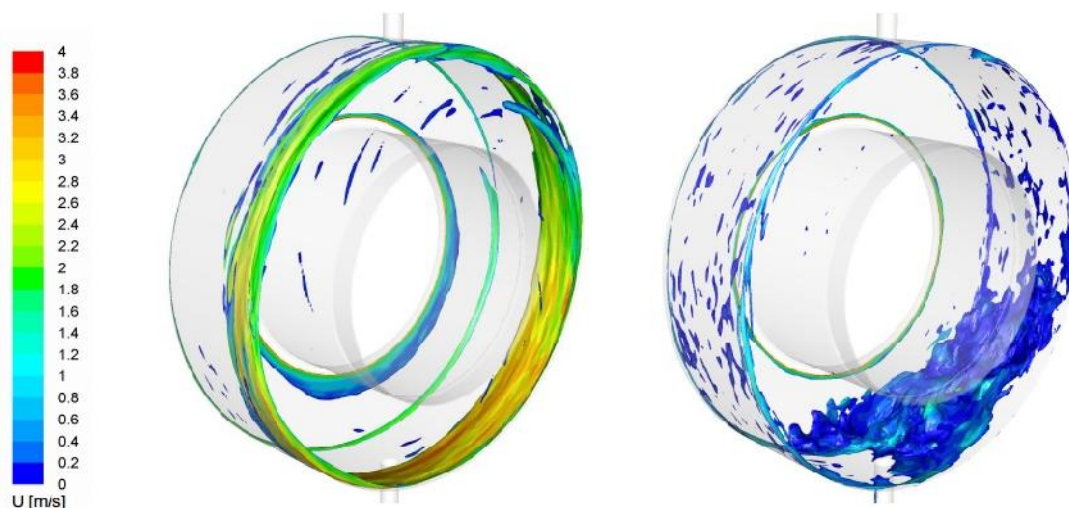


Figure 3.29. Contours of Oil Film Surface Velocities at $\Gamma_0 = 0.5$, Time-Averaged over 0.1 s

Contours of Oil Film Surface Velocities is presented in Fig. 3.29. The contour plots of Fig. 3.29 give a further insight in the spatial distribution of the time-averaged film surface velocities. Consistently with the relatively low reference film speeds has maximum film velocities of the order of 1 m/s (Fig. 29(b)) while values up to 3 m/s are found in case Fig. 29(a).

In paper [65] is shown that for a deeper insight into the oil wall film formation, the application of local Adaptive Mesh Refinement (AMR) is required. The coupling of the Volume-of-Fluid method for wall film modelling and an Euler-Lagrange technique for droplet tracking in combination with a droplet-wall film interaction model could be a promising approach to provide a numerical method for the modelling of complex two-phase flow phenomena in an aero engine bearing chamber. If the mesh resolution can be kept fine enough to resolve the film with VoF-AMR, but coarse enough for droplet tracking via Euler-Lagrange, this approach can be seen as well-balanced between computational effort and solution accuracy.

Fig. 3.30 shows influence of mesh size on simulation oil film.



Figure 3.30. Influence of mesh size on the prediction of oil wall film development at $n_{sh}=5,000$ pm. (Case A – 621500 cell, Case C – 170000 cell, Case F – variable)

For case A (Fig. 3.30a), the oil film is rather smeared over the chamber walls due to insufficient grid resolution in tangential direction. Fig. 3.30c shows the influence of a local AMR (case F) based on the gradient of the volume fraction of the liquid phase. Here, a completely different wall film structure occurs. On the one hand, smaller flow features such as oil droplets, ligament shedding and film waves are predicted due to the much smaller cell size, leading to a mesh size of around $N_{cell}=7,000,000$. On the other hand, however, the wetting of the chamber walls differs from the ones observed in cases A and C, considerably. A reason for this behaviour might be the solver settings necessary for the adaptive mesh refinement.

Considering case A with an average time step of $\Delta t = 1.41e-5$ s, the computational effort or calculating a physical flow time of $t = 1$ s equals to 1,500 CPUh/s which corresponds to 48 time steps per CPUh. Increasing the mesh size globally for case B, the computational costs are increased to 4,000 CPUh/s, corresponding to 16 time steps per CPUh with an average time step of $\Delta t = 1.48e-5$ s. The application of local AMR increases mesh size, up to

$N_{\text{cell}}=7,000,000$ and computational costs considerably up to 63,000 CPUh/s, corresponding to 5 time steps per CPUh with an average time step of $\Delta t = 3.25e-6$ s. [65]

In work [39], the use of the Compressive Interface Reconstruction scheme with bounded second order implicit time discretization has enabled a significant speed-up of the simulation times against the previously adopted explicit Geometric-Reconstruction scheme. The use of the Compressive Interface Reconstruction approach, coupled with the bounded second order implicit transient formulation, enabled to achieve a stationary-state inside the bearing chamber, hence a condition in which given reference flow parameters oscillate around a constant mean value. In this case, the parameter considered was the oil residence volume inside the bearing chamber annulus, i.e. excluding the vent and scavenge pipes. The mesh for this baseline case had 2.7 million cells, with a corresponding time step size of 10^{-5} seconds. Starting from an initialization with a 0.5 mm oil film on the outer and bearing-side walls, the stationary-state was reached after about 2.2 seconds of flow time, as reported in Fig. 3.40a.

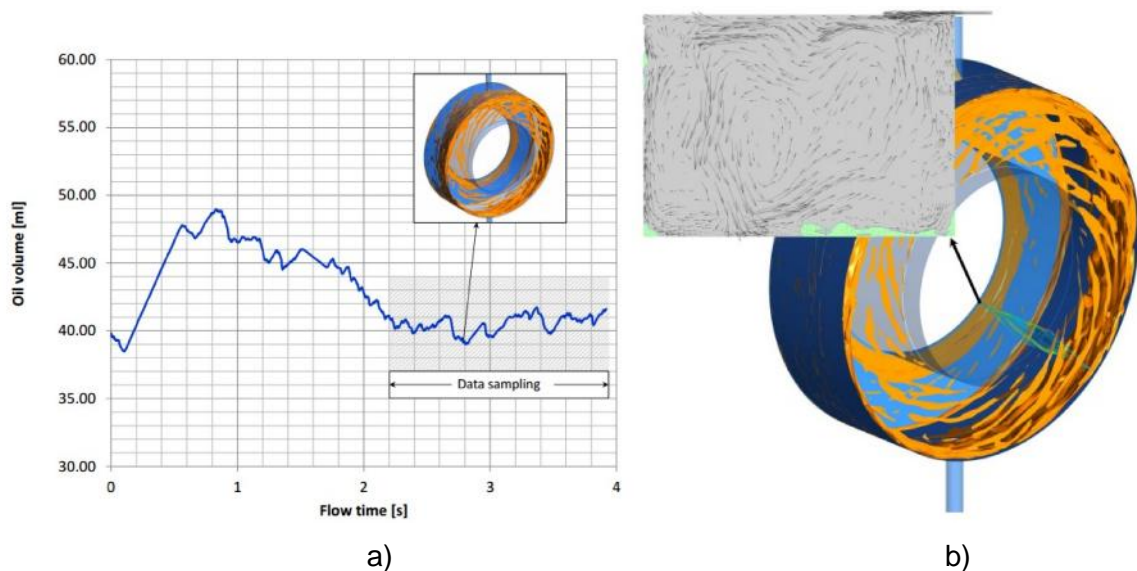


Figure 3.40. Time evolution of residence oil volume, baseline case (a) and Iso-surface of oil volume fraction (b)

Air flow field tends to push the oil towards the air inlet (or "front") side of the chamber. This is clearly visible in Fig. 3.40b, which shows an accumulation of oil consistently with the velocity vectors of the secondary air flow. This result, however, was not consistent with the secondary vortices calculated in the air-only simulations.

The results [39] have shown a tendency of the model to underpredict the oil film thickness on the bearing chamber outer wall, with the oil accumulating on the air inlet side. Oil tends to entrain with the vent air flow in a higher proportion than the experimental observations, thus giving an under-prediction of the bearing chamber scavenge efficiency. Further mesh refinement in the oil film regions did not give an improvement of the results. Future improvements to the modelling strategy include a better understanding of the effects of Turbulence Damping on the liquid flow structure.

A temporal evolution of the crown's breakup is depicted in the Fig. 3.41 using the isosurface of the volume fraction at $\alpha = 0.5$ viewed from two different perspectives. When the single drop touches the liquid surface with a point contact, capillary waves are induced by the numerical method. These capillary waves travel upwards along the impinging drop and flow along the fast expanding ejecta. [51]

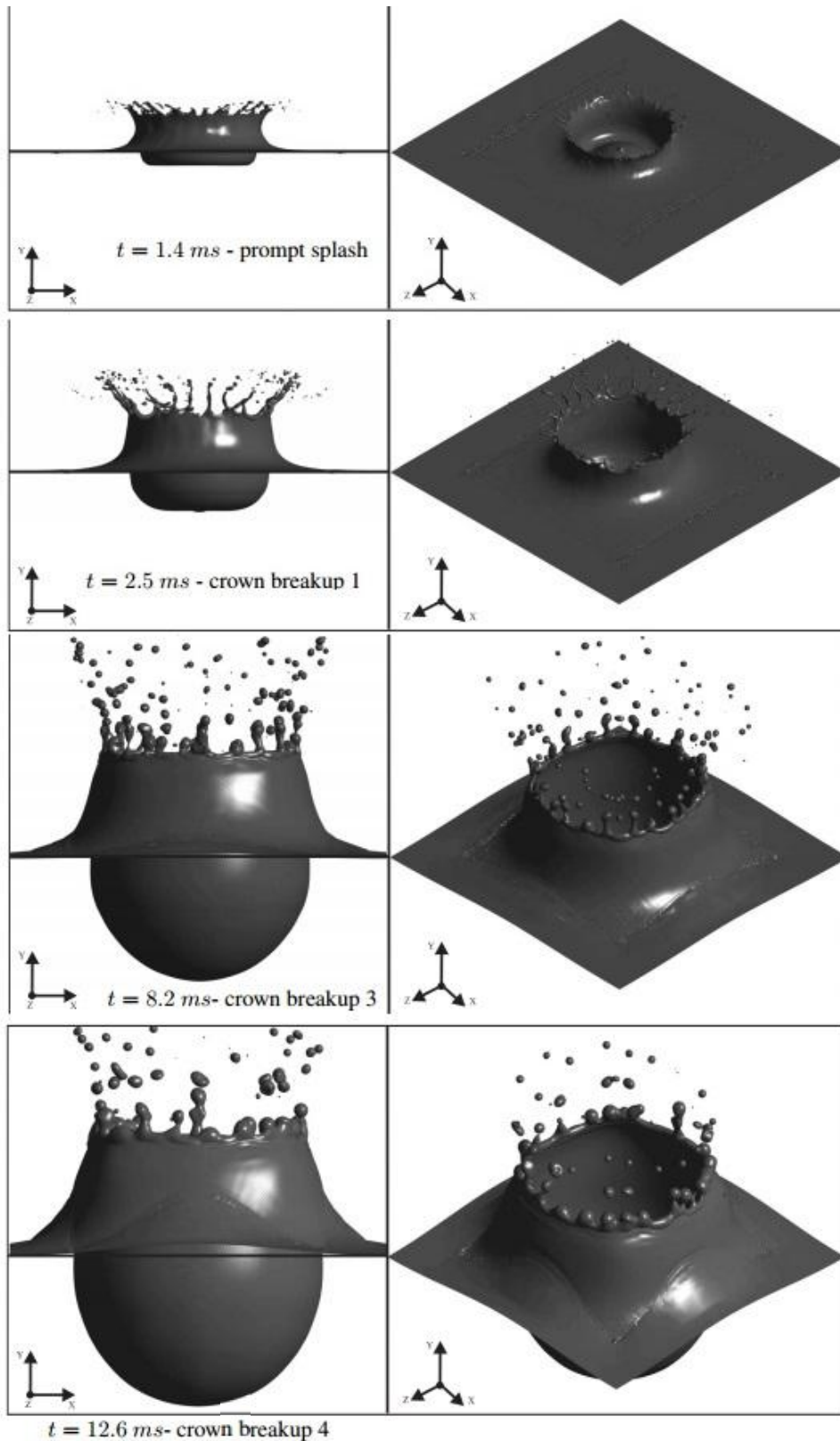


Figure 3.41. Iso-surface of $\alpha \approx 0.5$ showing different stages of the crown's breakup during drop impact on a liquid layer ($We=2209$, $Oh=0.0031$)

The build-up of pressure caused by the enhanced surface tension forces at the edge of the elongated finger-like jets is well shown in Fig. 3.42. In this figure, the iso-surface of the volume fraction at $\alpha \approx 0.5$ is coloured by the calculated static pressure contours.

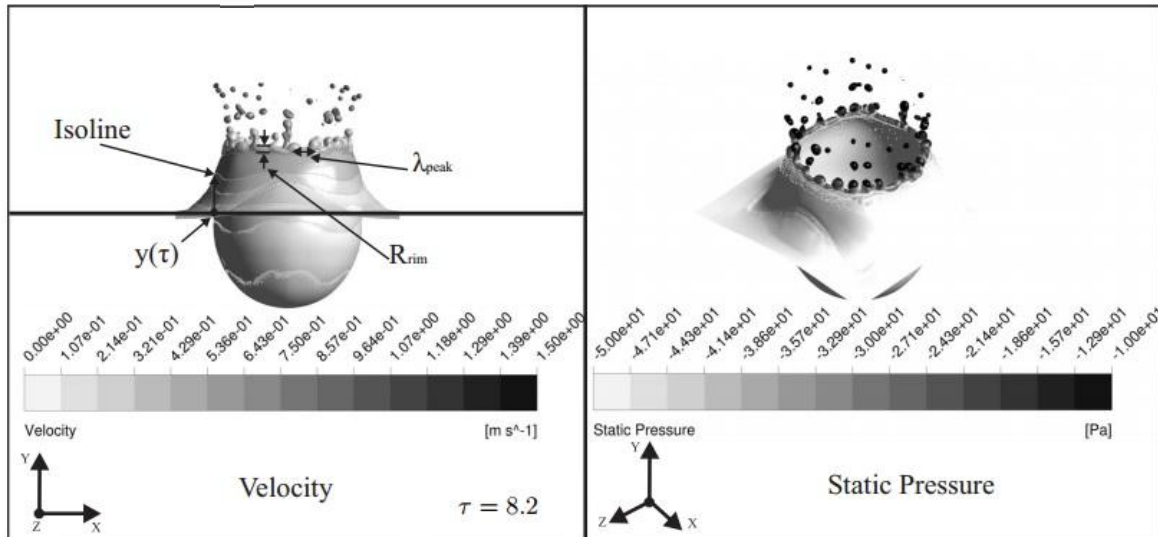


Figure 3.42. Iso-surface of $\alpha \approx 0.5$ coloured by the static pressure and absolute velocity during a crown's breakup: $We=2209$, $Oh=0.0031$, and $Fr=343$

Fig. 3.43 shows the effect of the Weber number for three different crown disintegration stages, namely $\tau = 2.3$ and $\tau = 5.2$.

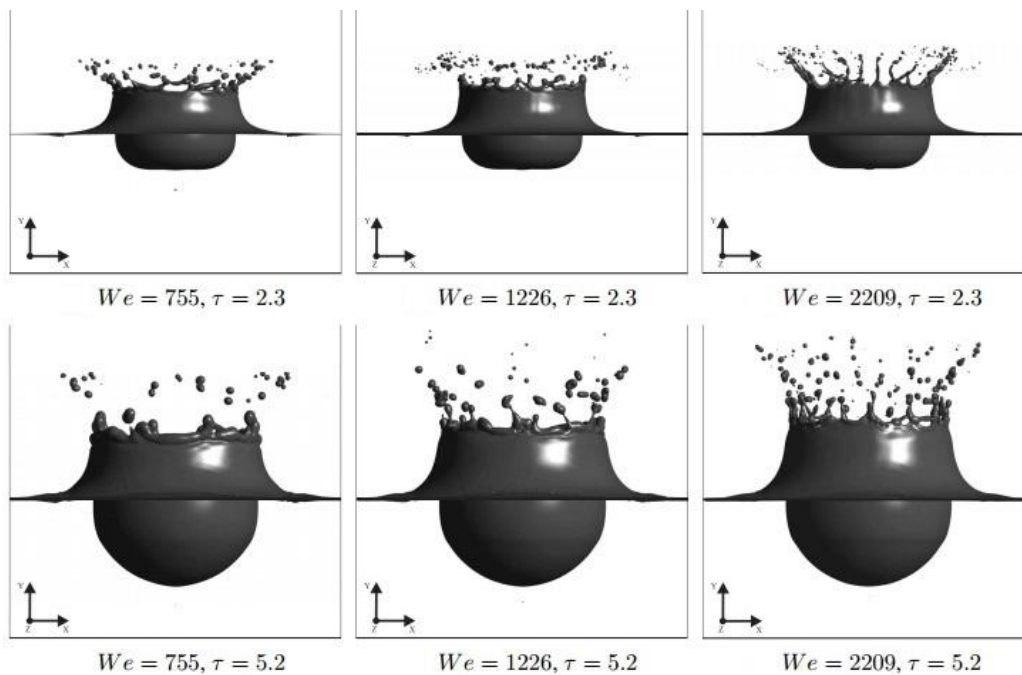


Figure 3.43. Qualitative depiction of the Weber number influence on the crown's breakup process during single drop impingement onto liquid surfaces

An increase of the impinging Weber number results in an enhanced dominance of the kinetic energy over the surface tension energy. This, in turn, may indicate that fewer forces are available during the impingement to act against the additional surface generation, thereby making the release of secondary drops easier.

Fig. 3.44 shows the effect of three different impinging Froude numbers on the crown's breakup dynamics for a constant impinging K number of $K = 8565$ in two different breakup stages: $\tau = 2.3$ and $\tau = 5.2$.

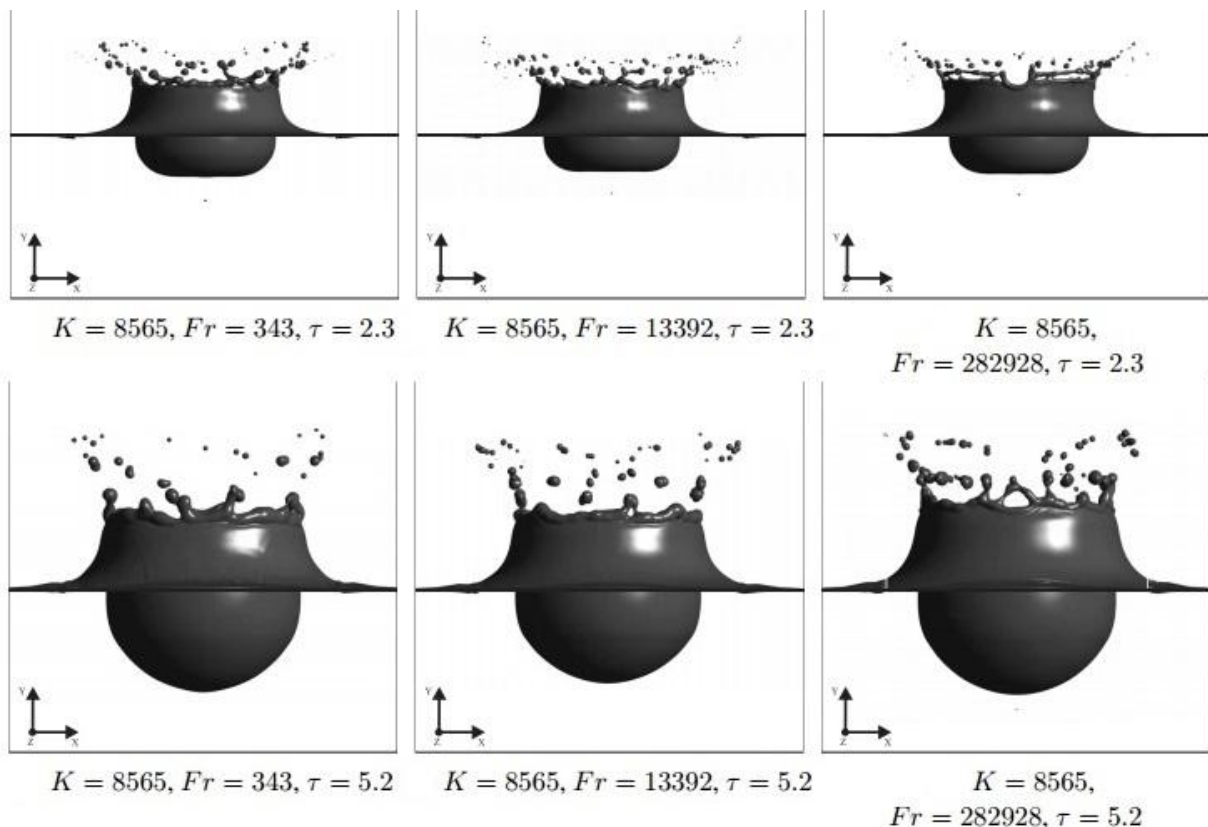


Figure 3.44. Qualitative depiction of the influence of the Froude number on the crown's breakup process during single drop impingement onto liquid surfaces

An enhancement of the impinging Froude number is equal to a reduction of the role of the gravitational forces that are acting against the crown's inertia. By comparing the qualitative depiction of the effect in the early stage of the impingement, at $\tau = 1.3$ and $\tau = 2.3$, larger crown heights with increasing Froude number are clearly shown. The effect becomes more evident at $\tau = 5.2$ where not only do higher crown occur, but also a reduced crown thickness for higher Froude numbers. As a result of the reduced gravitational forces, the corrugations at the crown's rim appear also to be amplified with larger Froude numbers. [51]

The effect of three different impact angles on the crown's breakup for an impinging Weber number of $We = 1850$ is depicted in a side and top view in Fig. 3.45 at different impingement times. For a better impression of the crown's breakup dynamics, iso-surfaces of the volume fraction at $\alpha = 0.5$ in the top view are additionally coloured by the y-coordinate. The drop

impact dynamics becomes more and more asymmetrical with respect to the crown's shape around the impingement point at lower angles of incidence. The visualizations are accompanied by the related pressure and velocity fields of the liquid film (see Fig. 3.46).

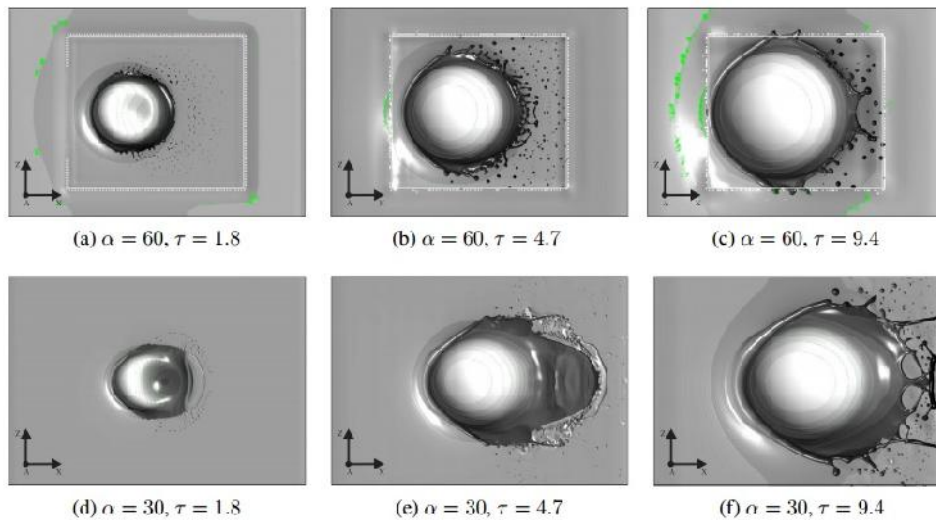


Figure 3.45. Qualitative depiction of the influence of the impact angle on the crown's breakup process during single drop impingement onto liquid surfaces from the top ($We=1850$, $Oh=0.036$, $Fr=195072$)

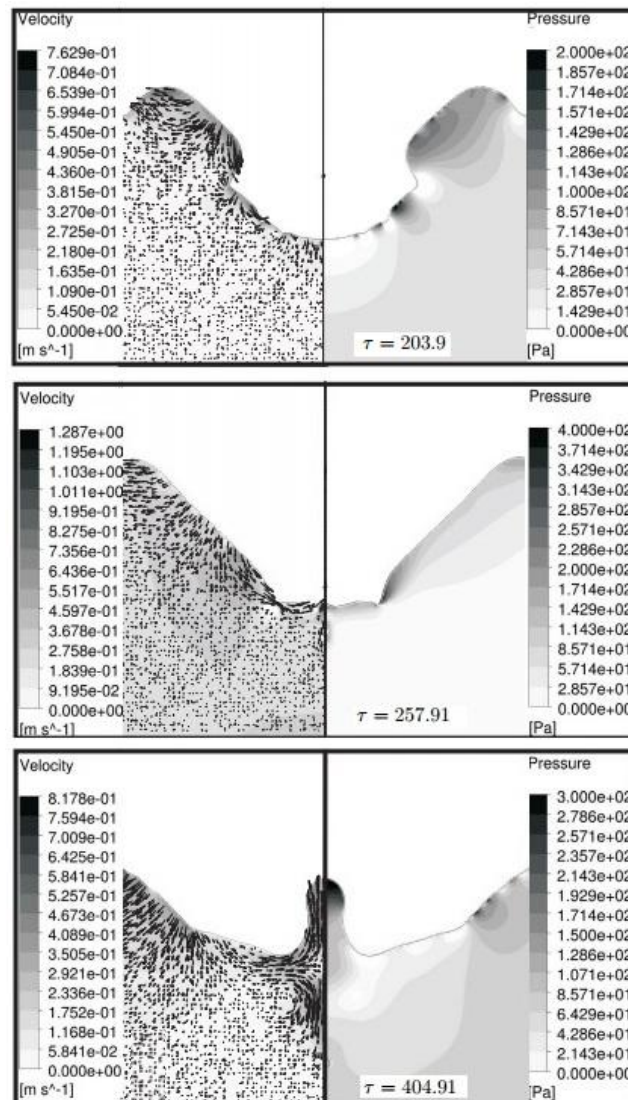


Figure 3.46. Iso-surface of $\alpha = 0.5$ showing pressure and velocity field within cavity and lamella rim during drop impact on a liquid layer: $We=541$, $Oh=0.0161$, $D=0.175$ mm and $V=15$ m/s

The capillary waves are transported further towards the bottom of the cavity by a difference in pressure occurring between the rim and the bottom of the crater. The surface tension forces cause first a change in the cavity shape from a hemisphere to a conical one, by the downward motion of the capillary waves. Then, there is formed a central jet that may pinch off some drops.

The growing potential of the multiphase CFD technique, together with increasing computational resources, has paved the way for the development of an integrated CFD multiphase modelling technique. Such a simulation tool should be capable of calculating the complete two-phase flows and heat transfer in oil systems. Despite the significant progress over the last decade in the modelling of the droplet and wall film dynamics in bearing chambers, there has still been a lack of a physical sub-model accounting for the description of the mass and momentum exchange between the impinging drops and the wall films. Drop-film interaction is known to affect the overall performance of an oil-system. [51]

A simulation of ball bearing geometrically representative of an aeroengine bearing has been conducted using a coupled level-set VOF approach for the two-phase oil-air flow [66]. The simulation assumed periodic flow as a result of the flow conditions. The contributions to pressure and viscosity from the effect of elasto-hydrodynamic lubrication were assumed negligible because of the scale of the domain relative to the contact regions, however, the loading of the bearings and effect of contact angles and ball spinning were fully considered with values chosen based on published work. In the bearing model presented, there are front and rear chambers with the rear chamber representing the space outside the bearing closest to the front (fan end) of the aeroengine.

The schematic in Fig. 3.47 shows the configuration to be modelled.

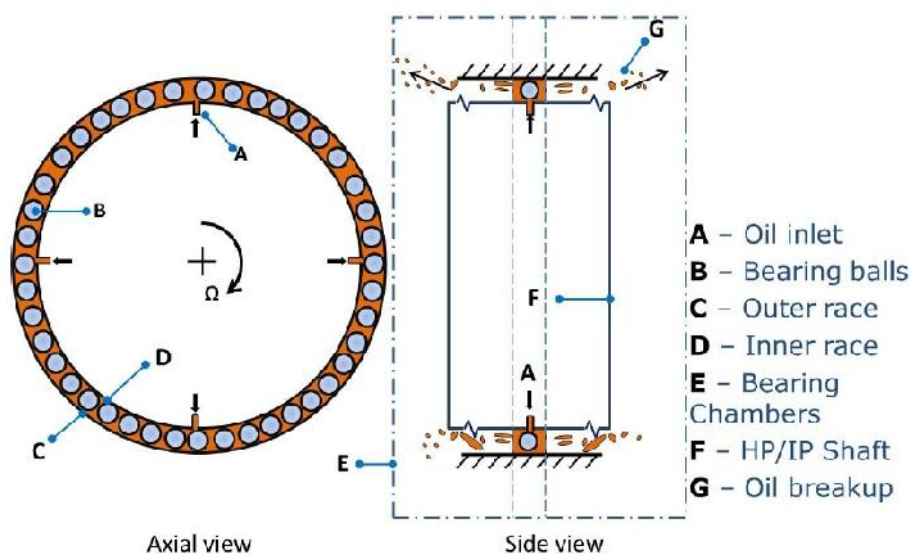


Figure 3.47. Schematic illustration of oil movement and form as it passes through the bearing

A bearing chamber houses the bearings and also serves to collect the used lubricating oil which is collected via a sump. The circulation of oil goes through a series of steps before collection at the sump. From the oil tank, the oil is fed into the bearing via the inner-race. The oil goes into the spaces between the balls and at the points of contact such as the bearing cage, the inner race, (D), and the outer race, (C). The pressure differential between the bearing chamber regions and the inlet oil pressure, the rotating shaft and the air windage from the rotating flow combine to break the oil into oil jets/ligaments and subsequently into oil droplets, (G).

Computational mesh structure is presented in Fig. 3.48. The enhanced Coupled Level Set Volume of Fluid method is used with Reynolds Averaged Navier-Stokes (RANS) equations. In the VOF technique, a colour function, Γ , based on the volume fraction of the fluids, is used to describe the multiphase mixture of oil and air. In regions with air only, the volume fraction is zero and regions completely filled with oil have a volume fraction of 1. The interface regions lie in the range $0 < \Gamma < 1$. In the Level Set technique, a smooth signed function, ϕ , is used to describe the phases of the fluids. In a two-phase system, a positive value of ϕ describes one phase. The free interface is described using an iso-surface of zero for ϕ . To model the effect of turbulence, the SST k- ω model was employed. This model includes

modifications appropriate to low Reynolds number regions as may be found in this model for films near walls [66, 67].

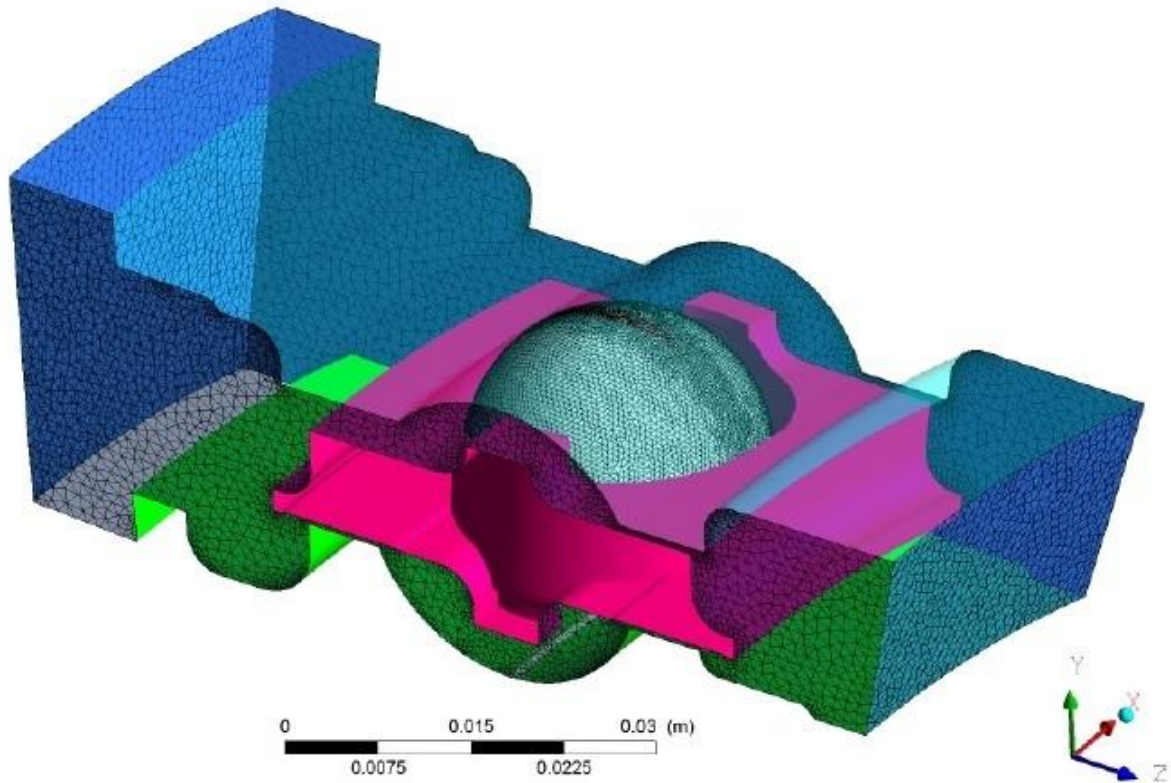


Figure 3.48. Computational mesh structure

A first order accurate explicit time integration is used for the temporal terms discretisation. The SIMPLE algorithm is used to solve the RANS equations. The convergence target for all main residuals was 10^{-4} or lower and a maximum of 50 iterations per time step were used. Simulations were carried out on 16 core processors with 16 G RAM per machine generating about 5 ms of flow time per day of computation time.

The film on the ball bearing appears to exhibit a paint roller pattern. The oil film rolls on the balls as it spins, Fig. 15. The oil exits into the front chamber as shown in Fig. 3.49, 3.50. [66]

The oil exits mostly in the form of irregularly shaped droplets and mostly through the widest gap between the cage and the outer race. Although, the sizes of the droplets have not been measured in this paper, it is clear, assuming the model to be correct, that the sizes of the oil droplets are not uniformly distributed in all cases. The oil sizes are more uniformly distributed in the 5,000 rpm cases and the 13,000 rpm cases have a very wide range of droplet sizes. The droplet population after a similar number of rotations is higher in the 5,000 rpm cases than in the 13,000 rpm cases.

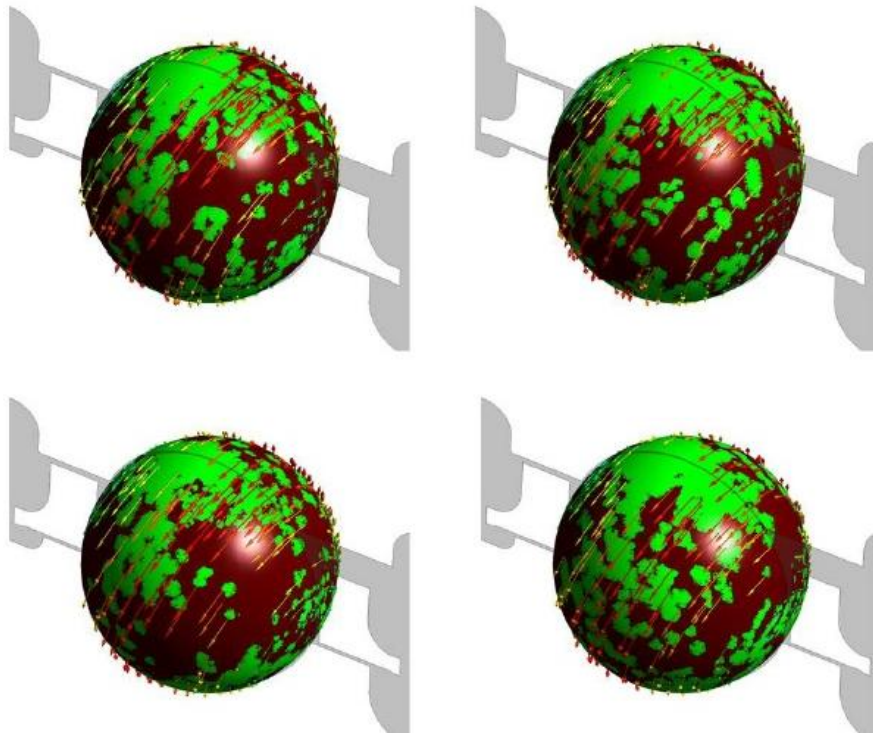
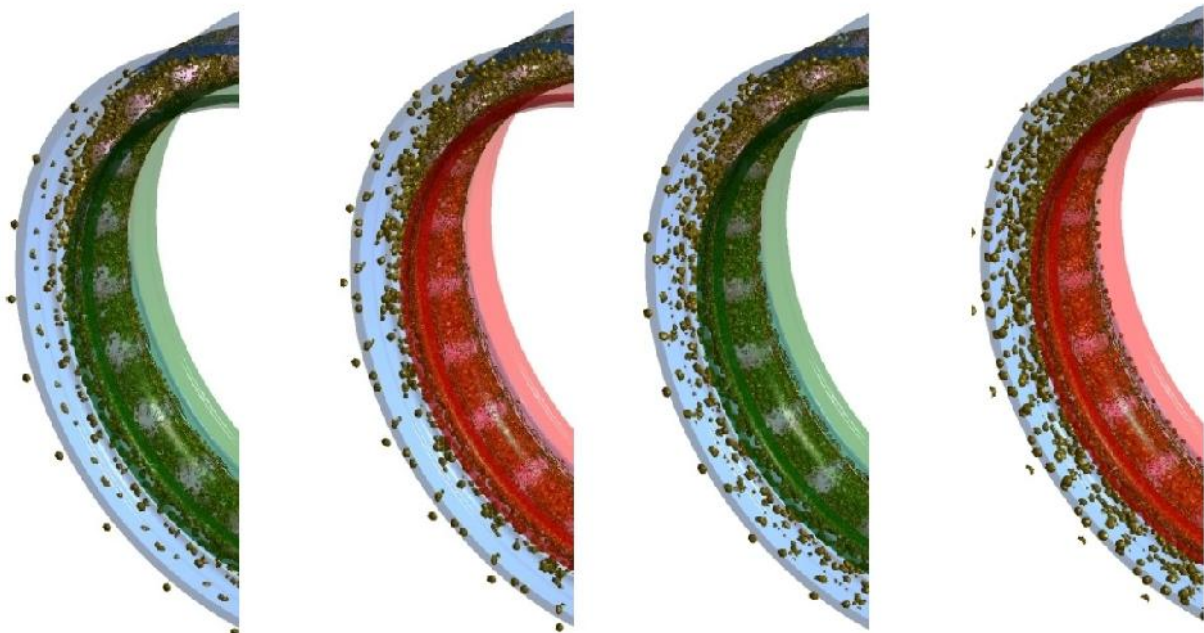


Figure 3.49. Oil rolling with the ball



(a) $\Omega_s = 13,000\text{rpm}$ $T^* = 3$

(b) $\Omega_s = 5,000\text{rpm}$ $T^* = 3$

(c) $\Omega_s = 13,000\text{rpm}$ $T^* = 5$

(d) $\Omega_s = 5,000\text{rpm}$ $T^* = 5$

Figure 3.50. Oil breakup into front chamber at 8 ltr/min

3.3 CFD modeling of Heat Transfer problems

Paper [22] establishes the heat transfer simulation model and performs numerical simulation according to the experimental conditions. The heat flux at the measurement position of the experiment is obtained, and compared with the experimental data averaged in the last one minute. Fig. 3.51 are the comparison between the simulated and experimental values of heat transfer of axial twophase flow inside and on the wall surface of the bearing chamber. Here the initial temperature of the wall is 75 degrees Celsius, the flow rate of the lubrication oil is 200L/h, and the rotation speeds are 1500r/min and 3000r/min respectively.

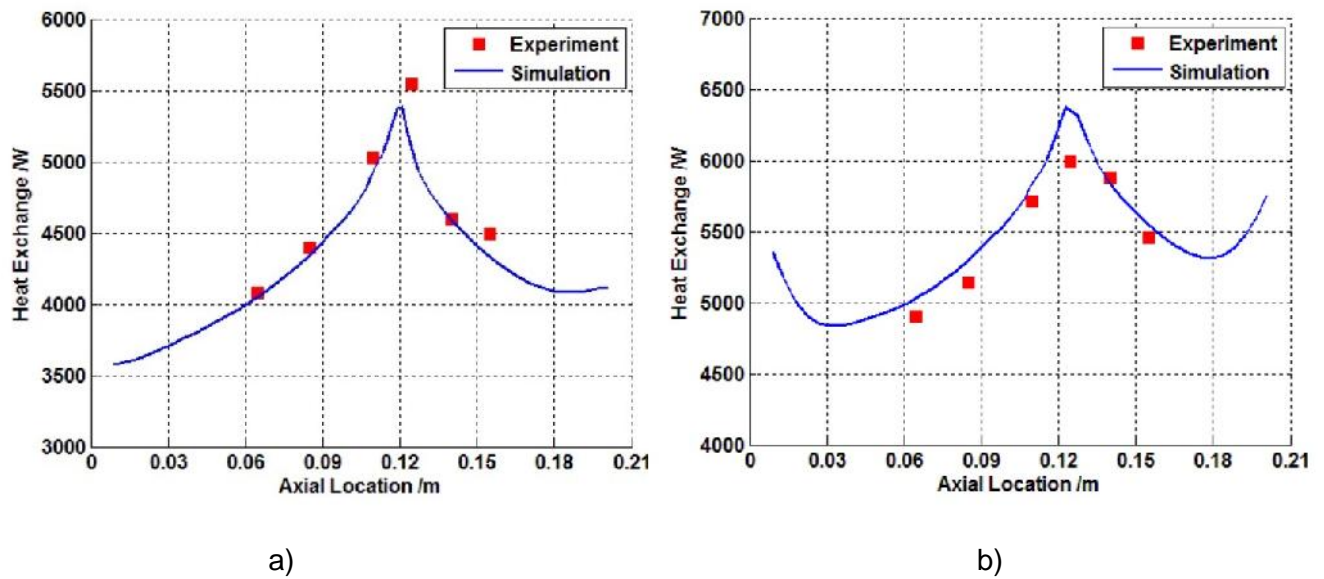


Figure 3.51. Comparison of calculated heat transfer. The flow rate is 200L/h, and the rotational speed is 1500 r/min (a). The flow rate is 200L/h, and the rotational speed is 3000 r/min (b)

According to the experimental results and the simulation results of the bearing chamber [22] Nusselt number as a function of the oil supply Reynolds number at the same rotation speed ($n=3000\text{r/min}$) is shown in Fig. 3.52. Here the oil flow rate ranges from 100 L/h to 800 L/h.

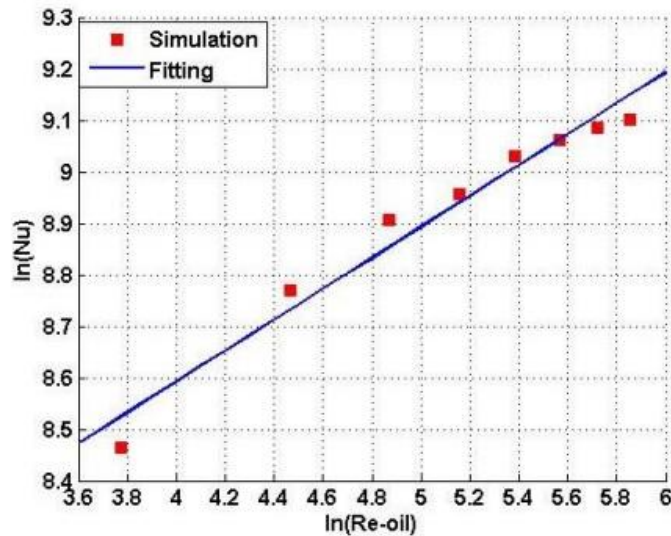


Figure 3.52. The wall Nusselt number as a function of the oil supply Reynolds number

According to the results [22] heat transfer between the oil film flow and the inner bearing chamber wall will increase with the rise of rotation speed. Along with the increase of rotation speed, the heat transfer in the two sides of position along the axial direction gradually increases. The nature logarithm of the average Nusselt number around the circumference of the bearing chamber wall is directly proportional to the 0.3 power of the nature logarithm of the oil supply Reynolds number. The nature logarithm of the average Nusselt number around the circumference of the bearing chamber wall is directly proportional to 0.345 power of the nature logarithm of the rotational Reynolds number of rotating shaft.

Using mathematical model [37] was obtained results of heat transfer in bearing chamber. The heat transfer coefficient calculated at the walls (of the bearing chamber) is shown for two different time steps in Fig. 3.53. The “left” and “right” views of the chamber are displayed on that figure. The heat transfer coefficient is higher toward the top region of the chamber which can be consistently attributed to the thinness of the wall film.

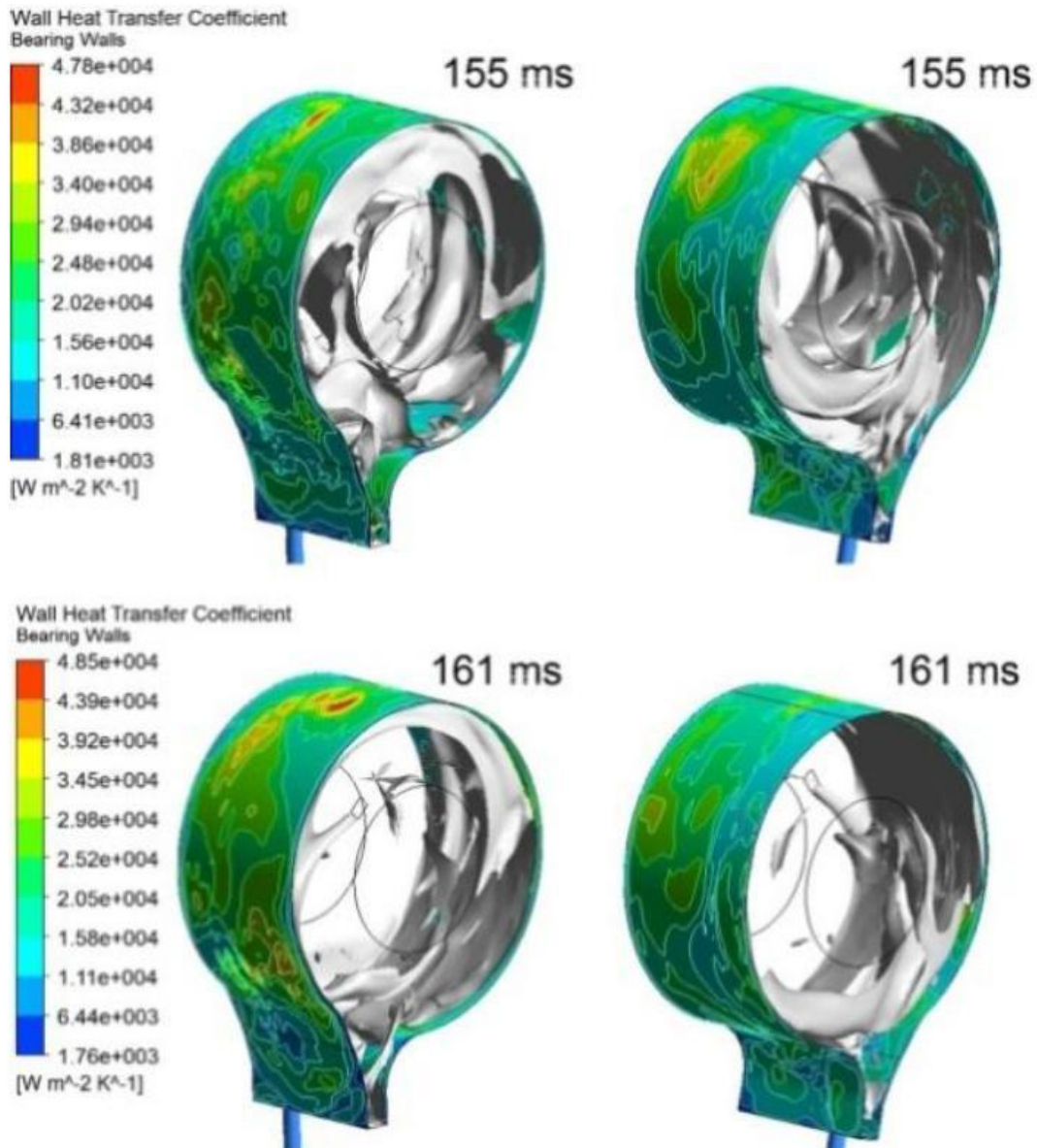


Figure 3.53. Heat transfer coefficient calculated on the bearing chamber walls

In paper [68] the study of numerical analysis of bearing lubrication flow field is presented. For high speed bearings, the numerical model is shown in Fig. 3.54.

Bearing internal flow field

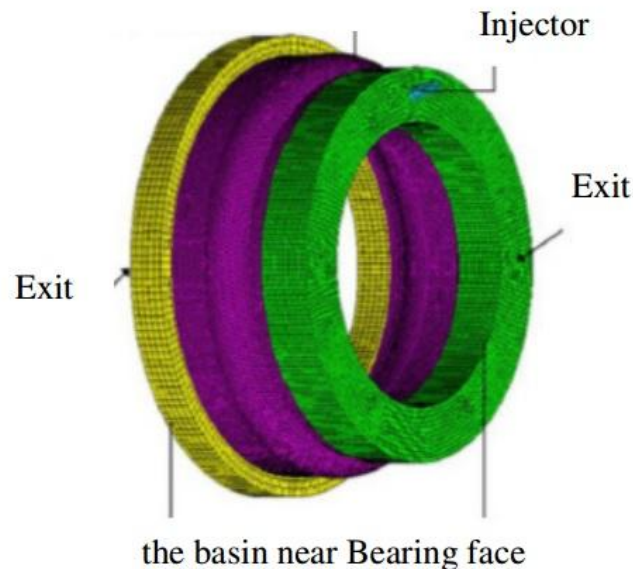


Figure 3.54. Finite element model of bearing lubrication

The bearing speed is 8000r/min, the DN value of the ball bearing work reaches 4×10^5 , and the lubrication flow rate is 3L/min. When the injection speed is 10m/s, the temperature distribution in the bearing cavity is shown in Fig. 3.55. As can be seen from the diagram, the temperature distribution is not uniform. Up near the nozzle and the rotation direction of the bearing to reduce, which also affected bearing internal flow temperature in the circumferential direction of the uneven distribution of bearing.

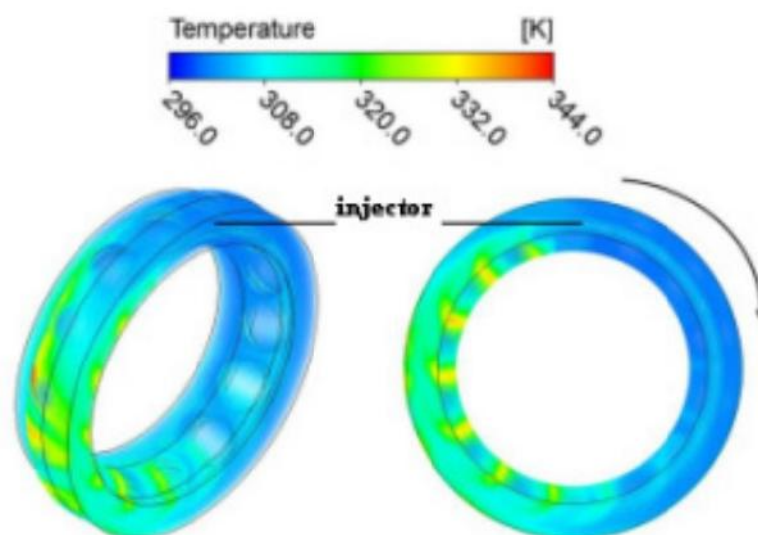


Figure 3.55. Temperature distribution of two phase flow field inside the bearing

When the lubricating oil enters the bearing, the interaction between the rolling element and the cage of the bearing will produce oil friction resistance, thus hindering the rolling of the rolling wheel. The more lubricating oil is, the greater the friction resistance is, and the more

oil loss is produced. Fig. 3.56 is the bearing internal rolling surface shear force distribution, bearing speed is 8000r/min, lubrication flow is 3L/min.

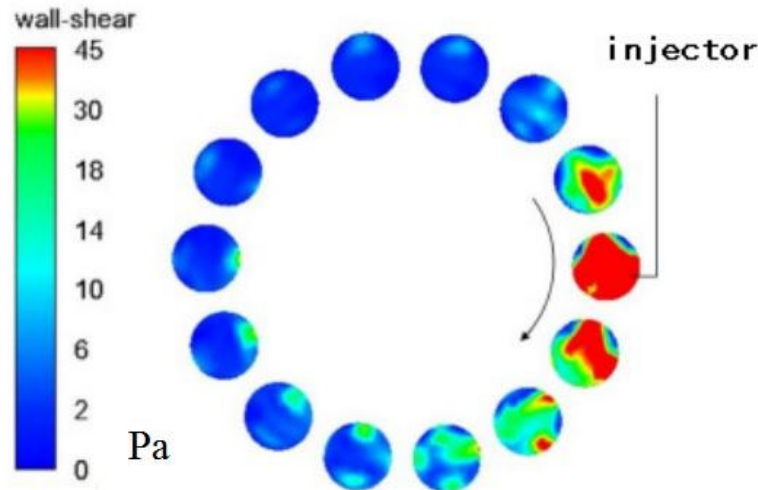


Figure 3.56. Surface shear stress distribution of rolling body

It can be seen from the figure, the rolling body surface shear stress is mainly composed of hindered lubricating oil caused by distribution and the distribution of the oil volume fraction of the shear force, the nozzle, gradually decreases along the direction of rotation bearing, oil volume fraction is where the friction resistance is greater, the greater the shear stress. [68]

In [69] presents thermal analyses of a bearing chamber located at the mid of the front frame structure where relatively lower wall temperatures encountered at engine operating conditions. Two Finite Element (FE) thermal modelling approaches were established to obtain temperature distribution over the bearing chamber inner wall by using FE thermal analysis software.

At the thermal model-1, heat capacity of oil flows into the cavity was used for the boundary condition at the bearing inner walls with the heat transfer coefficient derived empirically depending on rotational Reynolds number of shaft based on previous experiences. Thermal balance is reached in bearing chamber cavity providing equilibrium temperature with surrounding boundary conditions.

At the thermal model-2, temperature and mass flow of oil – air mixture were used in the cavity with the heat transfer coefficient based on oil related and sealing air related Reynolds number, mixture temperature and mixture mass flow, which is recommended in [20]. Mass flow and temperature in the cavity is defined by oil and sealing air flow which enter through both bearing elements.

Thermal model-2 considers a convective boundary condition which is provides equilibrium temperature with surroundings and fluid enthalpy is considered as lumped heat source. Thermal model-2 also considers convective boundary conditions for inner wall of the bearing chamber however this time heat exchange occurs between fluid and surfaces depending on the fluid flow direction. Considering the fluid flow directions, assumptions have been made depending on the seal air entrance and vent port location.

The results of modelling [69] are presented in Fig. 3.57.

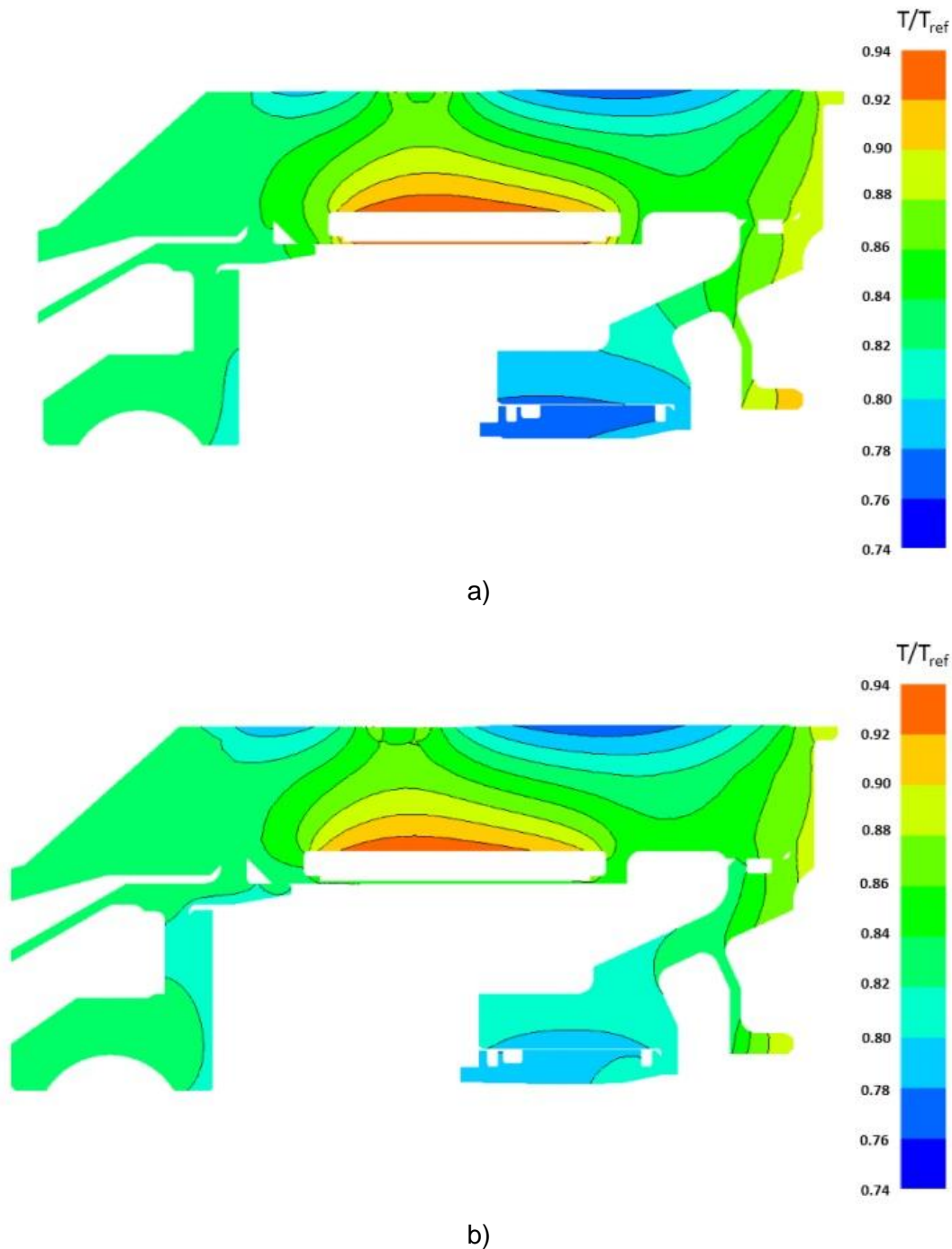


Figure 3.57. Result of the thermal model-1 (a) and model-2 (b)

According to Fig. 3.57 temperature values are higher on the inner manifold wall for the first modelling approach. Little differences were observed on temperature distribution at the front and rear support walls since fluid temperature change locally on the model-1. In general, model-2 predicts higher fluid temperature in bearing chamber and almost same with the model-1.

Summary

The works presented in the review clearly show that the problem of studying the processes occurring in the bearing chamber are relevant and are being studied by many researchers in various countries. Within the lubrication system, the design of a reliable, robust and efficient bearing chamber is considered to be the most challenging part, due to the complexity of the coincident two-phase flow phenomena, namely the wall films attached to the chamber walls, the droplet laden air flows, and the drop-film interactions. A special feature of these flow phenomena in bearing chambers is their strong dependence on the geometric configuration and engine operation cycle. The problem of heat exchange simulation is caused by the multiphase fluid in the bearing chamber. Heat transfer coefficients of multiphase fluid in bearing chamber depend on many factors, like flow structure, rotational speed of the shaft, amount of injected oil and airflow rate over the labyrinth seal, geometrical parameters of the cavity, etc.

Experimental investigations performed in the University of Karlsruhe provided a great contribution to understanding of bearing chamber flow distribution and heat transfer phenomena. Most of the reviewed experimental studies were carried out on the experimental setup created in the University of Karlsruhe and initially shown in [5]. Because the experimental data is usually limited to studies for simple geometrical forms of bearing chambers, as well as some simplifications related to limitations in the use of experimental methods, these studies can serve as a basis for validation of numerical modelling results only in the bearing chamber of simplified geometry.

The thermal and hydraulic processes in the bearing chamber belong to the processes that are very hard to be covered with the mathematical models. The behavior of the multiphase fluid (droplet-film-air) is influenced by oil and air flow rates, rotational speed, bearing chamber design and pressure in the bearing chamber, changes in the thermodynamic properties of phases due to heat transfer, roughness of the chamber walls and many other factors. The known numerical studies are often limited to the isothermal conditions of an air-oil flow.

There is no concrete model for calculation multiphase flows. Each problem should be using individual CFD-model. The growing potential of the multiphase CFD technique, together with increasing computational resources, tend to development of an integrated CFD multiphase modeling technique. Despite the significant progress in the modelling of the droplet and wall film dynamics in bearing chambers, there has still been a lack of a physical sub-model accounting for the description of the mass and momentum exchange between the impinging drops and the wall films. For this reason, a detailed understanding and modeling of the drop-to-film interaction is inevitable for the future simulation tools of oil system flow design. Therefore, in order to better understand the phenomena of heat transfer and flow distribution in the bearing chamber, the use of CFD simulation methods in combination with experimental data looks like a state of the art of the problem.

Although, the considered problem is very important for the gas turbine industry, this complex field has not yet been fully studied and is the subject of research within the framework of AMBEC project. The goal of AMBEC project is to achieve a complete understanding of the physical phenomena in the bearing chamber and create the methodology to calculate the heat transfer coefficient and the fluid flows (repartition) for different zones in the bearing chamber depending on the key parameters. To achieve this, the experimentals' methods, numerical methods and fundamental laws of the theory of heat transfer and fluid flow will be used.



AMBEC methodology will be based on combination of advanced CFD simulation of fluid flows and heat transfer with experimental data received by using experimental bearing chamber. Experimental data will be analyzed and compared to the prediction of CFD simulation. The differences will be analyzed and new methods set up in order to acquire a methodology able to predict the phenomena in a bearing chamber in hot and compact environment.

References

1. Inozemtsev, A. A., Nihamkin, M. A., Sandratskiy, V. L. (2008) Osnovyi konstruirovaniya aviatsionnyih dvigateley i energeticheskikh ustanovok. Vol. 1. Obschie svedeniya. Osnovnyie parametryi i trebovaniya. Konstruktivnyie i silovyye shemyi. [Aircraft engines and power plants designing basics. Vol. 1. General information. Basic parameters and requirements. Constructive and power circuits : textbook. for universities] Moscow: Mashinostroenie Publ., 2008. – 207 p.
2. Mykhailenko, ., Nemchenko, D., Douaissia Omar Hadj Aissa and Petukhov, I. (2017) Podhodyi k modelirovaniyu teplogidravlicheskih protsessov v elementah maslosistemyi GTD [Approaches to the Simulation of Thermal Hydraulic Processes in the Oil System Elements of Gas Turbine Engine], Bulletin of NTU "KhPI". Series: Power and heat engineering processes and equipment, no. 10 (1232), pp. 79-84
3. Isachenko, V. P., Osipova, V. A. and Sukomel, A. S. (1981), Teploperedacha. Uchebnik dlya vuzov [Heat transfer : textbook. for universities], Energiya, Moscow, Russia.
4. Wang, C, Morvan, H. P., Hibberd, S. and Cliffe, K. A. (2011), Thin Film Modelling For Aero-Engine Bearing Chambers, Vancouver, British Columbia, Canada, ASME 2011 Turbo Expo: Turbine Technical Conference and Exposition, Vol. 1, pp. 1–10, ISBN 978-0-7918-5461-7.
5. S. Wittig, A. Glahn, and J. Himmelsbach. Influence of high rotational speeds on heat transfer and oil film thickness in aero engine bearing chambers. – Lehrstuhl and Institut für Thermische Strömungsmaschinen, Universität Karlsruhe (T.H.), Karlsruhe, Germany, Journal of engineering for gas turbines and power, ASME, 1994, 93-GT-209, p. 395-401.
6. A. Glahn, S. Wittig, Two-Phase Air/Oil Flow in Aero-Engine Bearing Chambers Assessment of an Analytical Prediction Method of the Internal Wall Heat Transfer. – International Journal of Rotating Machinery 1999, Vol. 5, No. 3, pp. 155-165.
7. A. Glahn, S. Wittig Two-phase air/oil flow in aero engine bearing chambers – characterization of oil film flows. – Lehrstuhl und Institut für Thermische Strömungsmaschinen, Universität Karlsruhe, Germany, International Gas Turbine and Aeroengine Congress & Exposition, Houston, Texas, 1995, 95-GT-114.
8. P. Gorse, S. Busam, K. Dullenkopf. Influence of Operating Condition and Geometry on the Oil Film Thickness in Aeroengine Bearing Chambers. Journal of Engineering for Gas Turbines and Power, January, 2006, vol. 128, p. 103-110.
9. Wolfram Kurz, Klaus Dullenkopf, Hans-Jörg Bauer. Influences on the oil split between the oftakes of an aero-engine bearing chamber. – Proceedings of ASME Turbo Expo 2012, GT2012-69412, June 11-15, 2012, Copenhagen, Denmark.
10. Wolfram Kurz, Klaus Dullenkopf, Hans-Jörg Bauer. Capacitive film thickness measurements in a ventless aero-engine bearing chamber – influence of operating. – Proceedings of ASME Turbo Expo 2013: Turbine Technical Conference and Exposition, GT2013-94973, June 3-7, 2013, San Antonio, Texas, USA.
11. Wolfram Kurz and Hans-Jörg Bauer. An Approach for Predicting the Flow Regime in an Aero Engine Bearing Chamber. ASME Turbo Expo 2014: Turbine Technical Conference and Exposition Volume 5C: Heat Transfer, Düsseldorf, Germany, June 16–20, 2014
12. Amir A. Hashmi, Klaus Dullenkopf, Hans-Jörg Bauer, Michael Klingsporn. Experimental

investigation of lubrication oil film dynamics in a typical aero-engine bearing chamber environment. – Proceedings of ASME Turbo Expo 2011, GT2011-45545, June 6-10, 2011, Vancouver, British Columbia, Canada.

13. Chandra, B., Simmons, K., Pickering, S., Collicott, S. H., Wiedemann, N. Study of Gas/Liquid Behavior Within an Aeroengine Bearing Chamber. – Journal of Engineering for Gas Turbines and Power, May 2013, Vol. 135 / 051201-1.

14. Jee Loong Hee, R. Santhosh, Kathy Simmons, Graham Johnson, David Hann, Michael Walsh. Oil film thickness measurements on surfaces close to an aeroengine ball bearing using optical techniques. – Proceedings of ASME Turbo Expo 2017: Turbomachinery Technical Conference and Exposition, GT2017-63813, June 26-30, 2017, Charlotte, NC, USA.

15. . Chr. Mundo, M. Sommerfeld and C. Tropea Droplet-wall collisions: experimental studies of the deformation and breakup process. – Lehrstuhl für Strömungsmechanik, Universität Erlangen-Nürnberg, Cauerstr. 4, 91058 Erlangen, Germany, Int. J. Multiphase Flow Vol. 21, No. 2, pp. 151-173, 1995.

16. A. Glahn, M. Kurreck, M. Willmann and S. Wittig. Feasibility Study on Oil Droplet Flow Investigations Inside Aero Engine Bearing Chambers – PDPA Techniques in Combination With Numerical Approaches. J. Eng. Gas Turbines Power 118(4), 1996, pp. 749-755

17. P. Gorse¹, K. Dullenkopf, H.-J. Bauer and S. Wittig. An experimental study on droplet generation in bearing chambers caused by roller bearings. – Proceedings of ASME Turbo Expo 2008: Power for Land, Sea and Air, GT2008, June 9-13, 2008, Berlin, Germany.

18. Ph. Gorse, K. Willenborg, S. Busam, J. Ebner, K. Dullenkopf and S. Wittig, 3d-LDA Measurements in an Aero-Engine Bearing Chamber, Proceedings of ASME Turbo Expo 2003, Power for Land, Sea, and Air, June 16–19, 2003, Atlanta, Georgia, USA.

19. A. Glahn, S. Busam and S. Wittig. Local and mean heat transfer coefficients along the internal housing walls of aero engine bearing chambers. – Lehrstuhl und Institut für Thermische Strömungsmaschinen, Universität Karlsruhe (T.H.), 76128 Karlsruhe, Germany, International Gas Turbine & Aeroengine Congress & Exhibition, Orlando, Florida — June 2-June 5, 1997.

20. S. Busam, A. Glahn, S. Wittig Internal Bearing Chamber Wall Heat Transfer as a Function of Operating Conditions and Chamber Geometry, J. Eng. Gas Turbines Power Vol. 122, ASME, 2000, p.314-320.

21. Yuan Xichuan^{1,a}, Guo Hui^{1,b} and Wang Liangyun. Experiment Study of Heat Transfer in Aeroengine Bearing Chambers, Applied Mechanics and Materials, Trans Tech Publications, Switzerland, Vol 86 (2011), pp. 448-453, 2011.

22. Zhenxia Liu, Fei Zhang. The numerical simulation and experimental study on aero-engine bearing cavity wall heat transfer. – ISABE-2017-21379, 2017.

23. Budi W. Chandra, Steven H. Collicott, John H. Munson. Experimental optimization of Rolls-Royce AE3007 sump design, Proceedings of ASME Turbo Expo 2017: Turbomachinery Technical Conference and Exposition, GT2017-64030, June 26-30, 2017, Charlotte, NC, USA.

24. Felix C. von Plehwe, Benedikt Brox, Corina Schwitzke, Hans-Jörg Bauer. Experimental investigation of the influence of chamber geometry on bearing chamber oil leakage. – Proceedings of ASME Turbo Expo 2017: Turbomachinery Technical Conference and

Exposition, GT2017-63561, June 26-30, 2017, Charlotte, NC, USA.

25. Enrico Munari, Michele Pinelli. A review of wet gas flow rate measurements by means of singlephase meters, Proceedings of ASME Turbo Expo 2018, Turbomachinery Technical Conference and Exposition, GT2018-76190, June 11-15, 2018, Oslo, Norway.
26. Zimmermann, H, Kammerer, K, Fischer, R and Rebhahn, D., 1991. Two-phase flow correlations in air/oil systems of aero engines. ASME paper 91-GT-54.
27. Chew, J. W. Analysis of the oil film on the inside surface of an aero engine bearing chamber housing. International Gas Turbine and Aeroengine Congress and Exhibition, Birmingham, UK, 10–13 June 1996, ASME 96-GT-300.
28. Deissler, R., 1954, Heat transfer and fluid friction for fully developed turbulent flow of air and supercritical water with variable fluid properties, Transactions of the ASME, 76, 73-85.
29. C. Wang, H. P. Morvan, S. Hibberd, K. A. Cliff, A. Anderson, A. Jacobs, Specifying and benchmarking a thin film model for oil systems applications in ANSYS fluent. ASME Turbo Expo 2012: Turbine Technical Conference and Exposition, pp. 229-234. American Society of Mechanical Engineers, 2012.
30. Chen, GD, Sun, HC, Wang, J. Research into configuration and flow of wall oil film in bearing chamber based on droplet size distribution. Chin J Aeronaut 2011; 24: 355–362.
31. Farrall, M., Simmons, K., Hibberd, S., and Gorse, P. A numerical model for oil film flow in an aero-engine bearing chamber and comparison with experimental data. ASME Turbo Expo 2004, Power for Land, Sea and Air, Vienna, Austria, 14–17 June 2004, GT 2004-53698.
32. B. Kakimpa, H. P. Morvan and S. Hibberd, A Coupled 1D Film Hydrodynamics and Core Gas Flow Model for Air-Oil Flows in Aero-Engine Bearing Chambers. ASME Turbo Expo 2017: Turbomachinery Technical Conference and Exposition, Vol. 2B: Turbomachinery, Charlotte, North Carolina, USA, 26–30 June 2017, ASME GT2017-64693
33. Kakimpa B., Morvan H. P. and Hibberd S., 2016, “The Depth-Averaged Numerical Simulation of Laminar Thin-ilm Flows With Capillary Waves,” J. Eng. Gas Turbines Power, vol. 138, no. 11, pp. Paper No: GTP-16-1105
34. B. Kakimpa, H. P. Morvan and S. Hibberd, “Solution strategies for thin film rimming flow modelling,” ASME Turbo Expo 2015: Turbine Technical Conference and Exposition, GT2015-43503. American Society of Mechanical Engineers, 2015.
35. Kay E. D., Hibberd S. and Power H., 2014, “A depth averaged model for non-isothermal thin-film rimming flow,” Int. J. Heat Mass Tran., vol. 70, p. 1003–1015
36. Kay E. D., Hibberd S. and Power H. “Non-isothermal rimming flow with the effects of surface shear and droplet impact,” Physics of Fluids; 2015, Vol. 27 Issue 12, p122105-1
37. Akinola A. Adeniyi, Hervé P. Morvan and Kathy A. Simmons. A Transient CFD Simulation of the Flow in a Test Rig of an Aeroengine Bearing Chamber. ASME Turbo Expo 2014: Turbine Technical Conference and Exposition Volume 5C: Heat Transfer, Düsseldorf, Ger-many, June 16–20, 2014
38. Alexandre Crouchez-Pillot and Hervé P. Morvan. CFD Simulation of an Aeroengine Bearing Chamber Using an Enhanced Volume of Fluid (VOF) Method: An Evaluation Using Adaptive Meshing. ASME Turbo Expo 2014: Turbine Technical Conference and Exposition Vol-ume 5C: Heat Transfer, Düsseldorf, Germany, June 16–20, 2014.
39. Andrea Bristot, Hervé P. Morvan and Kathy A. Simmons. Evaluation of a Volume of Fluid

CFD Methodology for the Oil Film Thickness Estimation in an Aero-Engine Bearing Chamber. ASME Turbo Expo 2016: Turbomachinery Technical Conference and Exposition Volume 2C: Turbomachinery, Seoul, South Korea, June 13–17, 2016.

40. Review of fluid flow and convective heat transfer within rotating disk cavities with impinging jet S. Harmand, J. Pellé, S. Poncet, I.V. Shevchuk

41. Journal of computational physics 39, 201-225 (1981) Volume of Fluid (VOF) Method for the Dynamics of Free Boundaries* C. W. Hirt and B. D. Nichols Los Alamos Scientific Laboratory, Los Alamos, New Mexico 87545 Received November 1, 1979

42. D. Peduto, R. Koch, H. Morvan, K. Dullenkopf, and H.-J. Bauer, "Numerical studies of Single Drop impact on to a plane Shallow and Deep Liquid Pool," presented at the ILASS – Europe 2011, 24th Ann. Conf. on Liq. Atom. and Spray Systems, Estoril, Portugal, 2011.

43. Davide Peduto, Amir A. Hashmi, Klaus Dullenkopf, Hans-J, Herve Morvan. Modelling of an aero engine bearing chamber using enhanced cfd technique Proceedings of ASME Turbo Expo 2011 GT2011 June 6-10, 2011, Vancouver, British Columbia, Canada

44. Hashmi, A., Dullenkopf, K., Koch, R., and Bauer, H.-J., 2010. "CFD methods for shear driven liquid wall films". ASME-Paper: GT2010-23532.

45. Warren, G. P., Anderson, W. K., Thomas, J. L., & Krist, S. Grid Convergence for Adaptive Methods. AIAA Computational Fluid Dynamics Conference, 1991.

46. Jibin Hu, Wei Wu, Mingxing Wu, Shihua Yuan. Numerical investigation of the air–oil two-phase flow inside an oil-jet lubricated ball bearing. Jibin International Journal of Heat and Mass Transfer 68 (2014) 85–93.

47. M. Ramdin, R. Henkes, Computational fluid dynamics modeling of Benjamin and Taylor bubbles in two-phase flow in pipes, J. Fluids Eng. Trans. ASME 134 (4) (2012) 1–8.

48. E. Da Riva, D. Del Col, Numerical simulation of laminar liquid film condensation in a horizontal circular minichannel, J. Heat Transfer-Trans. ASME 134 (5) (2012) 1–8.

49. L Yu Yaguo, Jiang Le, LIU Zhenxia, Hu Jianping. Simulation and analysis of oil scoop capture efficiency. Proceedings of ASME Turbo Expo 2018. Turbomachinery Technical Conference and Exposition GT2018. June 11-15, 2018, Oslo, Norway. GT2018-75989

50. M Berthold, H. Morvan, R. Jefferson-Loveday, B. C. Rothwell, C. Young. Multiphase CFD modeling of external oil flow from a journal bearing. Proceedings of ASME Turbo Expo 2018 Turbomachinery Technical Conference and Exposition GT2018. June 11-15, 2018, Oslo, Norway. GT2018-77130

51. Peduto, D. (2015) Oil droplet impact dynamics in aeroengine bearing chambers: correlations derived from direct numerical simulations. PhD thesis, Karlsruhe Institute of Technology and University of Nottingham. Access from the University of Nottingham repository: http://eprints.nottingham.ac.uk/28997/1/Peduto_Davide_300dpi.pdf

52. J. Zhao, Z. Liu, Y. Lyu, P. Zhu, 2016 Analysis of Oil - Gas Interaction in the Aero-Engine Bearing Chamber., 2016 STLE Annual Meeting & Exhibition, 15-19 May 2016, Las Vegas, Nevada, USA

53. Lyu Yaguo, Zhao Jingyu, Liu Zhenxia, Ren Guozhe. 2016. Numerical study on the effect of oil removal from aero-engine bearing chamber and improvement, 2016 STLE Annual Meeting & Exhibition, 15-19 May 2016, Las Vegas, Nevada, USA

54. Denner, F., and van Wachem, B. G., 2015, "Numerical Time-Step Restrictions as a

Result of Capillary Waves," *J. Comput. Phys.*, 285(1), pp. 24–40.

55. Jingyu Zhao*, Zhenxia Liu, Yaguo Lu and Jianping Hu. Numerical Modeling of Unsteady Oil Film Motion Characteristics in Bearing Chambers. *Int J Turbo Jet Eng* 2015; 32(3): 233–245
56. O'Rourke, P. J., and Amsden, A. A., 1996, "A Particle Numerical Model for Wall Film Dynamics in Port- Injected Engines," SAE Paper 961961.
57. O'Rourke, P. J., and Amsden, A. A., 2000, "A Spray/wall Interaction Sub model for the KIVA-3 Wall Film Model," SAE Paper 2000-01-0271
58. Williams, J., 2007, "The Effect of Droplet Impact on Thin Film Rimming Flow," PhD Report, University of Nottingham.
59. B. Kakimpa, H.P. Morvan and S. Hibberd Thin-film flow over a rotating plate: an assessment of the suitability of VOF and Eulerian Thin-Film Methods for the numerical simulation of isothermal thin-film flows, Proceedings of ASME Turbo Expo 2015: Turbine Technical Conference and Exposition GT2015 June 15 – 19, 2015, Montréal, Canada.
60. B. Kakimpa, H.P. Morvan and S. Hibberd. The numerical simulation of multi-scale oil films using coupled VOF and Eulerian thin-film models. Proceedings of ASME Turbo Expo 2016: Turbomachinery Technical Conference and Exposition GT2016 June 13 – 17, 2016, Seoul, South Korea
61. Akinola A. Adeniyi, Budi Chandra, Kathy Simmons. Computational study of a customised shallow-sump aero-engine bearing chamber with inserts to improve oil residence volume. Proceedings of ASME Turbo Expo 2017: Turbomachinery Technical Conference and Exposition GT2017 June 26-30, 2017, Charlotte, NC, USA
62. Andrea Bristot, Herve P. Morvan, Kathy Simmons, Michael Klingsporn. Effect of turbulence damping in VOF simulation of an aero-engine bearing chamber Proceedings of ASME Turbo Expo 2017: Turbomachinery Technical Conference and Exposition GT2017 June 26-30, 2017, Charlotte, NC, USA
63. Egorov, Y., Boucker, M., Martin, A., Pigny, S., Scheuerer, M., and Willemsen, S., 2004. Validation of CFD codes with PTS-relevant test cases. Report, 5th Euratom Framework Programme ECORA project, September. See also URL [https://domino.grs.de/ecora/ecora.nsf/16edc336e8a342f580256502004d0e8b/684c0ed5f389add8c1256fcd002e7cb8/\\$FILE/D07_WP4.pdf](https://domino.grs.de/ecora/ecora.nsf/16edc336e8a342f580256502004d0e8b/684c0ed5f389add8c1256fcd002e7cb8/$FILE/D07_WP4.pdf)
64. Tkaczyk, P., 2011. "CFD simulation of annular flows through bends". PhD Thesis, The University of Nottingham, Nottingham, UK.
65. Krug, Matthias B.; Kurz, Wolfram; Höfler, Corina; Bauer, Hans-Jörg. Evaluation of the Volume-of-Fluid Method for the Numerical Modelling of an Aero Engine Bearing Chamber. The 22nd International Symposium on Air Breathing Engines. ISABE Conference 2015, Phoenix, AZ, USA, October 25-30, 2015. Paper No: ISABE-2015-21284.
66. Akinola A. Adeniyi, Hervé P. Morvan, Kathy A. Simmons. A multiphase computational study of oil-air flow within the bearing sector of aeroengines. Proceedings of ASME Turbo Expo 2015: Turbine Technical Conference and Exposition GT2015 June 15 – 19, 2015, Montréal, Canada
67. Adeniyi, A. A., 2014. "A Coupled Eulerian-Lagrangian Framework to model droplet to film interaction with Heat Transfer". PhD thesis, University of Nottingham.

68. Bing LI, Liang-hua ZENG, Bao-shan HUANG. Study on Two Phase Flow Heat Transfer of High Speed Bearings by Injection Lubrication. 2017 2nd International Conference on Mechatronics, Control and Automation Engineering (MCAE 2017)
69. Volkan Tatar, Altug Piskin. Numerical investigation on bearing chamber wall heat transfer. Proceedings of ASME Turbo Expo 2018. Turbomachinery Technical Conference and Exposition GT2018. June 11-15, 2018, Oslo, Norway. GT2018-75721

This publication reflects only the authors view and the Clean Sky 2 JU is not responsible for any use that may be made of the information it contains.